The Dissertation Committee for Yang Zhao certifies that this is the approved version of the following Dissertation:

Bio-Inspired Nanophotonics: Manipulating Light at the Nanoscale with Plasmonic Metamaterials

Committee:

Andrea Alù, Supervisor

Mikhail Belkin

Hao Ling

Gennady Shvets

Edward Yu

Bio-Inspired Nanophotonics: Manipulating Light at the Nanoscale with Plasmonic Metamaterials

by

Yang Zhao, B.E.; M.Phil.; M.S.

Dissertation

Presented to the Faculty of the Graduate School of

The University of Texas at Austin

in Partial Fulfillment

of the Requirements

for the Degree of

DOCTOR OF PHILOSOPHY

The University of Texas at Austin

May 2013

Dedication

To my family.

Acknowledgements

As the conclusion of my Ph.D. study, I want to take this chance to sincerely thank many people for their endless support. I'm very grateful to my Ph.D. advisor, Prof. Andrea Alù, for his generous acceptance of me becoming one of the first three members of his lab, and I want to thank him for his wholehearted guidance and strongest support during my study. I would also like to thank all my committee members: Prof. Mikhail Belkin, Prof. Hao Ling, Prof. Gennady Shvets, and Prof. Edward Yu for their attendance to my proposal and dissertation defense, and their support and guidance during my study. I want to thank Prof. Engheta, Prof. Halas, Prof. Nordlander, Prof. Laura Liu, Prof. Elaine Li, Prof. Boltasseva, Prof. Shih, and Prof. Shi for their collaborations during my Ph.D. I want to thank Prof. Downer, Prof. Chen, Prof. Deppe, Prof. Wu, Prof. Ronald Chung, and Prof. Xu for their support and encouragement. I also want to thank the professors in CREOL: Prof. Stegeman, Prof. Boreman, Prof. Hagan, Prof. Moharam, Prof. Kik, Prof. Zeldovich, Prof. Wu, Prof. Deppe, Prof. Li, Prof. Schoenfeld, Prof. Christodoulides, Prof. Dogariu, Prof. Delfyett, Prof. LiKamWa, Prof. Richardson, and Prof. Saleh, who have educated me and brought me to the fabulous world of optics and photonics.

I want to thank all my friends: Aiting Jiang, Xing-Xiang Liu, Nasim Estakhri, Christos Argyropoulos, Amir Askarpoor, Ian Williamson, Nicholas Estep, Jason Soric, Khai Le, Romain Fleury, Mina Hanna, Andre Esteva, Caleb Sieck, Mohamed Farhat, Pai-Yen Chen, Francesco Monticone, Matt Guild, Tengxiang Zhang, Li Tao, Feng Lu, Shannon Miller, Steve Reed, Waston Henderson, Zhengyan Li, Rafal Zgadzaj, Xiaohui Gao, Xiaoming Wang, Lucas Loumakos, JC Sanders, Robert Ehlert, Junwei Wei, Ming Lei, Peng Dong, Hao Chen, K Shavitranuruk, Guowei Zhao, Sabine Freisem, Abdullah

Demir. Thank you for being my friends, I have remembered and I appreciate every single favor that I have received from any of you during this path. I also want to take this chance to thank Jack Clifford, who taught me how to do machining, and Gary Thomas, Robert Hasdorff, who has helped me in building electronics, which helped me greatly in my experiments. I want to thank the wonderful staff in ECE department, Melanie Gulick, Melody Singleton, Barry Levitch, and Jean Toll.

At last, I want to thank my family for their never ending love.

Bio-Inspired Nanophotonics: Manipulating Light at the Nanoscale with Plasmonic Metamaterials

Yang Zhao, Ph.D.

The University of Texas at Austin, 2013

Supervisor: Andrea Alù

Metals interact very differently with light than with radio waves and finite conductivities and losses often limit the way that RF concepts can be directly transferred to higher frequencies. Plasmonic materials are investigated here for various optical applications, since they can interact, confine and focus light at the nanoscale; however, regular plasmonic devices are severely limited by frequency dispersion and absorption, and confined signals cannot travel along plasmonic lines over few wavelengths. For these reasons, novel concepts and materials should be introduced to successfully manipulate and radiate light in the same flexible way we operate at lower frequencies. In line with these efforts, optical metamaterials exploit the resonant wave interaction of collections of plasmonic nanoparticles to produce anomalous light effects, beyond what naturally available in optical materials and in their basic constituents. Still, these concepts are currently limited by a variety of factors, such as: (a) technological challenges in realizing 3-D bulk composites with specific nano-structured patterns; (b) inherent sensitivity to disorder and losses in their realization; (c) not straightforward modeling of their interaction with nearby optical sources.

In this study, we develop a novel paradigm to use single-element nanoantennas, and composite nanoantenna arrays forming two-dimensional metasurfaces and three-dimensional metamaterials, to control and manipulate light and its polarization at the nanoscale, which can possibly bypass the abovementioned limitations in terms of design procedure and experimental realization. The final design of some of the metamaterial concepts proposed in this work was inspired by biological species, whose complex structure can exhibit superior functionalities to detect, control and manipulate the polarization state of light for their orientation, signaling and defense. Inspired by these concepts, we theoretically investigate and design metasurfaces and metamaterial models with the help of fully vectorial numerical simulation tools, and we are able to outline the limitations and ultimate conditions under which the average optical surface impedance concept may accurately describe the complex wave interaction with planar plasmonic metasurfaces. We also experimentally explore various technological approaches compatible with these goals, such as the realization of lithographic single element nanoantenna with complex circuit loads, periodic arrays of plasmonic nanoparticles or nanoapertures, and stacks of rotated plasmonic metasurfaces. At the conclusion of this effort, we have been able to theoretically analyze, design and experimentally realize and characterize the feasibility of using discrete metasurfaces to realize phenomena and performance that are not available in natural materials, oftentimes inspired by the biological world.

Table of Contents

List of Tables

List of Figures

Chapter 1: Introduction

1.1 POLARIZED VISION IN BIOLOGICAL SPECIES

Humans are considered the most advanced species on earth in terms of language, logical reasoning, problem solving, etc., however, many other biological species have superior functions that humans don't possess, one of which is polarized vision. Human eyes can distinguish 10 million colors and intensities at logarithmic scale, but have very weak abilities to distinguish polarization states of light. Many sea creatures, birds, and insects, however, have the capabilities to sense different polarizations. As one of the earliest studies in biological science, bees were shown to use the polarization information to conduct a "waggle waggle dance" to inform their peers of the location of food sources, which may be more than 100 meters away. This was first decoded by Karl von Frisch, an Austrian ethologist, who received Nobel Prize in Physiology or Medicine in 1973 for his investigation on sensory perceptions of bees. In his Nobel lecture, he explained "the direction of vibration of polarized blue light, differs in relation to the sun's position across the entire vault of the sky, thus, to one that is able to perceive the direction of vibration, even a spot of blue sky can disclose the sun's position by its polarization patterns" [1],[2]. His following experiments revealed bees' capabilities of sensing the polarizations of light: "The observation hive was set horizontally in a dark tent from which the dancers had a lateral view of a small area of blue sky. They danced correctly toward the west where their feeding place was located 200 m away. When a round, rotatable polarizing foil was placed over the comb in a way as not to change the direction of the vibration of the polarized light from that part of the sky, they continued to dance correctly. If, however, I turned the foil right or left, the direction of the bees' dance changed to the right or the left by corresponding angle values." [1]

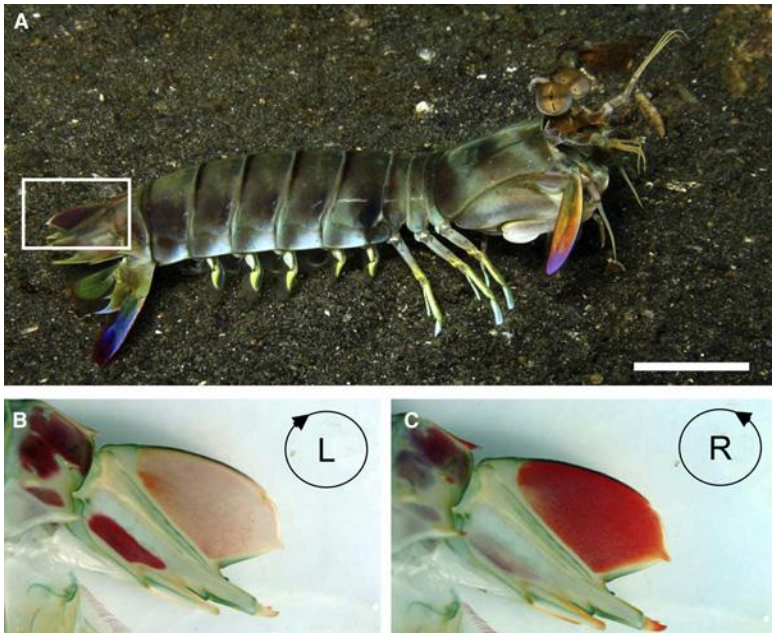

Figure 1.1: Circularly polarized signals of the mantis shrimp. (a) The stomatopod crustacean Odontodactylus cultrifer (male).The scale bar represents 1 cm. (b) Detail of telson keel (inset in (a)) photographed through a left-handed circular polarizing filter. (c) as (b) except photographed through a right-handed circular polarizing filter. Note the striking contrast difference compared to (b). (Image and caption adapted from Ref. [3])

In fact, not only bees, but many sea creatures possess polarized vision. Another well studied example is the mantis shrimp, whose vision system is considered as one of the most supreme kinds among all the studied sea creatures. Its spectrum covers from UV all the way to the near infra-red (NIR), and it could distinguish both linearly and circularly polarized light [2]. The skin of the mantis shrimp acts as a circular polarizer, polarizing sun light into left- or right-handed circularly polarized light. When examined under a circularly polarized light source, these skins could exhibit different colors (Figure 1.1). On the other hand, their eyes also function as a circularly polarization filter, and selectively filter the information reflected from the skin. The circularly polarized vision in mantis shrimp is believed to be closely related to the anatomical structure, which arises from the quarter-wave retardation effect from the overlying four-lobed R-8 cell [4].

In nature, these biological species use this superior polarized vision as part of the means to convey information to their peers, to navigate with minimum amount of light and to defend themselves against their enemies. Inspired by these amazing functions, we seek to create the same ability to humans in this research. Circularly polarized vision is not merely considered for navigational purposes, but could also bring many more intriguing applications to the modern mankind: for example, it could "enhance" our vision especially in turbid medium, such as in fogs or clouds; the same concept is also extended into circular polarized imaging systems in biomedical field, which has been recently studied for detecting tumors at early stages [5]. In addition, the possibility of creating and detecting circular polarization may be of interest for advanced optical signaling and sensors, due to its inherent robustness to scattering and diffraction.

Although polarization control and creation can be readily achieved through crystals such as quartz, tourmaline, or cordierite, the aforementioned applications ultimately require the generation of controllable polarized light, and highly compact and flexible designs to be able to integrate into existing imaging, microfluidic, or nanophotonic systems. The rigidity and bulkiness of natural polarizing crystals hinder the further advancement of these technologies.

In this study, we circumvented the limitations of natural materials by employing newly emerged artificial materials, metamaterials, and realized a prototype of the first broadband nanometer-thick optical polarizing device that bypassed the narrowband challenges inherent in existing metamaterials, transferred the three-dimensional concept to two-dimensional, which released both technological challenges in fabrication and in modeling.

1.2 INTRODUCTION TO METAMATERIALS

Metamaterials are artificial materials composed of sub-wavelength engineered inclusions, designed to collectively achieve exotic electromagnetic properties at the frequency of interest, beyond those available in nature or in any of their constituents. Although technology and nanofabrication have evolved at a fast pace and reached levels of flexibility that were unimaginable even a few years ago, specific physical and engineering challenges associated with design and realization of optical metamaterials still remain unresolved. In particular, technological challenges limit the realization of fully three-dimensional nanoscale metamaterials, especially in the optical regime [6]-[12]; in addition, the complex wave matter interaction in large arrays of resonant nanostructures, often with exotic plasmonic properties [13]-[15], requires parallel advances in the theoretical understanding and modeling of these effects.

Different from metamaterials, metasurfaces or metafilms are effectively the two-dimensional equivalent of metamaterials [16]-[18]. The interest in their design, realization and characterization has grown in parallel with the interest in metamaterials, as it was shown that, by tailoring their resonant constituent sub-wavelength inclusions, they may provide analogous exotic electromagnetic phenomena, such as negative index of refraction [19], sub-diffraction imaging [20], nanocircuitry [21]-[23] and cloaking [24],[25]. Their reduced profile makes them appealing and of easier realization from a practical and technological point of view.

By using these artificial materials and designing their nano-constituents and arrangements, we could control the current circulation at the surface, and further manipulate the phases and amplitudes of electromagnetic waves radiated to the far field, mimicking the polarized vision functions in biological species. At the optical frequencies, dielectric metamaterials still exhibit specific thickness limitations. In this regard,

employing plasmonic materials for the constituents of the optical metamaterials can provide unprecedented opportunities to manipulate light polarization at the nanoscale by exploiting the strong field localization and enhancement due to the localized light interaction with surface plasmons.

1.3 INTRODUCTION TO PLASMONICS

At microwave frequencies, metals are usually modeled as perfect electric conductors, since their small Ohmic losses are often negligible. At these frequencies and below, metals are used as reflectors (mirrors) and conducting electrodes for devices. At higher frequencies, up to the near infrared (NIR) and visible frequencies region, electromagnetic waves penetrate more into the metals, and the strong dispersion of metals opens interesting possibilities, currently described in the general field of plasmonics. In contrast to volume plasmons that can be excited in bulk metals, in this dissertation we focus on surface plasmons that exist in deeply sub-wavelength metal nanoparticles and densely packed arrays of nanoparticles. In particular, we focus on localized surface plasmons, which do not require phase-matching of the wave vectors to be excited, and arise mainly based on scattering phenomena. The scattering theory of single particles has been nicely carried out in chapter 4 and chapter 12 of [26], and the physics of localized surface plasmon is discussed in great details in chapter 5 of [27] and chapter 9 of [28]. Here we only summarize a few key points of these fundamental theories.

The seminal Mie theory of scattering was developed to understand the various colors from colloidal spherical particles. It solves for the scattered field by expanding the excitation plane wave in vector spherical harmonics and imposing the boundary conditions at the surface of the sphere being excited. Thus, the scattering coefficients are [1]:

$$a_n = \frac{\mu m^2 j_n(mx)\left[xj_n(x)\right]' - \mu_1 j_n(x)\left[mxj_n(mx)\right]'}{\mu m^2 j_n(mx)\left[xh_n^{(1)}(x)\right]' - \mu_1 h_n^{(1)}(x)\left[mxj_n(mx)\right]'}, \tag{1.1}$$

and

$$b_n = \frac{\mu_1 j_n(mx)\left[xj_n(x)\right]' - \mu j_n(x)\left[mxj_n(mx)\right]'}{\mu_1 j_n(mx)\left[xh_n^{(1)}(x)\right]' - \mu h_n^{(1)}(x)\left[mxj_n(mx)\right]'}, \tag{1.2}$$

where $x = 2\pi Na/\lambda$, $m = N_1/N$, and N_1, N are refractive indices of the particle and the medium, μ_1 and μ are the permeability of the particle and the medium, and a is the radius of the particle, j_n is the spherical Bessel function. The scattered wave is related to these scattering coefficients and the vector spherical harmonics $\mathbf{M}$ and $\mathbf{N}$ as:

$$\mathbf{E}_s = \sum_{n=1}^{\infty} i^n E_0 (2n+1)/n(n+1)\left(ia_n\mathbf{N} - b_n\mathbf{M}\right), \tag{1.3}$$

Therefore, the scattered field is the largest when the denominators in (1.1) and (1.2) go to zero, which is satisfied when the frequencies of the sphere are complex [26]. These frequencies are the resonances of the spherical particle, which are dependent upon the size of the sphere.

The above equation can be dramatically simplified when the spherical particle dimension is much smaller than the wavelength of excitation ($a \ll \lambda$), we are dealing with problems in the quasi-static limit, which means only the time variation of field is kept, while no spatial retardation effect needs to be considered over the sphere volume. Under this circumstance, only the electric dipole term is dominant in the scattering terms, and the scattering cross section can be simplified as:

$$C_{sca} = \frac{8\pi}{3} k^4 a^6 \left| \frac{\varepsilon_1 - \varepsilon}{\varepsilon_1 + 2\varepsilon} \right|^2, \tag{1.4}$$

where ε_1 and ε are permittivity of the particle and the medium [27]. To maximize the scattering cross section, the condition deduced from (1.4) is $\varepsilon_1 = -2\varepsilon$, which requires the two permittivity values to exhibit the opposite sign at the same frequency. This condition can be met, at least for the real parts of the permittivities, when one of these materials is metal operated below plasma frequency, and the other one is dielectrics. The condition is the "resonant" condition, where electrons in the solid will exhibit collective and coherent oscillations triggered by photons. The plasma frequencies of noble metals are often close to the optical frequencies, which is the reason that plasmonic material is one of the best candidates to realize optical metamaterials with aforementioned functions.

1.4 ORGANIZATION OF THE DISSERTATION

The brief introduction to plasmonics presented in the previous section along with the functionalities inspired by biological species will guide our designs of optical metamaterials [29]. In this dissertation, we apply noble metals, such as silver and gold, and take the advantages of their strong dispersive nature near the optical and near-infrared frequencies to design resonant single nanoparticle or nanoparticle arrays with exotic properties and deeply sub-wavelength dimensions. The quasi-static limit introduced earlier applies to all the designs in this dissertation. The resonance of a single nanoparticle can be determined by vanishing the denominator of (1.4). In the visible to near-infrared frequencies gold and silver are good candidate materials when the nanoparticles are embedded in dielectrics such as air or silica. In most of our designs, the nanoparticles are not necessarily spherical, however, the resonance condition estimated in (1.4) can be tuned to different shape factors, as long as the size limitation is satisfied. These resonance conditions provide a nice guidance for the resonances of single element

nanoantenna [30] discussed in Chapter 2 and 3, and those of nanorod components, which are used to compose metasurfaces in Chapter 6, 7 and 8 with specific modifications.

Besides the scattering theory described above, the nanocircuit theory and transmission line theory are extremely important tools in modeling our designs of single-element nanoantennas [30]-[32], metasurfaces [33]-[35] and multilayer metasurfaces formed metamaterials [36]. The nanocircuit theory [37]-[39] and the surface impedance model [40] are discussed in chapter 4, chapter 5 and chapter 6. The transmission-line theory [41] is introduced in chapter 5, and is extensively applied in chapter 8. For extended reviews of the progress on metasurfaces, the readers can refer to [42],[43], and fundamentals and recent progress on optical metamaterials can be found in [29],[44]-[52].

Two major experimental manifestations of our ideas are also discussed in this dissertation. Both have been validated through conventional nanofabrication techniques and carried out using the facilities at the Microelectronic Research Center (MRC) located at the Pickle Research Campus (PRC) and the Center for Nano- and Molecular Science (CNMS) located at the main campus at the University of Texas at Austin. Fabrication and characterizations of these nanophotonic devices are detailed in chapter 7 and chapter 8.

1.5 REFERENCES

[1] http://nobelprize.org/nobel_prizes/medicine/laureates/1973/frisch-lecture.pdf

[2] http://larouchepac.com/node/17209

[3] Chiou, T. H. *et al*. Circular polarization vision in a stomatopod crustacean. Curr. Biol. 18, 429-434, (2008).

[4] Kleinlogel, S. and White, A. G. The secret world of shrimps: polarisation vision at its best. Plos One 3, (2008).

[5] Kartazayeva, S. A.; Ni, X. and Alfano, R. R. Optics Letters 30, 1168 (2005).

[6] Shalaev, V. M. *et al*. Negative index of refraction in optical metamaterials. Optics Letters 30, 3356-3358, (2005).

[7] Valentine, J. *et al.* Three-dimensional optical metamaterial with a negative refractive index. Nature 455, 376-U332, (2008).

[8] Liu, N., Guo, H.C., Fu, L.W., Kaiser, S., Schweizer, H., and Giessen, H. Three-dimensional photonic metamaterials at optical frequencies, Nature Materials, 7, pp. 31-37, (2008).

[9] Soukoulis, C.M., and Wegener, M. Past achievements and future challenges in the development of three-dimensional photonic metamaterials, Nature Photonics, 5, pp. 523-530, (2011).

[10] Brueck, S.R.J. Optical and interferometric lithography-Nanotechnology enablers, Proceedings of the IEEE, 93, pp. 1704-1721, (2005).

[11] Henzie, J., Lee, M.H., and Odom, T.W. Multiscale patterning of plasmonic metamaterials, Nature Nanotechnology, 2, pp. 549-554, (2007).

[12] Liu, N., Liu, H., Zhu, S.N., and Giessen, H. Stereometamaterials, Nature Photonics, 3, pp. 157-162, (2009).

[13] Maier, S. A., Brongersma, M. L., Kik, P. G., Meltzer, S., Requicha, A. A. G., Atwater, H. A. Plasmonics-A route to nanoscale optical devices, Advanced Materials, 13, pp. 1501-1505, (2001).

[14] Maier, S. A., Atwater, H. A. Plasmonics: Localization and guiding of electromagnetic energy in metal/dielectric structures, Journal of Applied Physics, 98, pp. 011101, (2005).

[15] Ozbay, E. Plasmonics: Merging photonics and electronics at nanoscale dimensions, Science, 311, pp. 189-193, (2006).

[16] Kuester, E.F., Mohamed, M.A., Piket-May, M., and Holloway, C.L. Averaged transition conditions for electromagnetic fields at a metafilm, IEEE Transactions on Antennas and Propagation, 51, pp. 2641-2651, (2003).

[17] Holloway, C.L., Mohamed, M.A., Kuester, E.F., and Dienstfrey, A. Reflection and transmission properties of a metafilm: With an application to a controllable surface composed of resonant particles, IEEE Transactions on Electromagnetic Compatibility, 47, pp. 853-865, (2005).

[18] Gordon, J.A., Holloway, C.L., and Dienstfrey, A. A physical explanation of angle-independent reflection and transmission properties of metafilms/metasurfaces, IEEE Antennas and Wireless Propagation Letters, 8, pp. 1127-1130, (2009).

[19] Beruete, M., Navarro-Cia, M., Falcone, F., Campillo, I., and Sorolla, M. Single negative birefringence in stacked spoof plasmon metasurfaces by prism experiment, Optics Letters, 35, pp. 643-645, (2010).

[20] Chen, P.Y., and Alù, A. Subwavelength Imaging Using Phase-Conjugating Nonlinear Nanoantenna Arrays, Nano Letters, 11, pp. 5514-5518, (2011).

[21] Alù, A., and Engheta, N. Tuning the scattering response of optical nanoantennas with nanocircuit loads, Nature Photonics, 2, pp. 307-310, (2008).

[22] Alù, A., and Engheta, N. Input impedance, nanocircuit loading, and radiation tuning of optical nanoantennas, Physical Review Letters, 101, pp. 043901, (2008).

[23] Sun, Y., Edwards, B., Alù, A., and Engheta, N. Experimental realization of optical lumped nanocircuits at infrared wavelengths, Nature Materials, 11, pp. 208-212, (2012).

[24] Alù, A. Mantle cloak: Invisibility induced by a surface, Physical Review B, 80, pp. 245115, (2009).

[25] Burokur, S.N., Daniel, J.P., Ratajczak, P., and de Lustrac, A. Tunable bilayered metasurface for frequency reconfigurable directive emissions, Applied Physics Letters, 97, pp. 064101, (2010).

[26] Bohren, C. F. and Huffman, D. R. Absorption and scattering of light by small particles. (John Wiley & Sons, Inc., 1983).

[27] Maier, S. A. Plasmonics: fundamentals and applications. (Springer, 2007).

[28] Sarid, D. and Challener, W. Modern instroduction to surface plasmons. (Cambridge University Press, 2010).

[29] Cai, W. and Shalaev, V. M. Optical Metamaterials: Fundamentals and Applications. (Springer, 2009).

[30] Liu, N. *et al*. Individual Nanoantennas Loaded with Three-Dimensional Optical Nanocircuits. Nano Letters 13, 142-147, (2013).

[31] Novotny, L. and van Hulst, N. Antennas for light. Nature Photonics 5, 83-90, (2011).

[32] Zhao, Y.; Engheta, N. and Alù, A. Effects of shape and loading of optical nanoantennas on their sensitivity and radiation properties. Journal of the Optical Society of America B-Optical Physics 28, 1266-1274, (2011).

[33] Zhao, Y. and Alù, A. An Ultrathin Quarter-Wave Nano-Plate Based on Detuned Plasmonic Nanoantennas. In IEEE Antennas and Propagation Society International Symposium (2012).

[34] Zhao, Y. and Alù, A. Manipulating light polarization with ultrathin plasmonic metasurfaces. Physical Review B 84, (2011).

[35] Zhao, Y. and Alù, A. Tailoring the Dispersion of Plasmonic Nanorods To Realize Broadband Optical Meta-Waveplates. Nano Letters 13, 1086, (2013).

[36] Zhao, Y.; Belkin, M. A. and Alù, A. Twisted optical metamaterials for planarized ultrathin broadband circular polarizers. Nature Communications 3, (2012).

[37] Engheta, N. Circuits with light at nanoscales: Optical nanocircuits inspired by metamaterials. Science 317, 1698-1702, (2007).

[38] Alù, A. and Engheta, N. Tuning the scattering response of optical nanoantennas with nanocircuit loads. Nature Photonics 2, 307-310, (2008).

[39] Schnell, M. *et al*. Controlling the near-field oscillations of loaded plasmonic nanoantennas. Nature Photonics 3, 287-291, (2009).

[40] Zhao, Y.; Engheta, N. and Alù, A. Homogenization of plasmonic metasurfaces modeled as transmission-line loads, Metamaterials 5, pp. 90-96 (2011).

[41] Pozar, D. M. Microwave Engineering. (John Wiley & Sons, 2012).

[42] Kildishev, A.; Boltasseva, A. and Shalaev, V. Planar Photonics with Metasurfaces. Science 339, 1232009, (2013).

[43] Holloway, C. L. *et al*. An Overview of the Theory and Applications of Metasurfaces: The Two-Dimensional Equivalents of Metamaterials. Ieee Antennas and Propagation Magazine 54, 10-35, (2012).

[44] Linden, S. *et al*. Magnetic response of metamaterials at 100 terahertz. Science 306, 1351-1353, (2004).

[45] Pendry, J. B. Negative refraction. Contemporary Physics 45, 191-202, (2004).

[46] Zhang, S. *et al.* Experimental demonstration of near-infrared negative-index metamaterials. Physical Review Letters 95, (2005).

[47] Soukoulis, C. M.; Kafesaki, M. and Economou, E. N. Negative-index materials: New frontiers in optics. Advanced Materials 18, 1941-1952, (2006).

[48] Cai, W. S.; Chettiar, U. K.; Kildishev, A. V. and Shalaev, V. M. Optical cloaking with metamaterials. Nature Photonics 1, 224-227, (2007).

[49] Alù, A. and Engheta, N. Plasmonic and metamaterial cloaking: physical mechanisms and potentials. Journal of Optics a-Pure and Applied Optics 10, (2008).

[50] Chen, H. Y.; Chan, C. T. and Sheng, P. Transformation optics and metamaterials. Nature Materials 9, 387-396, (2010).

[51] Luk'yanchuk, B. *et al.* The Fano resonance in plasmonic nanostructures and metamaterials. Nature Materials 9, 707-715, (2010).

[52] Soukoulis, C. M. and Wegener, M. Past achievements and future challenges in the development of three-dimensional photonic metamaterials. Nature Photonics 5, 523-530, (2011).

Chapter 2: Single Element Plasmonic Nanoantennas as Building Blocks and Nanocircuit Theory

In order to build metamaterials with the superior functionalities introduced in Chapter 1, we start with studying the basic building blocks: single element nanoantennas. In this chapter and the next, we will discuss the design and analysis of single element nanoantennas and their circuit theory as the foundations of this study. Designing single element nanoantennas, and more specifically, studying their shape effects on the sensitivity tuning and radiation efficiencies enables us to proceed to more complicated designs on the two-dimensional (2D) nanoantenna arrays (metasurfaces), and multilayer stacking of the metasurfaces as metamaterials.

In this chapter, we will focus on analyzing the relations between radiation properties and sensitivity of optical nanoantennas and their shape and design parameters using the nanocircuit concepts. We apply these findings to optimize the sensitivity and bandwidth of printed plasmonic nanoantennas, which could be applied not only in the proposed functions that we aim to achieve, but could also have impact on optical communications and label-free bio-sensing applications, for which we provide an example of employing these single element nanostructures and their nanocircuit design principles in bio-sensing applications at the end of this chapter. In comparison to conventional plasmonic optical sensors, which mainly rely on localized surface plasmons, our design rules suggest that optical nanoantennas may provide enhanced sensitivity for biomedical applications, and our analytical solutions based on their equivalent nanocircuit model may provide an efficient tool for their design optimization. Several numerical simulations are presented to verify utility of this design method, providing excellent agreement between numerical and analytical results.

2.1 INTRODUCTION

At microwave and radio frequencies (RF), an antenna is designed as a transducer to convert free-propagating electromagnetic waves into confined electric currents, and vice versa. With the progress of nanofabrication technology, it is now becoming feasible to fabricate analogous devices in the nanometer range, as optical nanoantennas [1]-[4]. Due to their nanometer size, optical nanoantennas are not only useful as emitters or receivers, but they have other appealing properties, such as sub-diffraction field confinement and optical near field enhancement [5]-[7]. These properties have led to several important applications, including high resolution microscopy [8],[9], single molecular sensing and spectroscopy [2],[3],[10]-[12], enhancement of photovoltaic energy conversion efficiency [13], near-field nanofabrication [14], solid state light emission enhancement [15]-[17], single photon sources [18], and optical communications [19]-[22].

The functionality of optical nanoantennas, however, differs considerably from their RF counterparts [20],[23], and their analysis and design rules should obviously be accordingly modified. For instance, the resonance condition of RF antennas, which usually resonate when their characteristic size is comparable to half-wavelength, does not directly apply to optical antennas [23]. This is due to the fact that metals are dispersive and have finite conductivities in the optical regime, supporting surface plasmon polaritons (SPPs) with considerably shorter wavelengths than that of free-space. Due to SPPs, the nanoantenna resonance frequency strongly depends on its transverse size, shape and material properties. Sensitivity and bandwidth of these devices are also similarly affected.

The strong field confinement and nanoscale size makes nanoantennas one of the ideal devices for biological sensing [24],[25], since the presence of small molecules at

their load may alter their frequency response. Their design and optimization as bio-sensors, however, has been often empirical, due to their complex interaction with the optical signal and their plasmonic properties, and has been in general limited to maximizing their field enhancement at the sample location [26].

In this chapter, we develop certain design methodologies for optical nanoantennas and apply these nanodevices for bio-sensing applications and optical communications, properly taking into account their plasmonic and displacement effects. Our work applies the optical nanocircuit concepts [27],[28] to this problem, consistent with some earlier works that have defined the optical impedance and radiation properties of interest for several nanoantenna geometries [20],[21],[29]. In the past, these concepts have been applied to properly tuning [19], loading [20] and matching [22] optical nanoantennas, whereas here we focus on modeling the features of bandwidth, efficiency and sensitivity of these loaded nanoantennas that are of particular interest for bio-sensing and communication applications. We show how the proper definition and calculation of the 'intrinsic' optical impedance of the nanoantennas of interest, which is a complex function of its size, shape and material properties, allows characterization of its functionality as a sensor, and in particular its resonance frequency, bandwidth and sensitivity to the variations in the antenna shape and loading materials. This result may provide useful guidelines for optimization of the design of optical antennas as sensing elements or nanoprobes in optical microscopy and spectroscopy, and also as building blocks of the plasmonic metamaterials for polarization manipulation.

2.2 THEORETICAL MODEL

Without loss of generality, we focus our analysis on flat nanoantenna geometries loaded at their center by a nanoparticle, as depicted in Figure 2.1. These nanoantennas

may be easily printed on a transparent substrate using standard lithographic techniques. In Figure 2.1 we have reported three typical nanoantenna geometries of interest: (a) the nanodipole, (b) the nanobowtie and (c) the nanodimer antenna. The three shapes may all effectively be reduced to the nanobowtie geometry in Figure 2.1(b) in the limit in which the arm angle α tends to 0 or 180 degrees, respectively. The nanoantenna thickness d, gap size g, arm angle α and arm length L are suitably varied to investigate how they affect the nanoantenna resonance, sensitivity and bandwidth of operation. In order to compare the different nanoantenna geometries, their properties have been compared by varying the nanoparticle loads placed at their gap.

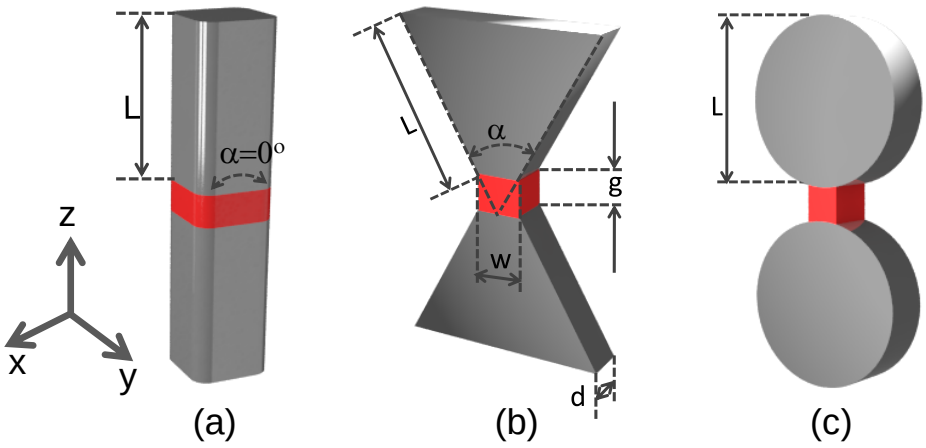

Figure 2.1: Nanoantenna geometries of interest, with the angle α ranging between 0 and 180 degrees, corresponding to: (a) nanodipole, (b) nanobowtie, and (c) nanodimer antennas. (Reproduced with permission from JOSA B, Vol. 28, Issue 5, pp. 1266-1274 (2011). Copyright 2011 Journal of Optical Society of America)

Our full-wave numerical simulations are obtained using commercially available software based on time-domain finite integration technique [30], and excited using two different approaches: (a) a discrete current source element placed at the center of the gap across the two arms, aligned along the y axis, in the unloaded case ($\varepsilon_L = \varepsilon_0$ at the gap),

is used to determine the reflection coefficient at the feed versus frequency, the optical input impedance and the optical radiation efficiency, as defined in [20],[22]; (b) a plane wave with electric field linearly polarized along the y axis and incident along the z direction, is employed to analyze the far-field scattering properties in the loaded and unloaded scenarios, varying the permittivity at the gap. We have assumed all the nanoantennas to be composed of silver, modeled with the Drude permittivity model [31] $\varepsilon_{Ag} = \varepsilon_0 \left\{ \varepsilon_\infty - f_p^{\,2} / \left[f \left(f - i\gamma \right) \right] \right\}$, where $\varepsilon_\infty = 5$, $f_p = 2.175\,\mathrm{PHz}$ and $\gamma = 4.35\,\mathrm{THz}$. An $\exp\left(-i\omega t\right)$ time dependence has also been assumed.

In order to analyze the nanoantenna sensitivity to variations in the load, different dielectric materials and combinations of them, with permittivity ranging between $\varepsilon_L = \varepsilon_0$ and $\varepsilon_L = 5\varepsilon_0$, have been considered in the gap region. Following our results in [19],[20], the nanoantenna interaction with the load may be accurately quantified by modeling the nanoantenna response as a single nanocircuit element with 'intrinsic' optical impedance $Z_a = R - iX$, where R is the nanoantenna intrinsic resistance and X is the corresponding reactance. The intrinsic impedance of the nanoantenna depends in a complex way on the material properties and on its geometry, and it may be calculated by driving the nanoantenna at its gap with an optical source. Effectively, Z_a is defined as the ratio between the effective voltage applied across the antenna arms and the optical displacement current flowing through the gap. As we show in the following, its value fully characterizes the nanoantenna interaction with any arbitrary load placed at its gap, with generic impedance Z_L. For instance, in the case of a single homogeneous nanodisk filling the gap, the total optical impedance of the nanoantenna Z_{in} at the gap is easily calculated from Z_a using the circuit model in Figure 2.2(a), with $Z_L = ig / \omega\varepsilon_L S$ and $S = wd$ [19],[20]. Variations at the load may be directly taken into account in the equivalent circuit model of Figure 2.2(a), as the complex antenna response is completely

described by its intrinsic impedance Z_a. In the case of two nanoloads stacked vertically in the gap, with thickness ζ and $g-\zeta$, their optical impedances are effectively connected in series [19],[32],[33], and the corresponding model is given in Figure 2.2(b). Conversely, for nanoparticles stacked horizontally within the gap, with width ξ and $w-\xi$, the corresponding circuit model is the one in Figure 2.2(c), with the load impedances displaced in parallel. Despite their simplicity, these nanocircuit models are very effective quantitative descriptions of the nanoantenna interaction with the load. Indeed, in the earlier theoretical work, they have been used to tune [19] and match the nanoantenna to an incoming optical feeding line [22]. Here we show that they may also be used to predict and optimize the nanoantenna sensitivity and bandwidth of operation.

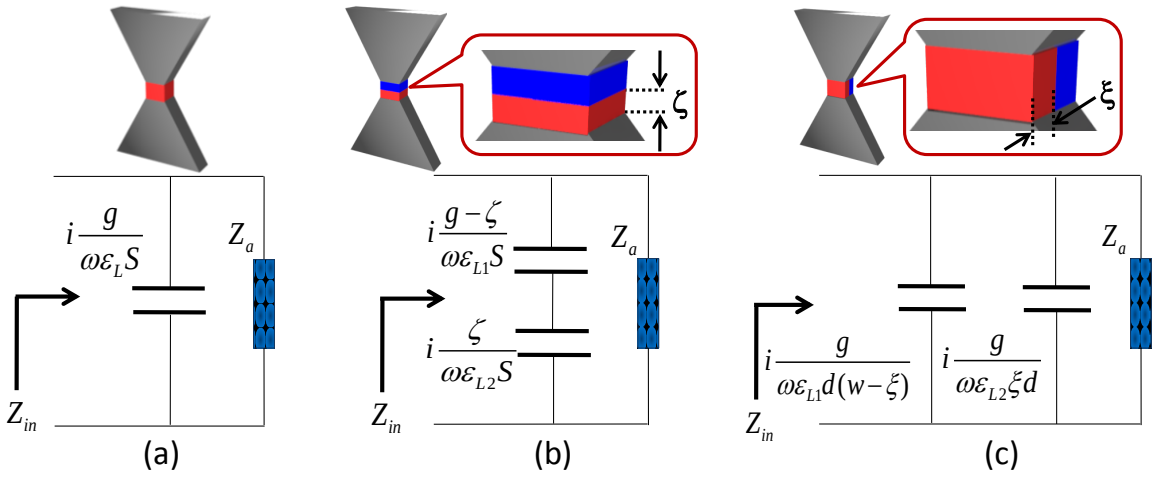

Figure 2.2: Nanocircuit model for the optical input impedance with different loads at the gap of the nanoantennas in Figure 2.1. (a) Nanoantenna with one homogeneous nanoparticle at the gap, (b,c) nanoantenna with two nanoparticles with different permittivity ε_{L1} and ε_{L2} connected in series (b) and parallel (c). The insets show the corresponding sketches of the different load configurations. (Reprinted with permission from JOSA B, Vol. 28, Issue 5, pp. 1266-1274 (2011). Copyright 2011 Journal of Optical Society of America)

In the unloaded case (Figure 2.2 (a) with $\varepsilon_L = \varepsilon_0$), the input impedance may be simply written as:

$$Z_{in} = \frac{1}{\dfrac{1}{R - iX} - i\omega C}, \tag{2.1}$$

where $C = \varepsilon_0 S / g$ is the nanocapacitance of the empty gap. In particular, the real and imaginary parts of the input impedance $Z_{in} = r_0 - ix_0$ may be written as:

$$r_0 = \frac{R}{1 + C\omega\left(-2X + C\left(R^2 + X^2\right)\omega\right)}, \tag{2.2}$$

$$x_0 = \frac{X - C\left(R^2 + X^2\right)\omega}{1 + C\omega\left(-2X + C\left(R^2 + X^2\right)\omega\right)}. \tag{2.3}$$

Solving for the real and imaginary parts of the intrinsic impedance we find:

$$R = \frac{r_0}{1 + C\omega\left(2x_0 + C\left(r_0^{\,2} + x_0^{\,2}\right)\omega\right)}, \tag{2.4}$$

$$X = \frac{x_0 + C\left(r_0^{\,2} + x_0^{\,2}\right)\omega}{1 + C\omega\left(2x_0 + C\left(r_0^{\,2} + x_0^{\,2}\right)\omega\right)}, \tag{2.5}$$

which are the formulas we effectively utilize to de-embed the intrinsic impedance of the nanoantenna from the full-wave simulations of the unloaded geometry fed at its gap by a current source.

When a homogeneous load with permittivity ε_L is placed at the gap, the modified capacitance $C_L = \varepsilon_L S / g$, modifies the input impedance into $Z_{inl} = r_l - ix_l$, with:

$$r_l = \frac{g^2 R}{g^2 - 2gSX\varepsilon_L\omega + S^2\left(R^2 + X^2\right)\varepsilon_L^{\,2}\omega^2}, \tag{2.6}$$

$$x_l = \frac{g\left[gX - S\left(R^2 + X^2\right)\varepsilon_L\omega\right]}{g^2 - 2gSX\varepsilon_L\omega + S^2\left(R^2 + X^2\right)\varepsilon_L^{\,2}\omega^2}. \tag{2.7}$$

The parallel 'open-circuit' resonance frequency of the nanoantenna, which corresponds to the resonant scattering condition in the receiving regime and to the frequency of maximum matching from a feeding optical line [19],[22], is obtained when r_l is maximum and $x_l = 0$, i.e., at the radian frequency

$$\omega_0 = \frac{gX}{S\left(R^2 + X^2\right)\varepsilon_L}. \tag{2.8}$$

The above equation implies that, with increasing permittivity at the gap, the resonance frequency decreases, consistent with our numerical results in [19]. It is interesting to note that, since $|X| \gg R$ at this resonance, due to the short electrical length of the nanoantenna, Eq. (2.8) also implies:

$$\frac{1}{X} \cong \frac{\varepsilon_L \omega_0 S}{g} = \frac{1}{\mathrm{Im}\left[Z_L\right]\Big|_{\omega_0}}, \tag{2.9}$$

as expected by the LC parallel resonant circuit at the gap.

The sensitivity of the nanoantenna $\mathbb{S}$ at such resonance frequency ω_0 may be defined as the derivative of Eq. (2.8) with ε_L:

$$\mathbb{S} = \frac{\partial \omega_0}{\partial \varepsilon_L} \approx -\frac{gX}{S\left(R^2 + X^2\right)\varepsilon_L{}^2}\Bigg|_{\omega_0}. \tag{2.10}$$

The nanoantenna sensitivity strongly depends on the value of intrinsic impedance at the frequency of interest. Proper choice of the nanoantenna geometrical parameters may optimize the sensitivity $\mathbb{S}$ for the applications of interest. For a given nanoantenna geometry, more flexibility may be obtained by using cascaded loads, as in Figure 2.2(b) and 2.2(c). In the series case as depicted in Figure 2.2(b), the overall capacitance is:

$$C = \frac{S}{\frac{(g-\zeta)}{\varepsilon_{L1}} + \frac{\zeta}{\varepsilon_{L2}}}. \tag{2.11}$$

The corresponding resonance frequency ω_0 and sensitivity $\mathbb{S}$ of the nanoantenna become:

$$\omega_0 = \frac{gX\varepsilon_{L2} + X\zeta(\varepsilon_{L1} - \varepsilon_{L2})}{S(R^2 + X^2)\varepsilon_{L1}\varepsilon_{L2}}, \tag{2.12}$$

$$\mathbb{S} = \frac{\partial\omega_0}{\partial\varepsilon_{L2}} \approx -\frac{X\zeta}{S(R^2 + X^2)\varepsilon_{L2}^{\ 2}}, \tag{2.13}$$

where $\mathbb{S}$ is defined as the sensitivity to variations in the load with permittivity ε_{L2}.

Similarly, for the parallel configuration $C = \varepsilon_{L1}(w-\xi) + \varepsilon_{L2}\xi$ and the resonance frequency ω_0 and sensitivity $\mathbb{S}$ become:

$$\omega_0 = \frac{X}{(R^2 + X^2)\left[\varepsilon_{L1}w + \xi(\varepsilon_{L2} - \varepsilon_{L1})\right]}, \tag{2.14}$$

$$\mathbb{S} = \frac{\partial\omega_0}{\partial\varepsilon_{L2}} \approx -\frac{X\xi}{(R^2 + X^2)\left[\varepsilon_{L1}(w-\xi) + \varepsilon_{L2}\xi\right]^2}. \tag{2.15}$$

It is evident how the resonance frequency and nanoantenna sensitivity may be tailored to a large degree by combining different nanocircuit loads at the gap. It is relevant to stress that the formulas derived here allow a semi-analytical quantitative prediction and optimization of the nanoantenna parameters of interest for applications such as biosensing, which may be deduced after a single numerical simulation of the unloaded nanoantenna driven at the gap. Moreover, once the intrinsic impedance is calculated, the resonance frequency and sensitivity of the nanoantenna may be tailored by properly selecting the load impedance in optical communication applications. Sensitivity is also directly related to the bandwidth of these nanoantennas, which may be tailored using similar concepts.

Before concluding this section, we would like to emphasize that, despite the fact that the nanocircuit concepts have been originally developed by assuming uniform plane-wave-like excitation [28], these results are not a function of the specific form of excitation. In fact, the only assumption in deriving Eq. (2.1) is that the field impinging on the nanoantenna may be approximated by its local value at the gap location, assumption that is valid and justifiable for the typical sub-wavelength size of these devices. This implies that even in typical biosensing measurements, which may require focused beams and confocal microscopy for the proper nanoantenna excitation, the dominant mechanisms would be analogous to those verified in the present work and modeled by nanocircuit concepts. These concepts break down for larger objects, with sizes comparable with the wavelength of operation, for which local variations of the impinging field and excitation of higher-order modes may become relevant.

2.3 EFFECTS OF THE NANOANTENNA GEOMETRY ON ITS SENSITIVITY FOR BIOSENSING APPLICATIONS

In this section we apply the previous theoretical results to biosensing applications, presenting several numerical examples that show how the sensitivity and resonance frequency shift of the nanoantenna geometries of Figure 2.1 may be predicted with semi-analytical tools. We also discuss how the nanoantenna shape and geometry affects these resonance properties. Two series of numerical simulations were conducted using different gap dimensions for the same ratio g/S (in order to keep the gap capacitance in the unloaded case constant), comparing resonance frequency, sensitivity and radiation efficiency. The first set of nanoantennas has gap dimensions $5\times10\times20\,nm^3$, and the second set $10\times20\times20\,nm^3$, where the three numbers denote $g\times w\times d$. For the nanodimer scenario, analogous gap dimensions were used, except for minor modifications due to the curvature at the gap terminals.

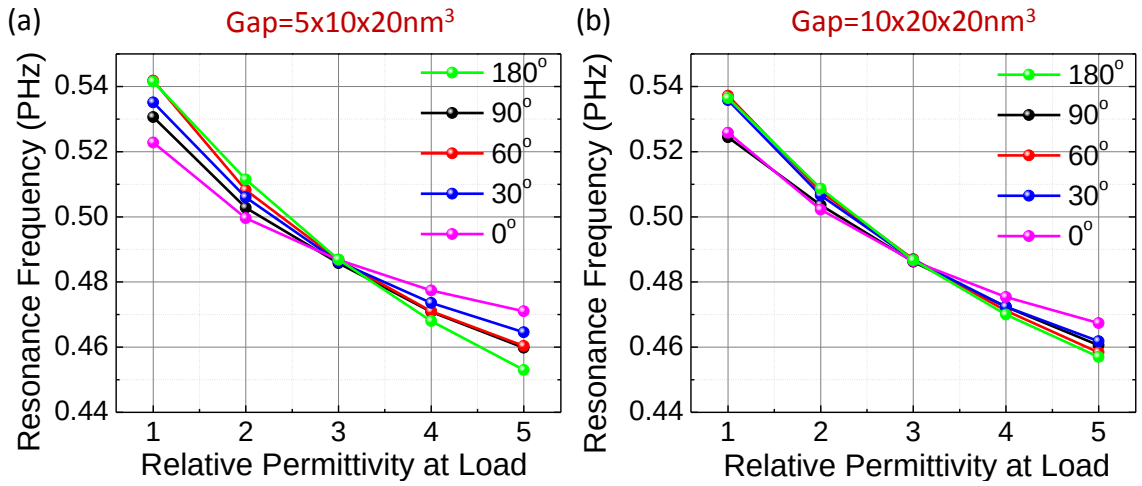

Figure 2.3: Variation of the resonance frequency with the load permittivity for different angles α, for two different gap sizes. (Reprinted with permission from JOSA B, Vol. 28, Issue 5, pp. 1266-1274 (2011). Copyright 2011 Journal of Optical Society of America)

Table 2.1: Nanoantenna Arm Length

Angle α	Gap=5×10×20 nm^3	Gap=10×20×20 nm^3
	Arm Length (nm)	Arm Length (nm)
0^o	32	50.5
30^o	41	55
60^o	45.9	58.9
90^o	47	59.85
180^o	71.8	84

Figure 2.3 shows the full-wave numerical simulations for the variation of resonance frequency ω_0 with the load permittivity (for the case of Figure 2.2(a)), for the two sets of gap dimensions, varying the nanoantenna shape via the angle α. For each

angle, in order to provide a fair comparison among different geometries, each nanoantenna arm length has been properly tuned in order to support the resonance at the design frequency $f_0 = 486.4THz$ for a load permittivity $\varepsilon_L = 3\varepsilon_0$. This choice for the comparison among different nanoantenna designs stems from the fact that the absorption loss in plasmonic nanoantennas is dominated by the vAlùe of imaginary part of the metal permittivity at the resonance frequency, rather than its overall length or volume. The corresponding arm lengths are reported in Table 2.1, where it is evident how an increasing arm angle α corresponds to a longer arm length for fixed resonance frequency f_0, which is a typical feature of plasmonic nanoantennas [20],[23].

As predicted by Eq. (2.8), the resonance frequency is inversely proportional to the load permittivity in each scenario, with a slope determined by the intrinsic impedance of the nanoantenna at the frequency of interest. We have verified that the numerical simulations completely agree with the analytical result in Eq. (2.8). This comparison is explicitly reported in Figure 2.4 for the case $\alpha = 60^o$, where we have compared the analytical and numerical curves of the input resistance versus frequency in the case of a driven nanoantenna varying the loading material from $\varepsilon_L = \varepsilon_0$ to $\varepsilon_L = 5\varepsilon_0$. The resonance frequency corresponds to the position of the maximum input resistance, which, consistent with our nanocircuit model in Figure 2.2(a), shifts to lower frequencies and to smaller values for increased gap capacitance. In particular, Figure 2.4 shows the comparison of the resonance frequencies between numerical and analytical results for $\alpha = 60^\circ$ nanobowtie antenna with gap dimension $5 \times 10 \times 20 nm^3$. It is seen that the discrepancy is very minor, and indeed our analytical method provides an excellent approximation for the overall radiation and impedance properties of the nanoantennas under consideration. Similar plots have been obtained for the other geometries in Figure 2.3. The sensitivity at the design frequency is given in Figure 2.3 by the slope of the different curves, and it

coincides with the analytical value in Eq. (2.10) for all the considered examples. Inspecting the results of Figure 2.3, we find that the nanodimer antenna may provide the highest sensitivity among the considered designs. Among the bowtie nanoantennas, the $\alpha = 60^{\circ}$ design provides the largest sensitivity.

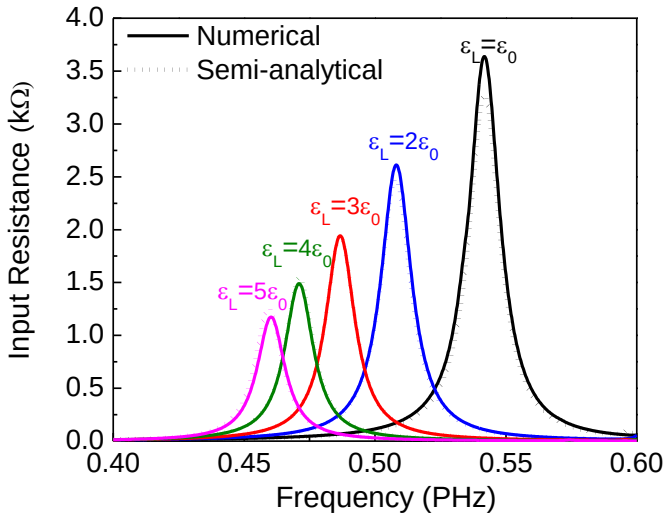

Figure 2.4: Comparison of numerical simulation (solid curves) and calculated input impedance using the semi-analytical approach presented in the previous section (dashed). (Reprinted with permission from JOSA B, Vol. 28, Issue 5, pp. 1266-1274 (2011). Copyright 2011 Journal of Optical Society of America)

It is interesting to underline that, for the antenna to resonate, the intrinsic reactance of the nanoantenna is required to be opposite to the load reactance $-1/\omega C$, as shown in Eq.(2.9). This implies that a larger sensitivity is directly related to a less steep variation of the intrinsic reactance, for which a small variation in C would produce a larger deviation in frequency. Figure 2.5 indeed shows this concept: in Figure 2.5(a) we report the variation of the calculated intrinsic reactance for the nanoantennas of Figure 2.2(a). As expected, the curves all meet at the design frequency f_0, at the reactance value $X = \left[g + \left(g^2 - 36R^2S^2\varepsilon_0{}^2\omega_0{}^2 \right)^{1/2} \right] / 6S\varepsilon_0\omega_0$, which ensures that all the

nanoantennas resonate at the same frequency for a load with $\varepsilon_L = 3\varepsilon_0$. Figure 2.5(b) reports the zoom of this plot around the resonance frequency, showing how the nanodimer and the $\alpha = 60^\circ$ nanobowtie antenna indeed exhibit the lowest slopes around the design frequency. This in turn results in the largest sensitivity to the load permittivity, which would be relevant to optimize the nanoantenna for bio-sensing applications.

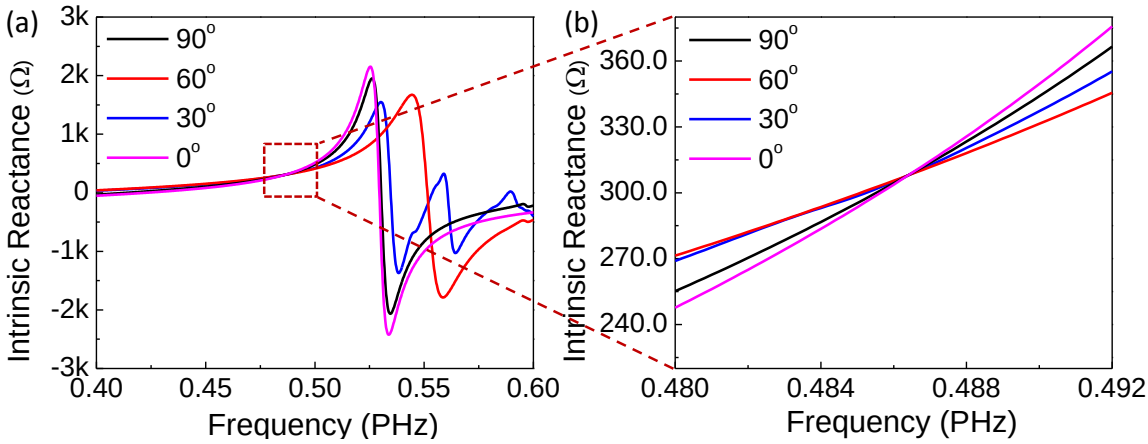

Figure 2.5: Numerically calculated intrinsic impedance for the nanoantennas with gap dimension $5\times10\times20nm^3$ for different antenna geometries, where the legend indicates the arm angle α. The dashed square region in panel (a) is enlarged in panel (b) in the vicinity of the resonance frequency f_0. (Reprinted with permission from JOSA B, Vol. 28, Issue 5, pp. 1266-1274 (2011). Copyright 2011 Journal of Optical Society of America)

It is seen that proper selection of the nanoantenna geometry may optimize the sensitivity and resonance frequency, and further flexibility in tuning the resonance at the frequency of desired sensitivity may be achieved using parallel or series combinations of loads, partially prefabricated at the gap and partially left empty for detection of bio-target. Figure 2.6 shows two examples of series and parallel loading, using materials with permittivity ε_{L1} and ε_{L2} equal to $3\varepsilon_0$ and $2\varepsilon_0$, respectively. In these examples, we have assumed that the bio-target has a relative permittivity around 2, and the gap is

partially filled with a material with relative permittivity 3. As shown in Figure 2.6(a), by varying the filling factor at the gap, parameter ζ of ε_{L2} we may be able to sensibly shift the resonance frequency. Similarly as in the parallel case shown in Figure 2.6(b), the parameter ξ was varied, with a higher percentage of the filling of the target material ε_{L2}, a blue shift of the resonance frequency is observed. In both cases, the shift of the resonance frequency in Figure 2.6 follows the theoretical predictions in Eq.(2.12) and Eq.(2.14), respectively. In order to make these results closer to their practical application for biosensing, we have also compared the achieved values of sensitivity with the values usually required for effective biomedical sensing. We consider, as an example a Concanavalin A (ConA) sensor, whose single protomer size is around $4.2\times4.0\times3.9\ nm^3$ [34]. The bio-target is usually immersed in a buffer solution, with refractive index around 1.33, and the refractive index of ConA is 1.57 [35]. The nanoantenna's narrow gap, acting as a tiny slot, makes detection of single molecule possible, which is a relevant advantage over other biosensing devices that usually require a much larger amount of sample. When the protein molecule passes through the nanoantenna's gap, a typical index variation from 1.33 to 1.57 is expected. Using these values, we expect a resonance shift of ~20 nm, as shown by the results in Figure 2.7.

The resonance frequency decreases linearly with a refractive index variation from 1 (air) to 1.33 (buffer solution) and 1.57(ConA). The corresponding sensitivity is around 83nm per RIU, which is comparable with other current biosensing techniques [36],[37]. In addition to the resonance shift, also the intensity of scattered field is expected to vary even more dramatically with respect to the index change at the gap. The variation of radiation resistance in Figure 2.4 is a good measure of such variation. We have calculated that for a 60 degree bowtie nanoantenna, the total scattered intensity drops 73.52% when the index at gap varies within this same range (from 1.33 to 1.57), ensuring significant

sensitivity for biomedical applications. This may represent an interesting alternative venue for biosensing.

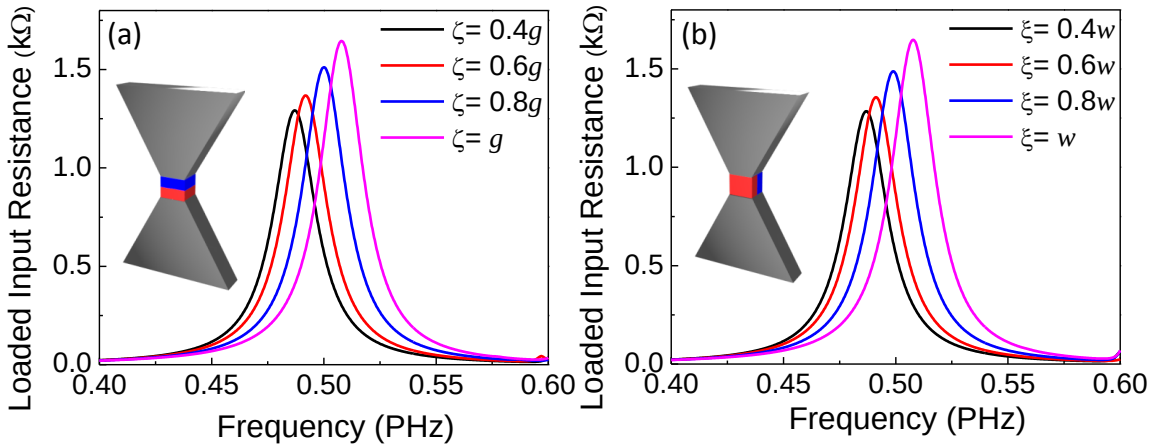

Figure 2.6: Tuning the nanoantenna resonance frequency with: (a) series loading, and (b) parallel loading. The corresponding loading geometries at the gap are shown in the insets of Figure 2.2(b) and Figure 2.2(c), respectively. With increasing the filling of the material with $\varepsilon_{L2} = 2\varepsilon_0$, the resonance frequency shifts to higher value. (Reprinted with permission from JOSA B, Vol. 28, Issue 5, pp. 1266-1274 (2011). Copyright 2011 Journal of Optical Society of America)

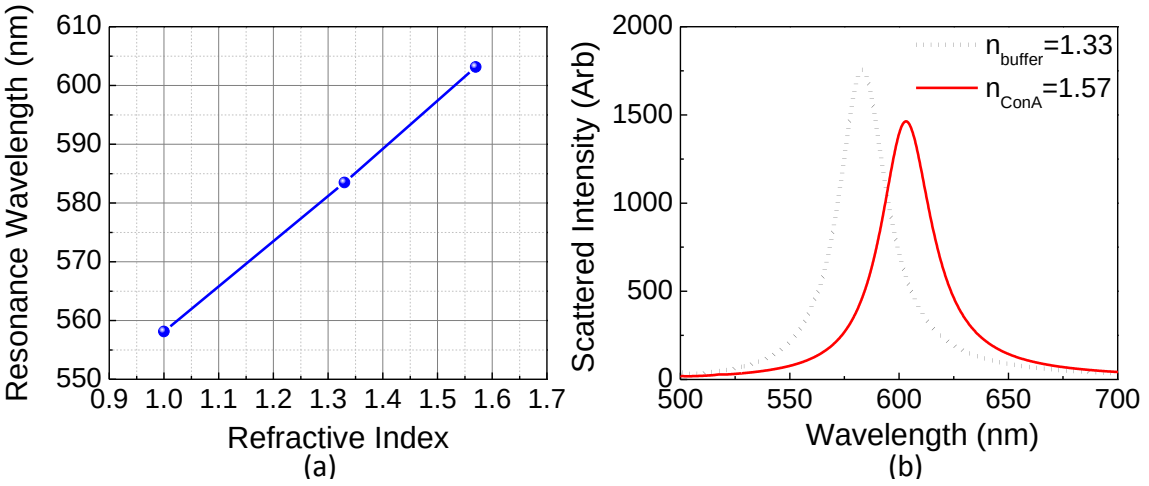

Figure 2.7: (a) Refractive index change of 60° nanoantenna with no series and parallel components inserted in the gap region, (b) the relative scattered intensity drop due to the change of index at the gap. (Reprinted with permission from JOSA B, Vol. 28, Issue 5, pp. 1266-1274 (2011). Copyright 2011 Journal of Optical Society of America)

2.4 EFFECTS OF THE NANOANTENNA GEOMETRY ON ITS RADIATION EFFICIENCY AND BANDWIDTH FOR OPTICAL COMMUNICATIONS

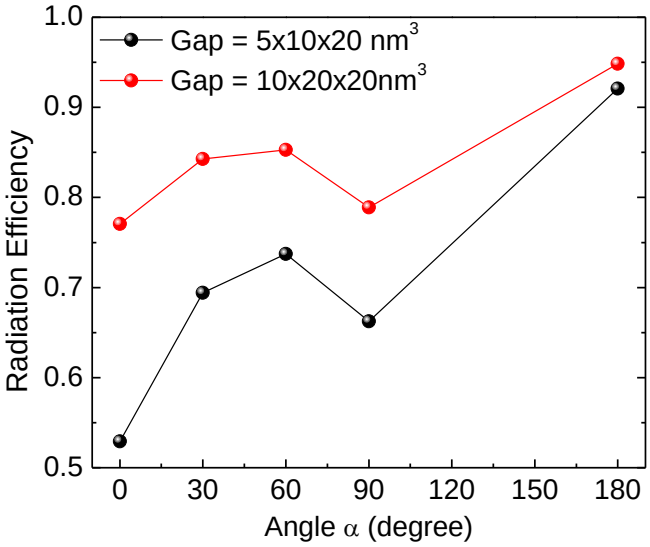

Figure 2.8: Comparison of simulated radiation efficiencies for different geometries, varying the angle α and the gap dimensions. (Reprinted with permission from JOSA B, Vol. 28, Issue 5, pp. 1266-1274 (2011). Copyright 2011 Journal of Optical Society of America)

Other relevant parameters characterizing the nanoantenna operation are its optical radiation efficiency η_{rad} and its overall bandwidth of operation, which are of interest for optical communications [22]. We define η_{rad}, in accordance with [20], as the ratio of radiated versus accepted power at the gap for a radiating nanoantenna, which is a measure of the robustness to absorption. In [21] we have shown that the nanodimer antenna may provide better radiation efficiency compared to the nanodipole, due to the reduced confinement of the SPP traveling along the nanoantenna arms. In Figure 2.8 we report our calculations for the overall radiation efficiency of the nanoantennas of Figure 2.3 at the design frequency f_0, as a function of their geometry. It can be seen that a bigger gap may provide higher radiation efficiency, without necessarily producing lower sensitivity (as seen in Figure 2.3). Moreover, the nanodipole antenna provides

significantly worse radiation efficiency than any other nanoantenna geometry, whereas the nanodimer ensures the largest efficiency among these antennas. It is interesting to underline that in a regular RF antenna large sensitivity is usually associated with a higher Q-factor, which implies smaller bandwidths, lower robustness to loss, and a usually lower overall radiation efficiency.

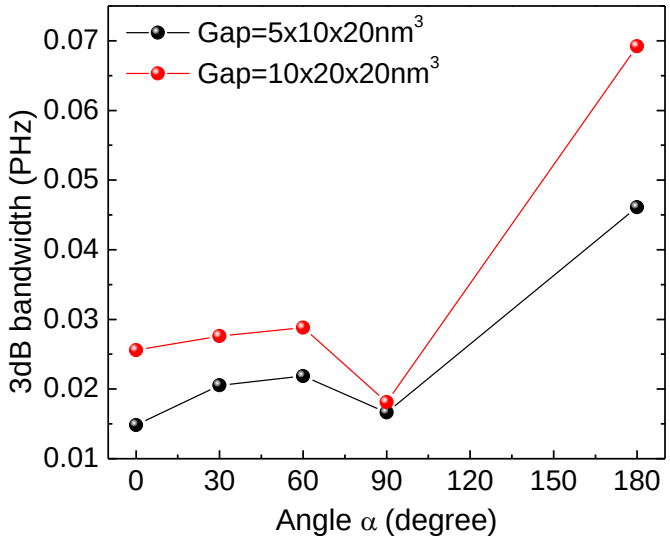

Figure 2.9: 3dB bandwidth extracted from the simulated nanoantenna polarizability. The red dots represent bandwidth of large gap with dimension $10\times10\times20\ nm^3$. The black dots represent bandwidth of small feedgap with dimension $5\times10\times20\ nm^3$. (Reprinted with permission from JOSA B, Vol. 28, Issue 5, pp. 1266-1274 (2011). Copyright 2011 Journal of Optical Society of America)

The plasmonic nature of these nanoantennas, however, reflects in an opposite trend: larger nanoantenna volumes (i.e., the nanodimer or the $\alpha = 60^\circ$ nanobowtie antenna) ensure less field confinement in the metal, which is reflected in larger efficiency and radiation resistance. At the same time, the increased confinement of the fringing fields at the gap ensures also increased sensitivity. The nanodimer shows a level of sensitivity comparable with the 60 degree nanobowtie antenna, but larger radiation

efficiency, associated with the absence of corners, which are associated with stronger confinement of the electric field, enhanced Ohmic losses and localized absorption.

The nanoantenna bandwidth of operation may be defined in terms of its scattering properties, when illuminated by an external plane wave, as in [19], or in terms of its reflection coefficient at the gap, when fed by a matched optical line as in [20]. We have numerically verified that the resonance frequency in both scenarios is well described by Eqs. (2.8)-(2.14) and the bandwidth of operation is also comparable in the two functionalities. We have calculated the 3dB bandwidth in terms of the maximum scattering peak for the nanoantennas in Figure 2.1(b) with varying arm angle for a load $\varepsilon_L = 3\varepsilon_0$ at the design frequency f_0, as reported in Figure 2.9. Also in this case, maximized bandwidth of operation is achieved for the nanodimer antenna.

Figure 2.10, in particular, reports the variation of polarizability associated with the nanoantennas analyzed here, a direct measure of their far-field scattering properties when illuminated by an external plane wave, compared with the corresponding variation of the reflection coefficient when fed at their gap. As expected, for any load and any nanoantenna geometry, a direct relation between the scattering resonances and the nanoantenna matching conditions are verified, implying that the two features are indeed both associated with the open-circuit resonance frequency ω_0. In the figure, the amplitudes of the polarizability are renormalized to the factor $k_0^3 / 6\pi\varepsilon_0$, consistent with [38]. We report in the figure for each nanoantenna geometry the corresponding electric and magnetic field distributions on the E plane at the resonance frequency when loaded with $\varepsilon_L = 3\varepsilon_0$.

2.5 CONCLUSIONS

In this chapter, we have discussed the complex relationship between the shape and geometry of optical nanoantennas and their sensitivity to the load variation, their radiation efficiency and bandwidth of operation. The optical nanocircuit concepts have been used as a useful tool for interpreting these effects in terms of the load variation and the corresponding modification of the intrinsic impedance at the gap, in order to design and optimize the nanoantenna parameters, to increase the nanoantenna sensitivity and to improve its overall radiation properties. We have shown, in particular, that the dimer and specific bow-tie configurations may provide optimal performance in terms of sensitivity, efficiency and bandwidth of operation. Distinct features stemming from the plasmonic nature of these nanoantennas have been also discussed. Finally, the reported full-wave numerical simulations agree with excellent accuracy with the analytical models and theoretical interpretation presented here and suggest that nanoantennas may be effectively employed for biosensing at the single molecule level and optical communications.

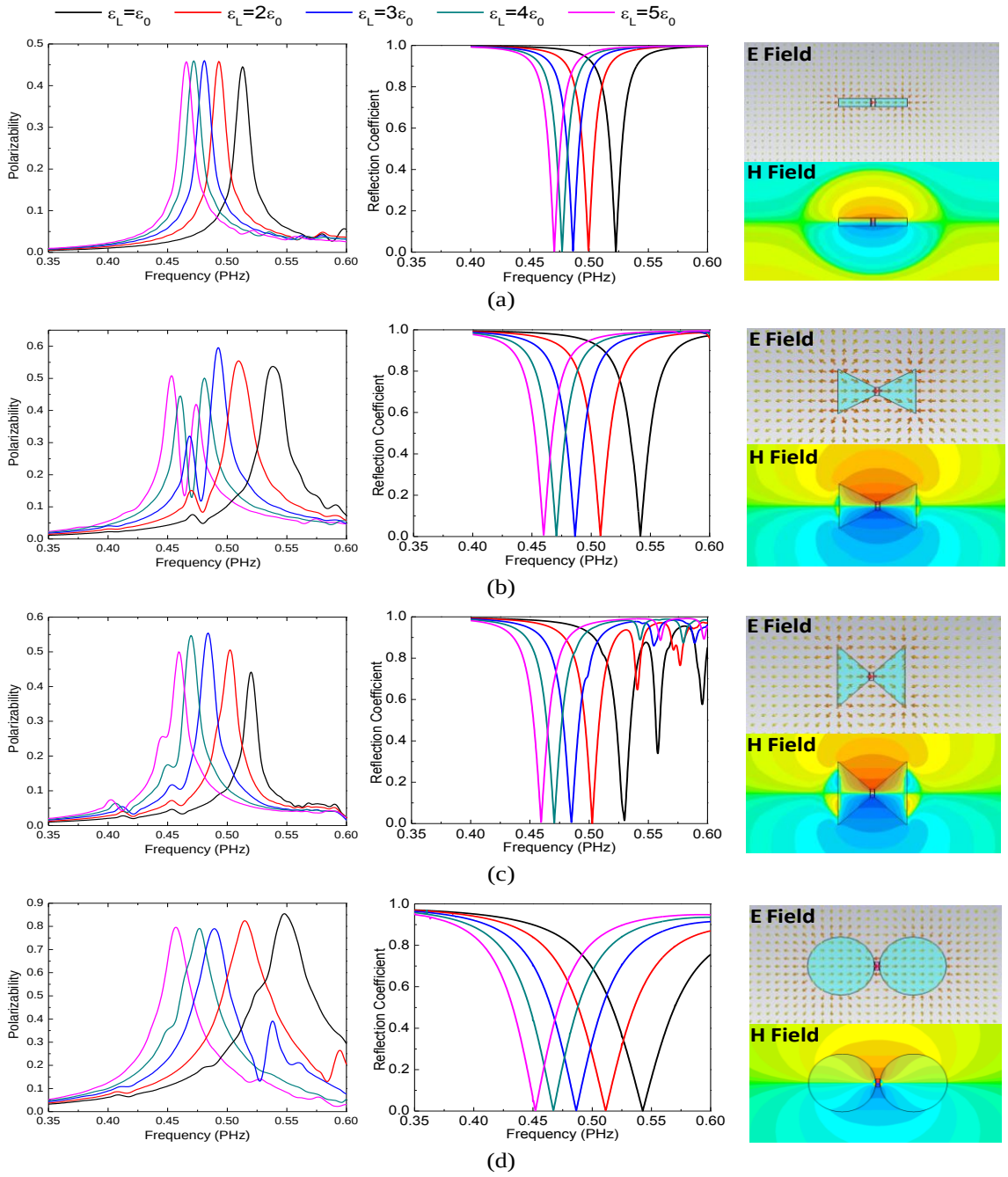

Figure 2.10: (Left) Normalized polarizability for gap size $50\times10\times20\ \text{nm}^3$ with: (a) $\alpha=0^{\circ}$, (b) $\alpha=60^{\circ}$, (c) $\alpha=90^{\circ}$, (d) $\alpha=180^{\circ}$; (center) Reflection coefficient when the nanoantennas are fed at the gap; (Right) corresponding field plots at resonance for load permittivity $\varepsilon_L=3\varepsilon_0$. (Reprinted with permission from JOSA B, Vol. 28, Issue 5, pp. 1266-1274 (2011). Copyright 2011 Journal of Optical Society of America)

2.6 REFERENCES

[1] P. Bharadwaj, B. Deutsch, and L. Novotny, "Optical antennas," Adv. Opt. Photon. 1, 438-483 (2009).

[2] P. Muhlschlegel, H. J. Eisler, O. J. F. Martin, B. Hecht, and D. W. Pohl, "Resonant optical antennas," Science 308, 1607-1609 (2005).

[3] P. J. Schuck, D. P. Fromm, A. Sundaramurthy, G. S. Kino, and W. E. Moerner, "Improving the mismatch between light and nanoscale objects with gold bowtie nanoantennas," Phys. Rev. Lett. 94, 017402 (2005).

[4] Z. Liu, A. Boltasseva, R. H. Pedersen, R. Bakker, A. V. Kildishev, V. P. Drachev, and V. M. Shalaev, "Plasmonic nanoantenna arrays for the visible," Metamaterials 2, 45-51 (2008).

[5] R. M. Bakker, A. Boltasseva, Z. Liu, R. H. Pedersen, S. Gresillon, A. V. Kildishev, V. P. Drachev, and V. M. Shalaev, "Near-field excitation of nanoantenna resonance," Opt. Express 15, 13682-13688 (2007).

[6] R. M. Bakker, H.-K. Yuan, Z. Liu, V. P. Drachev, A. V. Kildishev, and V. M. Shalaev "Enhanced localized fluorescence in plasmonic nanoantennae," Appl. Phys. Lett. 92, 043101 (2008).

[7] A. Bek, R. Jansen, M. Ringler, S. Mayilo, T. A. Klar, and J. Feldmann, "Fluorescence enhancement in hot spots of afm-designed gold nanoparticle sandwiches," Nano Lett. 8, 485-490 (2008).

[8] H. G. Frey, S. Witt, K. Felderer, and R. Guckenberger, "High-resolution imaging of single fluorescent molecules with the optical near-field of a metal tip," Phys. Rev. Lett. 93, 200801 (2004).

[9] P. Anger, P. Bharadwaj, and L. Novotny, "Enhancement and quenching of single-molecule fluorescence," Phys. Rev. Lett. 96, 113002 (2006).

[10] T. H. Taminiau, R. J. Moerland, F. B. Segerink, L. Kuipers, and N. F. van Hulst, "lambda/4 Resonance of an optical monopole antenna probed by single molecule fluorescence," Nano Lett. 7, 28-33 (2007).

[11] J. N. Farahani, D. W. Pohl, H. J. Eisler, and B. Hecht, "Single quantum dot coupled to a scanning optical antenna: A tunable superemitter," Phys. Rev. Lett. 95, 017402 (2005).

[12] A. Kinkhabwala, Z. F. Yu, S. H. Fan, Y. Avlasevich, K. Mullen, and W. E. Moerner, "Large single-molecule fluorescence enhancements produced by a bowtie nanoantenna," Nat. Photonics 3, 654-657 (2009).

[13] H. Mertens, J. S. Biteen, H. A. Atwater, and A. Polman, "Polarization-selective plasmon-enhanced silicon quantum-dot luminescence," Nano Lett. 6, 2622-2625 (2006).

[14] A. Sundaramurthy, P. J. Schuck, N. R. Conley, D. P. Fromm, G. S. Kino, and W. E. Moerner, "Toward nanometer-scale optical photolithography: Utilizing the near-field of bowtie optical nanoantennas," Nano Lett. 6, 355-360 (2006).

[15] K. Okamoto, I. Niki, A. Shvartser, Y. Narukawa, T. Mukai, and A. Scherer, "Surface-plasmon-enhanced light emitters based on InGaN quantum wells," Nat. Mater. 3, 601-605 (2004).

[16] S. A. Choulis, M. K. Mathai, and V. E. Choong, "Influence of metallic nanoparticles on the performance of organic electrophosphorescence devices," Appl. Phys. Lett. 88, 213503 (2006).

[17] J. J. Greffet, "Nanoantennas for light emission," Science 308, 1561-1563 (2005).

[18] A. F. Koenderink, "Plasmon nanoparticle array waveguides for single photon and single plasmon sources," Nano Lett. 9, 4228-4233 (2009).

[19] A. Alù, and N. Engheta, "Tuning the scattering response of optical nanoantennas with nanocircuit loads," Nat. Photonics 2, 307-310 (2008).

[20] A. Alù, and N. Engheta, "Input impedance, nanocircuit loading, and radiation tuning of optical nanoantennas," Phys. Rev. Lett. 101, 043901 (2008).

[21] A. Alù, and N. Engheta, "Hertzian plasmonic nanodimer as an efficient optical nanoantenna," Phys. Rev. B 78, 195111 (2008).

[22] A. Alù, and N. Engheta, "Wireless at the nanoscale: optical interconnects using matched nanoantennas," Phys. Rev. Lett. 104, 213902 (2010).

[23] L. Novotny, "Effective wavelength scaling for optical antennas," Phys. Rev. Lett. 98, 266802 (2007).

[24] M. F. Garcia-Parajo, "Optical antennas focus in on biology," Nat. Photonics 2, 201-203 (2008).

[25] F. Neubrech, A. Pucci, T. W. Cornelius, S. Karim, A. Garcia-Etxarri, and J. Aizpurua, "Resonant plasmonic and vibrational coupling in a tailored nanoantenna for infrared detection," Phys. Rev. Lett. 101, 157403 (2008).

[26] C. K. M. Fung, N. Xi, B. Shanker, K. W. C. Lai, and H. Chen, "Dipole and bowtie antenna for carbon nanotube (CNT) based infrared sensors", in *Proceedings of IEEE Conference on Nanotechnology Materials and Devices* (IEEE, 2009), pp. 87–90.

[27] N. Engheta, "Circuits with light at nanoscales: optical nanocircuits inspired by metamaterials, " Science 317, 1698-1702 (2007).

[28] N. Engheta, A. Salandrino, and A. Alù, "Circuit elements at optical frequencies: nanoinductors, nanocapacitors, and nanoresistors," Phys. Rev. Lett. 95, 095504 (2005).

[29] A. Alù, and N. Engheta, "On certain design criteria for nanoantennas in the visible," J. of Comput. Theor. Nanos. 6, 2009-2015 (2009).

[30] CST Microwave Studio™ 2010, CST of America, Inc.

[31] P.B. Johnson and R.W. Christy, "Optical constants of the noble metals," Phys. Rev. B 6, 4370-4379 (1972).

[32] A. Alù, A. Salandrino, and N. Engheta, "Parallel, series, and intermediate interconnections of optical nanocircuit elements. 2. Nanocircuit and physical interpretation," J. Opt. Soc. Am. B 24, 3014-3022 (2007).

[33] A. Alù, and N. Engheta, "Optical nanoswitch: an engineered plasmonic nanoparticle with extreme parameters and giant anisotropy," New J. Phys. 11, 013026 (2009).

[34] J. W. Becker, G. N. Reeke, J. L. Wang, B. A. Cunningham, and G. M. Edelman, "The covalent and three dimensional structure of Concanavalin A," J. Bio. Chem. 250, 1513-1524, (1975).

[35] L. S. Jung, C. T. Campbell, T. M. Chinowsky, M. N. Mar, and S. S. Yee, "Quantitative interpretation of the response of surface plasmon resonance sensors to adsorbed films ," Langmuir 14, 5636-5648 (1998).

[36] H. Sun, A. Chen, and L.R. Dalton, " Enhanced evanescent confinement in multiple-slot waveguides and its application in biochemical sensing," IEEE Photonics. J. 1, 48-57 (2009).

[37] J. N. Anker, W. P. Hall, O. Lyandres, N.C Shah, J. Zhao, and R.P. Van Duyne, "Biosensing with plasmonic nanosensors," Nat. Mater. 7, 442-453 (2008).

[38] A. Alù, and N. Engheta, "Polarizabilities and effective parameters for collections of spherical nano-particles formed by pairs of concentric double-negative (dng),

single-negative (SNG) and/or double-positive (DPS) metamaterial layers," J. Appl. Phys. 97, 094310 (2005).

Chapter 3: Experimental Validation of Individual Nanoantennas Loaded with Three-dimensional Optical Nanocircuits

In the previous chapter, we discussed how the shape and loading will affect the sensitivity, radiation efficiency and 3dB bandwidth of single element nanoantennas, where the sensitivity is the amount of frequency shift due to various designs of the nanoantenna geometries as a function of dielectric materials with different relative permittivities loaded at the nanoantenna gap. By using the nanocircuit concepts, we successfully tailored both the targeted resonance frequencies and the nanoantenna's sensitivity. In this chapter, we focus on experimental validation of single nanoantennas with various circuit loads by changing not only the materials loaded at the gap, but also the configurations of the loads. We experimentally demonstrate the first optical nanoscale circuits with fully three-dimensional lumped elements, which we use to tune and impedance-match a single optical dimer nanoantenna. We control the antenna resonance and impedance bandwidth using suitably designed loads with combinations of basic circuit elements: nanoscale capacitors, inductors and resistors. This study of single element nanoantennas will transfer in designing building blocks to compose two-dimensional densely packed nanoantenna arrays (metasurfaces) in the following chapters, and pave the way to the three-dimensional metasurfaces composites. In addition, our results will have a broad impact on extending conventional circuit concepts into the visible domain for applications in data storage, wireless optical links, and related venues.

3.1 INTRODUCTION

Antennas are essential devices in daily life, providing means of communication between the micro and macroworld. Impedance matching between an antenna and its feed network is fundamental to establishing an efficient wireless link. At radio

frequencies, matching is typically achieved by loading the antenna terminals with a circuit consisting of suitable combinations of resistors, capacitors and inductors. Extending this concept to the optical frequency domain [1]-[9] calls for optical analogues of these lumped circuit elements[10]-[13]. Such a set of circuit elements would provide a unique toolkit for designing all-optical wireless links [14], as well as for integration of nanophotonic devices in large optical nanocircuit boards.

Even though a significant amount of work has been devoted to the theory of optical nanocircuits (dubbed 'metatronics')[10],[12],[14]-[20] experimental verification has thus far been limited to a two-dimensional geometry [21], i.e., an ensemble of parallel rods, and to the mid-IR frequency range. While this geometry provides a proof-of-principle demonstration of the circuit theory, it is still far from the optical analog of individual, three-dimensional (3D) lumped circuit elements that could be freely combined into optical frequency nanocircuits of arbitrary complexity.

Here we present a significant step toward this direction by experimentally realizing and demonstrating 3D lumped nanocircuitry at visible wavelengths. To prove this concept, we utilize a simple optical antenna platform consisting of an individual gold dimer nanoantenna. This specific nanoantenna geometry is of particular interest due to its inherently large radiation efficiency and its strong tunability[11],[16],[18],[22]. Individual antennas are loaded with media of specific geometries and dielectric properties, enabling a full control of the loaded nanoantenna by an optical nanocircuit[10],[11],[14]-[16],[18],[23],[24]. We demonstrate both series and parallel combinations of nanocircuit elements (i.e., resistors, capacitors, and inductors) by appropriately loading specific arrangements of dielectric, semiconducting, and metallic nanoparticles in the antenna gap. Experimental measurements of the individually loaded nanoantennas confirm excellent tunability of the antenna impedance, resonance

wavelength, filtering, and scattering properties. The experimental results agree well with our analytical predictions based on optical circuit theory and full-wave simulations.

3.2 BACKGROUND OF BUILDING SINGLE ELEMENT NANOANTENNA AND NANOCIRCUIT LOAD

Our optical dimer nanoantenna consists of two closely spaced gold nanodiscs fabricated on a 100 nm SiO2 coated Si substrate (Figure 3.1a). The diameter and thickness of the gold discs are d = 116 nm and t = 50 nm, respectively. The gap between the two discs is g = 30 nm. By applying the Thévenin theorem to the gap terminals, we can define the effective optical impedance of the nanodimer as $Z_a = R_a - i X_a$. Figure 3.1b shows the antenna resistance R_a and reactance X_a as a function of wavelength. The curves are obtained using a semi-analytical retrieval method[18] by de-embedding the inherent capacitive effects that arise at the gap (see Methods). The same dimer nanoantenna is used throughout all the following examples. The optical impedance of the dimer nanoantenna is an intrinsic value, solely dependent on the antenna geometry and the material from which it is fabricated, not on the various materials to be loaded into the gap. By properly manipulating the nanoantenna load we may control and tune the antenna radiation properties over a broad range of wavelengths, in direct analogy to a radio-frequency antenna.

When the dimer nanoantenna is excited by light with the incident electric field parallel to the dimer axis (see Figure 3.1a), the antenna gap filters the incoming signal, operating as a parallel (shunt) combination of the antenna impedance Z_a and the load impedance at the gap. In order to provide a further insight, we examine the field distribution inside and around the dimer gap in the case of the unloaded nanoantenna (Figure 3.1b). For optical circuitry, the E-field component of the incident electromagnetic wave is the counterpart of the circuit voltage. The electric field changes sign when

crossing the dimer antenna terminals, ensuring continuity of the displacement currents across the gap and locally satisfying Kirchhoff's second law.

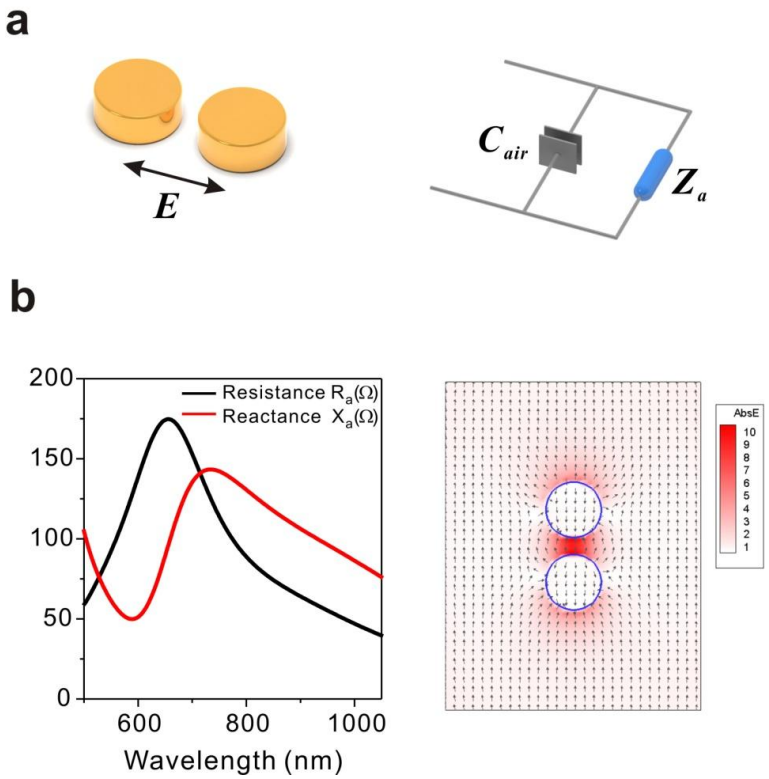

Figure 3.1: Geometry, nanocircuit model, and intrinsic impedance of a dimer nanoantenna. (a) Schematic of the unloaded dimer nanoantenna and its corresponding circuit model; (b) Intrinsic resistance and reactance of the dimer nanoantenna as a function of wavelength. The electric field distribution across the unloaded nanoantenna shows the parallel combination of the antenna and its capacitive gap. (Reprinted with permission from Nano Lett., 2013, 13 (1), pp 142–147. Copyright 2013 American Chemical Society)

The load in the gap therefore contributes an impedance, which is added in parallel to the intrinsic impedance of the dimer nanoantenna. The type of the complex impedance that the load may possess is determined by the dielectric properties of the material at optical frequencies. If the load is a dielectric with $\mathrm{Re}(\varepsilon) > 0$ at optical frequencies, it provides a capacitive impedance. If the load is a metal with $\mathrm{Re}(\varepsilon) < 0$ at optical

frequencies, it acts as an inductive impedance. The material loss of the load Im(ε) can be represented by a resistor element. From these basic elements [17],[19], complex nanocircuits can be constructed by combining suitably designed arrangements of different nanoparticle loads in the gap of the dimer nanoantenna.

3.3 EXPERIMENTAL VALIDATION OF SINGLE ELEMENT NANOANTENNA WITH NANOCIRCUIT LOAD

We start by first considering the simple case of a SiO_2 nanorod (Re(ε) > 0) loaded into the dimer antenna gap (see Figure 3.2a). The dimension of the rod is defined by its width, length, and thickness ($w \times g \times t$). Scanning electron microscope (SEM) images of the SiO_2 loaded antennas with different load widths are shown in Figure 3.2b (Fabrication details are provided in Methods). The optical response of the single nanoantennas with different loads is measured using dark-field microscopy and their scattering spectra are shown in Figure 3.2c. It is evident that the load can efficiently manipulate the dimer nanoantenna resonance, producing a successive red-shift in wavelength as the width of the SiO_2 rod increases. The experimental results agree well with the predictions obtained from full-wave simulations (Figure 3.2d).

Figure 3.2a shows the equivalent nanocircuit of the SiO_2 loaded nanoantenna. According to the nanocircuit paradigm [19], the SiO_2 load represents a capacitance, which can be simply described by the formula $C = \varepsilon wt / g$, where ε is the load permittivity. The total input impedance at the gap can then be calculated using

$$Z_{in} = \left(-i\omega C + \frac{1}{R_a - iX_a} \right)^{-1} . \qquad (3.1)$$

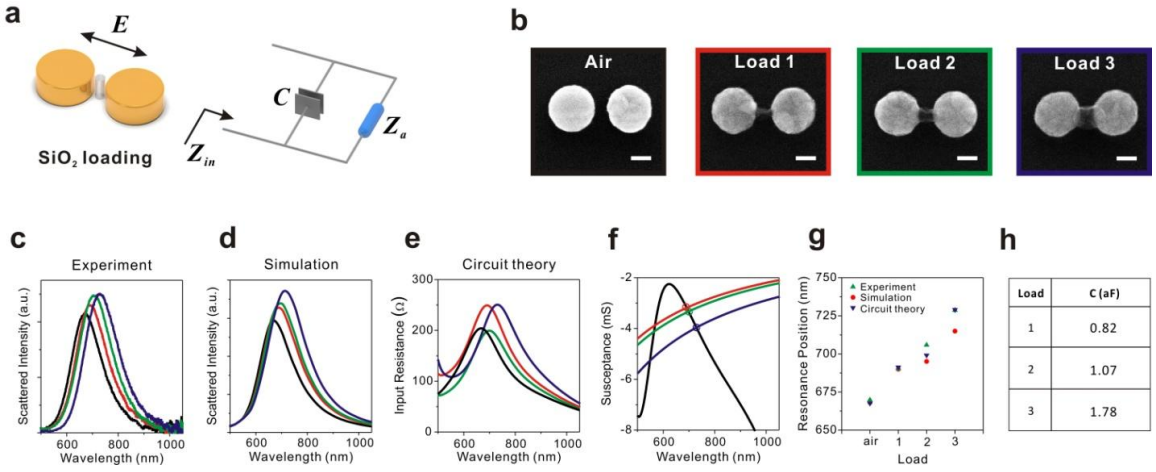

Figure 3.2: Dimer nanoantenna with capacitive loading. (a) Configuration of the SiO_2 loaded antenna and its corresponding circuit model; (b) SEM images of the SiO_2 loaded antennas. The widths of the SiO_2 rods are $w = 23\,nm$, $w = 30\,nm$, $w = 50\,nm$ for loads 1-3. The antenna gap dimension is $g = 30\,nm$, and the SiO_2 loads have the same thickness as the gold discs, $t = 50\,nm$. All scale bars in the SEM images are 50 nm. The frame colors of the SEM images in panel (b) correspond to the colors of the different loads shown in panels c to f: red (load1), green (load 2), and blue (load 3). (c) Experimental scattering spectra; (d) Corresponding simulated scattering spectra; (e) Calculated input resistances of the loaded nanoantennas as a function of wavelength; (f) Calculated intrinsic susceptance of the unloaded nanoantennas (black curve) and the susceptances of the loads as a function of wavelength. The intersections indicate the open-circuit resonances; (g) Comparison of the resonance wavelengths extracted from the experiment, numerical simulation, and the circuit model; h, Calculated capacitance values for loads 1-3. (Reprinted with permission from Nano Lett., 2013, 13 (1), pp 142–147. Copyright 2013 American Chemical Society)

Figure 3.2e shows the input resistances (the real part of Z_{in}) as a function of wavelength for different cases, as obtained using Eq. (3.1) with Z_a extracted from Figure 3.1b. A scattering maximum is observed in the spectrum at the open-circuit resonance of the loaded nanoantenna. At this peak wavelength, the antenna exhibits maximum scattering/absorption in its receiving operation and could be matched to a suitable feed line or a localized optical source in its transmitting operation. According to Eq. (1), this resonance arises when the intrinsic antenna susceptance $\mathrm{Im}\left[Z_a^{-1}\right]$ is

compensated by the capacitive susceptance of the load $-\omega C$. Figure 3.2f shows these two quantities as a function of wavelength. The circles in the figure are used to highlight the wavelength positions where the nanoantenna susceptance intersects with the susceptances of different loads, demonstrating the tunability of the open-circuit resonance through a capacitative load as predicted by our nanocircuit model. By inserting bigger SiO_2 nanorods into the nanoantenna gap and therefore larger capacitances, the antenna resonance shifts to longer wavelengths, consistent with the resonance shifts as shown in Figures. 3.2c-e.

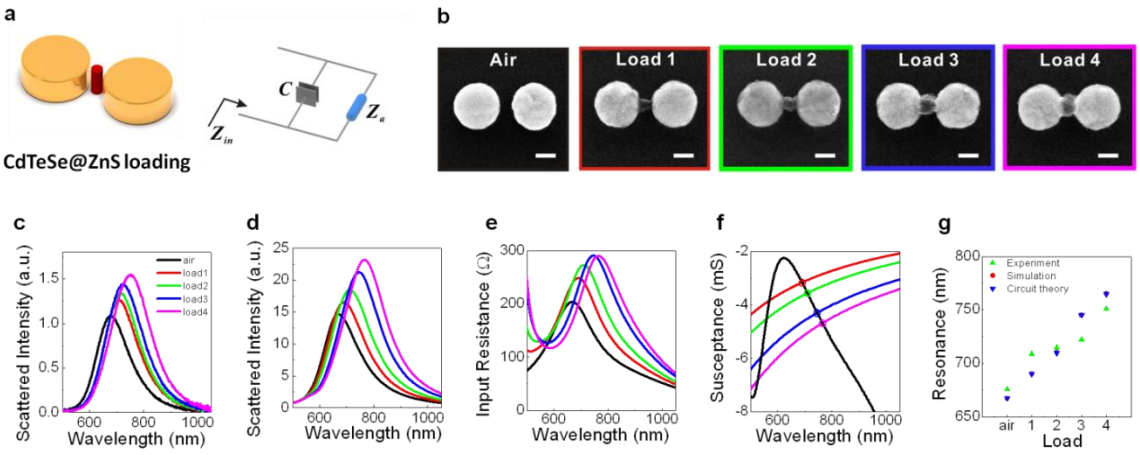

Figure 3.3: Dimer nanoantenna with quantum-dot loading. (a) Configuration of the CdTeSe@ZnS quantum dot loading and its corresponding circuit model. (b) SEM images for the loaded antennas. The radii of the quantum dot clusters are $a = 12\ nm$, $a = 14.5\ nm$, $a = 17.5\ nm$, $a = 22.5\ nm$ for loads 1-4. The remaining dimensions are consistent with the previous examples with other types of loads. All scale bars in the SEM images are 50 nm. (c) Experimental scattering spectra; (d) Corresponding simulated scattering spectra; (e) Calculated input resistances of the loaded dimer antennas; (f) Intrinsic susceptance of the unloaded nanoantenna (black curve) and the susceptances of the loads as a function of wavelength. The intersections indicate the open-circuit resonances; (g) Comparison of the resonance wavelengths extracted from the experiment, numerical simulation, and the circuit model. (Reprinted with permission from Nano Lett., 2013, 13 (1), pp 142–147. Copyright 2013 American Chemical Society)

Figure 3.2g compares the resonance positions extracted from the experiment, simulation, and circuit theory for each loaded dimer nanoantenna. These three sets of data match very well, confirming that capacitive loading can effectively manipulate the antenna resonance, as quantitatively predicted by Eq (3.1). The slight discrepancies between experiment and calculations are partially due to imperfections in fabrication due, for example, to small size and thickness variations through lithography and metal deposition. In addition, the circuit model assumes a uniform field distribution in the antenna gap, whereas the edges of the realistic structures may introduce fringing field effect. Still, excellent agreement is found, ensuring that the nanocircuit approach may lead to enormous simplifications in the design and operation of loaded nanoantennas. The table in Figure 3.2h displays the capacitance values for different loads. These values are extremely low, on the order of an attoFarad (10^{-18} F). This implies that the RC time constant of the nanostructure is extremely small. Larger capacitance values may be obtained by replacing the SiO_2 load medium with semiconductor materials of higher ε at optical frequencies, for example, CdTeSe@ZnS core/shell quantum dots and thus increasing the wavelength tunability (see Figure 3.3).

Significantly more advanced impedance tuning capabilities can be obtained by introducing combinations of variable nanocircuit elements. In the following, we demonstrate two examples of higher-order filters. When a gold nanoparticle with diameter *d* is loaded into the nanoantenna gap, the corresponding nanocircuit model is an LC series as shown in Figure 3.4a. This represents a second-order nanofilter. The gold nanoparticle acts as an optical frequency inductor and the two gaps between the gold nanoparticle and the discs of the nanoantenna behave as two capacitors. In our experiment, we sequentially increase the diameter of the gold nanoparticle until it is in conductive contact with both nanoantenna discs. The experimental and simulated

scattered spectra are shown in Figures 3.4c and 3.4d, respectively. Following the nanocircuit paradigm, the inductance of the loaded gold particle can be described by $L = -\left(\omega^2 \pi \varepsilon\, d/2\right)^{-1}$ and the gap capacitances are $C_1 = \varepsilon_0 \dfrac{wt}{g_1}$, $C_2 = \varepsilon_0 \dfrac{wt}{g_2}$, where g_1 and g_2 represent the residual gap sizes between the load and the dimer nanoantenna terminals. The total input impedance at the gap can then be calculated as

$$Z_{in} = \left(\left(-i\omega L + \frac{1}{-i\omega C_1} + \frac{1}{-i\omega C_2} \right)^{-1} + \frac{1}{R_a - iX_a} \right)^{-1}. \qquad (3.2)$$

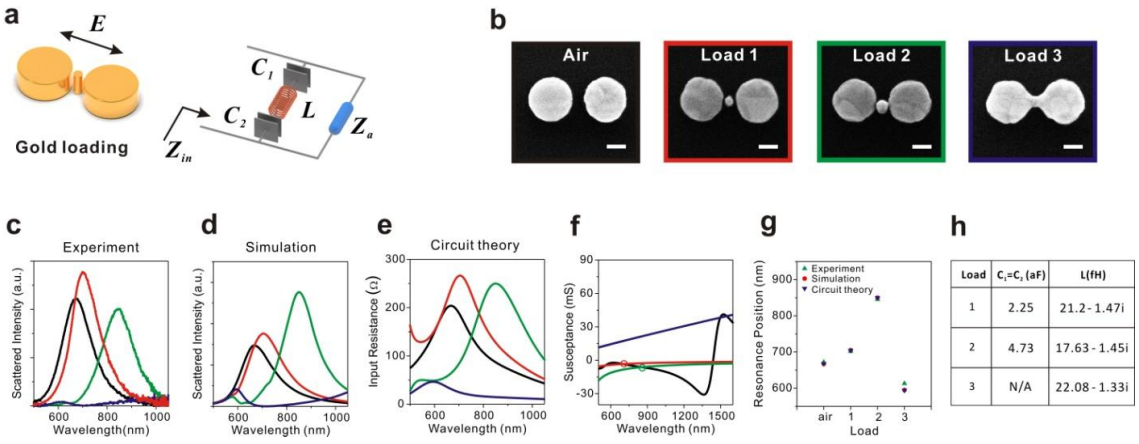

Figure 3.4: Dimer nanoantenna loaded by a second-order nanofilter. (a) Configuration of the gold loaded nanoantenna and its corresponding nanocircuit model; additional capacitances arise from the small gaps between the load and the two discs; (b) SEM images of the gold loaded antennas. The diameter of the gold load in the gap is $d = 20\ nm$ and $d = 28\ nm$ for loads 1 and 2, respectively, and the rod width of load 3 is $w = 20\ nm$. The remaining dimensions are consistent with the previous examples in Figure 3.2. All scale bars in the SEM images are 50 nm. (c) Experimental scattering spectra; (d) Corresponding simulated scattering spectra; (e) Calculated input resistances of the loaded nanoantennas as a function of wavelength; (f) Intrinsic susceptance of the unloaded nanoantenna (black curve) and the susceptances of the loads as a function of wavelength. The intersections indicate the open-circuit resonances; (g) Comparison of the resonance wavelengths extracted from the experiment, numerical simulation, and the circuit model; (h) Calculated nanocapacitive and nanoinductive values for loads 1-3. (Reprinted with permission from Nano Lett., 2013, 13 (1), pp 142–147. Copyright 2013 American Chemical Society)

Figures 3.4e and 3.4f show the input resistances and susceptances as a function of wavelength for different load cases, calculated using the nanocircuit theory with the same antenna impedance Z_a extracted from Figure 3.1b and Eq. (3.2). The capacitances and inductances of the nanocircuit elements are provided in Figure 3.4h. The capacitance values for this structure are also very small, in the attoFarad range, with the corresponding inductances in femtoHenries (10^{-15} H), ensuring high resonance frequencies in the visible regime ($\omega_r = (LC)^{-1/2}$). The presence of metal losses introduces a small imaginary part into the inductance, which corresponds to a small series resistance in the circuit model (not illustrated in Figure 3.4a).

In this second-order nanofilter scenario, the circuit load induces more complex frequency response, which allows for more flexible control of the antenna impedance dispersion and its wavelength-dependent scattering characteristics. In particular, we see in Figure 3.4f that the load susceptance can be tailored in a much broader fashion to support resonant dispersion and a range of both positive and negative reactive values, as a function of the relative weight of inductance and capacitance in the series nanocircuit. This enables impedance matching of the nanoantenna susceptance in different wavelength windows and provides a variety of bandwidths and scattering response as a function of the overall reactance of the load. This directly leads to a more variable dispersion of the resonance maximum of the open-circuit nanoantenna (Figure 3.4e), which translates into more tunable far-field scattering response of the loaded nanoantenna (Figures 3.4c and 3.4d). Figure 3.4g shows that the full-wave simulations and the experimental results follow the nanocircuit model predictions extremely well in terms of the open-circuit resonance. The resonance position and bandwidth can be broadly tuned by changing the filter response of the load. The corresponding field distribution (see Figure 3.5) is fully consistent with this model, showing the continuity of the displacement

currents flowing in the three reactive elements in the nanoantenna gap. The strong interaction of the electromagnetic field with the load and its specific polarization ensure the accuracy and applicability of our nanocircuit model across the entire wavelength range of interest.

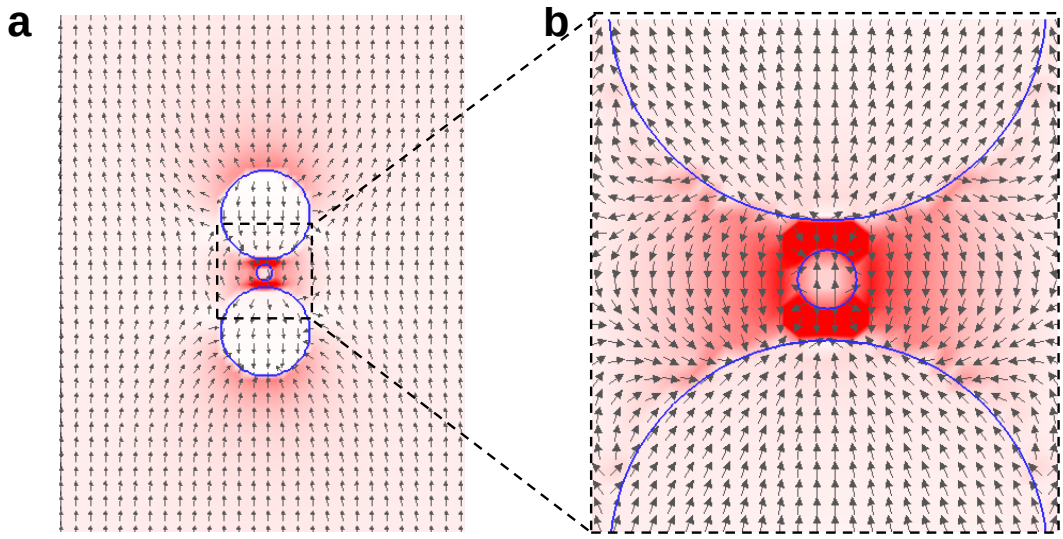

Figure 3.5: Field distribution of the nanoantenna with inductive loading. (a) Field distribution around the nanoantenna with the gold nanoload; (b) Enlarged view of the field across the gap. It shows that the electric field flips sign across the terminals of the nanoantenna and the boundary of the gold nanoload. This is consistent with the circuit model. (Reprinted with permission from Nano Lett., 2013, 13 (1), pp 142–147. Copyright 2013 American Chemical Society)

When the gold nanoparticle completely fills the nanoantenna gap (see load 3), the series capacitance is absent (see also Figure 3.4h). In this case, the RL load becomes purely inductive and the susceptance curve (blue curve in Figure 3.4d) barely intersects with the nanoantenna susceptance curve. The resonance is significantly blue-shifted and decreases in intensity. This effect is associated with a much smaller peak in the corresponding input resistance (Figure 3.4e). This may be particularly useful for

impedance matching the nanoantenna to lower impedance feeds, such as plasmonic wires, and shows the large degree of flexibility offered by a higher-order filter. When the metallic load is in direct contact with the nanoantenna arms, the electrons in the metal can move across the gap. Even in this extreme scenario, the nanocircuit theory holds a very good agreement with the experimental and full-wave simulation results (Figure 3.4g).

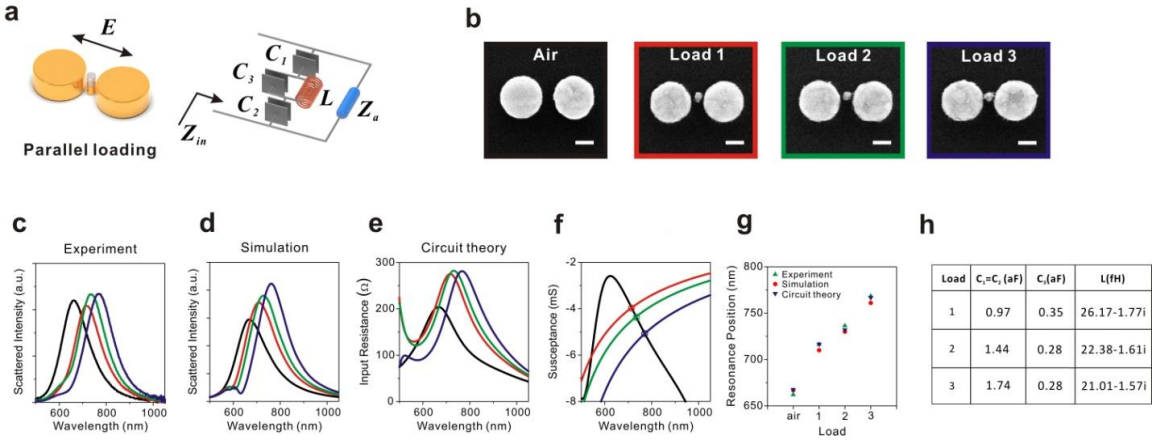

Figure 3.6: Dimer nanoantenna loaded by a third-order nanofilter. (a) Configuration of a gold partially loaded nanoantenna and its corresponding circuit model. C_1 and C_2 are obtained by leaving small gaps between the gold load and the two discs of the nanoantenna. C_3 is obtained by decreasing the thickness of the gold load; (b) SEM images of the gold partially loaded antennas. The thickness of the gold load in the gap is 30 nm and the diameters of the gold load are $d = 22\ nm$, $d = 24\ nm$, and $d = 26\ nm$ for loads 1-3. The remaining dimensions are consistent with the previous examples in Figure 3.2. All scale bars in the SEM images are 50 nm. (c) Experimental scattering spectra; (d) Corresponding simulated scattering spectra; (e) Calculated input resistances of the loaded nanoantennas as a function of wavelength; (f) Intrinsic susceptance of the unloaded nanoantenna (black curve) and the susceptances of the loads as a function of wavelength. The intersections indicate the open-circuit resonances; (g) Comparison of the resonance wavelengths extracted from the experiment, numerical simulation, and the circuit model; h, Calculated nanocapacitive and nanoinductive values for loads 1-3. (Reprinted with permission from Nano Lett., 2013, 13 (1), pp 142–147. Copyright 2013 American Chemical Society)

As a final example of the flexibility and potential of this approach, we demonstrate a third-order nanofilter. This is realized by using a thinner gold particle load than the antenna itself in the gap, which is equivalent to loading the nanoantenna with a capacitor (C_3) and an inductor (L), simultaneously leaving suitable gaps to the nanoantenna terminals, which behave as two additional capacitors (C_1 and C_2) as shown in Figure 3.6a. In this case, the loading in the antenna gap corresponds to an LC parallel circuit in series with two additional capacitances. The additional parallel capacitance C_3 leads to sharper response in the impedance dispersion as well as sharper scattering features measured in the far field (Figure 3.6c). The impedance values of this third-order nanofilter are shown in Figure 3.6h for different cases. Our experimental and simulated results agree very well, again supporting our nanocircuit model (Figure 3.6). In this scenario, the four reactances can cooperatively tailor the open-circuit resonance peak and impedance dispersion of the dimer nanoantenna. Figure 3.7 shows the field distributions of the loaded antenna at two different cutting planes. Continuity of the displacement current is also confirmed in this more complex nanocircuit, which ensures the validity of our circuit model.

Our work in this chapter provides an experimental demonstration of the nanocircuit paradigm to control and manipulate the optical response of nanoantennas. We have experimentally realized various topologies of first-order, second-order, and third-order 3D nanofilters to tune and match an individual optical nanoantenna. To our knowledge, this represents the first realization and verification of 3D optical frequency nanocircuits. These results present a blueprint for controlling and tuning optical frequency nanophotonic devices using nanocircuits, analogous to turning the frequency-tuning knob of a radio. This is remarkably different from antenna tuning through other strategies [25]. Our concept introduces optical nanoscale circuits based on fully three-

dimensional lumped elements, used to tune at will an optical nanodimer. We believe that our work paves the way to the eventual development of integrated optical frequency circuit boards and optical wireless links that bridge on-chip nanoscale optical signals to the far field.

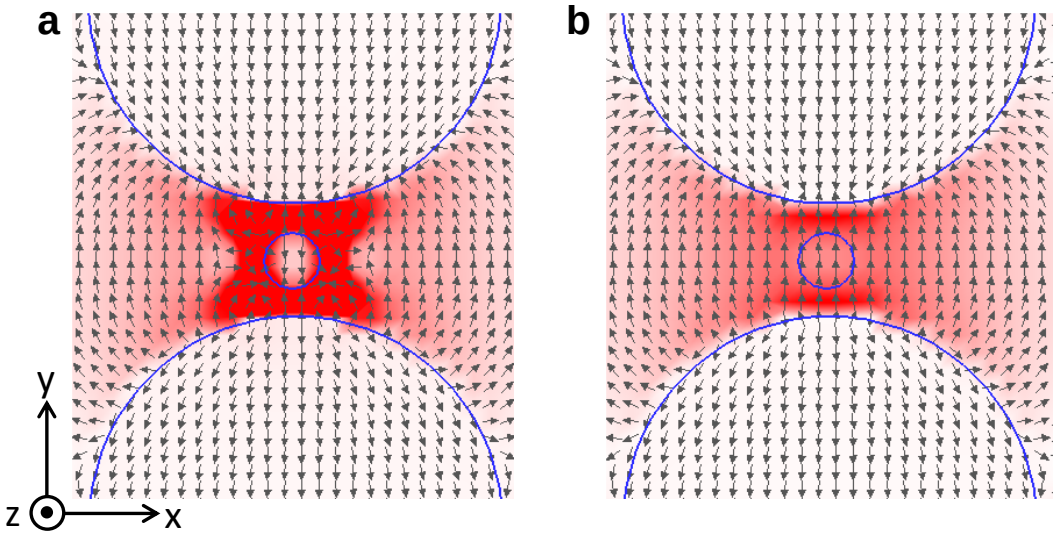

Figure 3.7: Field distribution of the nanoantenna with parallel loading. (a) Enlarged view of the field distribution surrounding the nanoantenna gap within the inductive loading region ($z = 12.5\,nm$); (b) Enlarged view of the field distribution surrounding the nanoantenna gap within the capacitively loading region ($z = 37.5\,nm$). (Reprinted with permission from Nano Lett., 2013, 13 (1), pp 142–147. Copyright 2013 American Chemical Society)

3.3.1 Nanofabrication details

The antenna structures and alignment markers are first defined in poly(methyl methacrylate) resist using electron-beam lithography on a 100 nm SiO2 coated Si substrate. The substrate is then covered with 1 nm titanium adhesion film and 50 nm gold film using electron-beam evaporation followed by a lift-off procedure. Next, the substrate is coated once more with poly(methyl methacrylate) resist. Computer-controlled

alignment at the sub-10 nm level using the gold alignment markers is applied to ensure the accurate positioning of the nanoload pattern in the antenna gap. Subsequently, the nanoload material is obtained by covering the substrate first with 1 nm titanium adhesion film and then the target material using electron-beam evaporation followed by a lift-off procedure.

3.3.2 Optical measurement of single element nanoantenna

The scattering spectra of the single nanoantennas with different loads are collected using dark-field microscopy. The microscope used is a Zeiss Axiovert 200 MAT, the CCD is a Princeton Instruments Pixis 400 BR, and the spectrograph is an Acton 2156i imaging spectrograph. The objective used is a long working distance objective with numerical aperture of 0.55.

3.3.3 Numerical simulation of the loaded nanoantennas

The full-wave numerical simulations are obtained using a commercial implementation of the Finite Element Method (COMSOL Multiphysics). A plane wave with electric field linearly polarized along the antenna axis is employed to analyze the far-field scattering properties in the loaded and unloaded scenarios. The permittivity of SiO2 is taken as 2.09, and the empirical dielectric function of bulk gold is used [26].

3.3.4 Calculation of input impedance

The intrinsic impedance of the dimer nanoantenna was calculated using a retrieval method based on full-wave numerical simulations [27]. It was sufficient to conduct one numerical simulation of the nanoantenna driven by a discrete current source to retrieve the intrinsic resistance R_a and reactance X_a as shown in Figure 3.1b and use them for the loaded antenna cases. The retrieval algorithm is based on equations introduced in Chapter 2 [18], with

$$R_a = \frac{r_0}{1 + C_{air}\omega\left(2x_0 + C_{air}\left(r_0^2 + x_0^2\right)\omega\right)}, \tag{3.3}$$

and

$$X_a = \frac{x_0 + C_{air}\left(r_0^2 + x_0^2\right)\omega}{1 + C_{air}\omega\left(2x_0 + C_{air}\left(r_0^2 + x_0^2\right)\omega\right)}. \tag{3.4}$$

r_0 and x_0 are the input resistance and reactance of the dimer antenna, which is excited by a discrete current source at the empty gap. $C_{air} = \varepsilon_0 S / g$ is the capacitance at the empty gap to be de-embedded, S is the effective area of the capacitor at the gap, and g is the gap dimension. The fringing fields close to the edge of the capacitor are negligible here because the diameter of the loaded particle is larger than the effective width of the gap.

3.4 REFERENCES

[1] Adato, R.; Yanik, A. A.; Altug, H. Nano Lett., 11, (12), 5219-5226, (2011).

[2] Agio, M. and Alù, A. (eds.) Optical Antennas. Cambridge University Press 2012.

[3] Curto, A. G.; Volpe, G.; Taminiau, T. H.; Kreuzer, M. P.; Quidant, R.; van Hulst, N. F. Science, 329, (5994), 930-933, (2010).

[4] Farahani, J. N.; Pohl, D. W.; Eisler, H. J.; Hecht, B. Phys. Rev. Lett., 95, (1), 017402, (2005).

[5] Greffet, J. J. Science, 308, (5728), 1561-1563, (2005).

[6] Muhlschlegel, P.; Eisler, H. J.; Martin, O. J. F.; Hecht, B.; Pohl, D. W. Science, 308, (5728), 1607-1609, (2005).

[7] Novotny, L. Phys. Rev. Lett., 98, (26), 266802, (2007).

[8] Novotny, L.; van Hulst, N. Nat. Photonics, 5, (2), 83-90, (2011).

[9] Taminiau, T. H.; Stefani, F. D.; Segerink, F. B.; Van Hulst, N. F. Nat. Photonics, 2, (4), 234-237, (2008).

[10] Alù, A.; Engheta, N. Phys. Rev. Lett., 101, (4), 043901, (2008).

[11] Berthelot, J.; Bouhelier, A.; Huang, C. J.; Margueritat, J.; Colas-des-Francs, G.; Finot, E.; Weeber, J. C.; Dereux, A.; Kostcheev, S.; El Ahrach, H. I.; Baudrion, A. L.; Plain, J.; Bachelot, R.; Royer, P.; Wiederrecht, G. P. Nano Lett., 9, (11), 3914-3921, (2009).

[12] Greffet, J. J.; Laroche, M.; Marquier, F. Phys. Rev. Lett., 105, (11), 117701, (2010).

[13] Huang, J. S.; Feichtner, T.; Biagioni, P.; Hecht, B. Nano Lett., 9, (5), 1897-1902, (2009).

[14] Alù, A.; Engheta, N. Phys. Rev. Lett. 104, (21), 213902, (2010).

[15] Alù, A.; Engheta, N. Nat. Photonics, 2, (5), 307-310, (2008).

[16] Alù, A.; Engheta, N. Phys. Rev. B, 78, (19), 195111, (2008).

[17] Engheta, N. Science, 317, (5845), 1698-1702, (2007).

[18] Zhao, Y.; Engheta, N.; Alù, A. J. Opt. Soc. Am. B: Opt. Phys., 28, (5), 1266-1274, (2011).

[19] Engheta, N.; Salandrino, A.; Alù, A. Phys. Rev. Lett., 95, (9), 095504, (2005).

[20] Ozbay, E. Science, 311, (5758), 189-193, (2006).

[21] Sun, Y.; Edwards, B.; Alù, A.; Engheta, N. Nat. Mater., 11, (3), 208-212, (2012).

[22] Huang, F. M.; Baumberg, J. J. Nano Lett., 10, (5), 1787-1792, (2010).

[23] Large, N.; Abb, M.; Aizpurua, J.; Muskens, O. L. Nano Lett., 10, (5), 1741-1746, (2010).

[24] Schnell, M.; Garcia-Etxarri, A.; Huber, A. J.; Crozier, K.; Aizpurua, J.; Hillenbrand, R. Nat. Photonics, 3, (5), 287-291, (2009).

[25] Atay, T.; Song, J. H.; Nurmikko, A. V. Nano Lett., 4, (9), 1627-1631, (2004).

[26] Johnson, P. B.;Christy, R. W. Phys. Rev. B, 6,(12), 4370-4379, (1972).

[27] CST Studio Suite 2011. Available at http://www.cst.com

Chapter 4: Theoretical Analysis of the Chiral Effect of Mestasurfaces

So far we have walked through the theoretical designs and optimization of single element nanoantennas, and experimentally demonstrated the feasibility of realizing these building blocks loaded with different nanocircuit elements, providing large at optical frequencies. In this chapter, we will explain theoretically how chiral effect could arise by specific designing thin sheet of two dimensional nanoantenna arrays, also called metasurfaces. The chiral effect is one of the means that could lead to broadband circular polarized filtering effect, which could function similarly as the filtering effect in the vision system of the biological species we introduced initially, such as the mantis shrimps.

In this context, we discuss in details in this chapter the theoretical basis and numerically model the physical mechanisms behind extrinsic chiral effects induced over ultrathin plasmonic metasurfaces and in optical metamaterials characterized by controlled arrangements of stacked metasurfaces. We explain these effects using analytical models, supported and validated by full-wave numerical simulations. We also provide physical insights into the anomalous optical effects offered by these nanodevices and we envision potential optical applications of these concepts.

4.1 INTRODUCTION

The nature of light propagation has fascinated mankind for centuries and has been studied since ancient times by Greek philosophers, who were the first to discover that light travels along straight lines in homogeneous media, can be focused by curved glasses, can be reflected by smooth surfaces and is refracted when crossing interfaces between media with different density. Mankind has been using these properties to transmit signals, detect and exchange information for centuries. The physical principles

behind these phenomena were established well before 1900 and are based on structures and devices many wavelengths large. However, due to recent advances in science and technology, scientists and researchers have become more interested in controlling the interaction of light with matter in nanostructures of size comparable with the wavelength of operation. These possibilities can largely overcome the conventional limitations of light manipulation and their applications, mostly associated with the diffraction limit. It has been found, in particular, that nanoparticles and their collections may achieve exotic phenomena that are not available in conventional optics. The whole research area of metamaterials, currently one of the most popular in optics, has emerged from these concepts [1]-[21]. In the following, we review our recent efforts in using metasurfaces and their combinations to realize unique chiral effects at the nanoscale, and in modeling these effects using analytical techniques that can provide physical insights into these anomalous optical phenomena.

It is interesting that one of the first forms of exotic artificial materials, realized over a century before the term ‘metamaterials’ was even coined, was produced with the goal of largely increasing optical activity and chirality in natural materials by J. C. Bose in 1898 [22],[23]. In these early experiments, twisted artificial molecules were used to introduce strong chiral effects that were essential to tailor and control the polarization of light and create circular polarization. Today even more than at those times, control and detection of the polarization state of light is fundamental in several optical and photonic applications, and it is one of the relevant functionalities that distinguish several biological species [24]-[27] from the human vision system, which cannot detect polarization information. Although linear polarizers are quite easily realized, and they may work over a broad range of frequencies, detection of circular polarization is more challenging, since it is inherently based on phase detection, and it may be usually performed only over a

limited range of frequencies using quarter-wave plate technology. However, biological species can detect circular polarization information over much broader bandwidths, and they are able to use this information for orientation, signaling and defense. Therefore, it would be very relevant to develop analogous functionalities in a man-made photonic system operating at the nanoscale.

As we will discuss in the following, the exotic features of plasmonic metasurfaces in the visible domain may provide the necessary tools to induce compact resonances and anomalous optical response for strong chiral effects. In the following sections, we first put forward a general theoretical model for ultrathin planar plasmonic metasurfaces, with particular attention to their chiral effects, using an averaged transmission-line shunt admittance tensor based on the generalized dipolar polarizability of the inclusions forming the array. In our model, we fully take into account the dynamic interaction within the array and the cross-polarization coupling. We validate the accuracy of our approach and its limitations by comparing the homogenized metasurface model with full-wave numerical simulations based on finite-integration techniques (CST Microwave StudioTM 2011), in order to outline the conditions under which the averaged optical surface impedance may accurately describe the complex wave interaction of planar plasmonic metasurfaces. Then, we apply this analytical model to explore various technological approaches to achieve strong chiral effects using metasurfaces, such as the realization of lithographic periodic arrays of nanoparticles and stacks of plasmonic metasurfaces to form twisted metamaterials, a concept that we have recently introduced to provide strong, broadband optical activity based on a lattice effect [28].

4.2 WAVE INTERACTION WITH PLANAR METASURFACES: THEORETICAL BASIS

One of the major advantages of metasurfaces is the relaxation of complicated fabrication processes required in three-dimensional metamaterials, which is especially challenging at optical frequencies. Recent works based on a three-dimensional lithographic method, direct laser writing (DLW), have demonstrated the realization of three-dimensional metamaterials that exhibit strong, broadband chirality in the near-IR to mid-IR regime [29],[30]. DLW is an emerging microfabrication technique based on two-photon absorption to initiate polymerization; the limitation of this method resides in the ultimate feature dimensions that may be achieved in the fabricated structure, which is ultimately dominated by the diffraction limit [31]-[33]. This is due to the fact that light sources commonly utilized in this fabrication method are Ti: Sapphire lasers with an emitting wavelength centered at 800nm; therefore, the voxel size is severely limited by this length scale. So far the smallest feature achieved with this method is in the micro-meter range. Planar lithographic methods, such as electron beam lithography, on the contrary, utilize electron beams, implying that, theoretically, the minimum spot size can be as small as a few nanometers, which can provide more possibilities for metamaterial applications in the visible range, including optical activity. Chirality has been demonstrated in either planar [34]-[38] or three-dimensional metamaterials [28],[39] using this fabrication technique. Planar metasurfaces generally exhibit much weaker chiral effects compared with three-dimensional geometries, because an infinitesimally thin surface is inherently achiral, and excitation at oblique incidence or nonreciprocal responses are required to distinguish between left-handed (LCP) and right-handed circular polarizations (RCP).

In this chapter, we theoretically discuss how individual and stacked planar metasurfaces may provide strong chiral effects and effectively respond as a bulk three-

dimensional chiral metamaterial. We first consider a single, optically thin metasurface located in the $z=0$ plane, formed by arbitrarily shaped plasmonic nanoparticles embedded in a rectangular lattice with periods d_x and d_y. We assume here and in the following that the lattice constants are much smaller than the wavelength of operation so that only the zero-th diffraction order can propagate away from the metasurface plane, and that the inclusions are not too densely packed so that the optical wave interaction can be modeled using the dipolar approximation with good accuracy. We further assume that the inclusions are sufficiently thin in the direction normal to the array to ensure that only an optical displacement current tangential to the surface may be induced.

These assumptions ensure that, when excited by an external plane wave with arbitrary polarization and incidence angle θ, the inclusions are well described by an electric dipole moment parallel to the surface and a magnetic dipole moment normal to it. In the planar array, the local fields impinging on each inclusion are given by the superposition of the impinging fields and the radiation from other dipoles, due to the coupling with the inclusions in the array. Therefore, the metasurface response may be compactly described through a generalized array polarizability tensor $\underline{\underline{\boldsymbol{\alpha}}}_s$ that relates the induced dipole moments at the origin $\mathbf{p}_{00}$, $m_{00}\hat{\mathbf{z}}$ to the impinging fields $\mathbf{E}_{inc}$ (electric) and $\mathbf{H}_{inc}$ (magnetic), including the full dynamic coupling among the inclusions [40],[41]:

$$\begin{pmatrix} \mathbf{p}_{00}/\varepsilon_0 \\ \eta_0 m_{00}/\mu_0 \end{pmatrix} = \left(\begin{pmatrix} \underline{\boldsymbol{\alpha}}_{ee} & \boldsymbol{\alpha}_{em} \\ \boldsymbol{\alpha}_{me} & \alpha_{mm} \end{pmatrix}^{-1} - \begin{pmatrix} \underline{\mathbf{C}}_{tt} & \mathbf{C}_{tz} \\ \mathbf{C}_{zt} & C_{zz} \end{pmatrix} \right)^{-1} \cdot \begin{pmatrix} \mathbf{E}_{inc} \times \hat{\mathbf{z}} \\ \eta_0 \mathbf{H}_{inc} \cdot \hat{\mathbf{z}} \end{pmatrix} = \underline{\underline{\boldsymbol{\alpha}}}_s \cdot \begin{pmatrix} \mathbf{E}_{inc} \times \hat{\mathbf{z}} \\ \eta_0 \mathbf{H}_{inc} \cdot \hat{\mathbf{z}} \end{pmatrix}. \quad (4.1)$$

In this formula, $\underline{\underline{\boldsymbol{\alpha}}}_{ee}$ is the transverse electric polarizability tensor (2×2), α_{mm} is the normal magnetic polarizability coefficient and $\boldsymbol{\alpha}_{em}$, $\boldsymbol{\alpha}_{me}$ are the magnetoelectric polarizability vectors, which take into account the cross-coupling between transverse electric and normal magnetic effects due to artificial magnetism and polarization effects.

In addition, the $\mathbf{C}$ elements are the Green's dyadic coefficients taking into account the array coupling [40], $\hat{\mathbf{z}}$ is the unit normal vector to the array, ε_0, μ_0 and $\eta_0 = \sqrt{\mu_0 / \varepsilon_0}$ are the free-space permittivity, permeability and characteristic impedance, respectively. The reciprocity of the metasurface imposes the Onsager constraints [42],[43] on these elements, which may be combined with the reciprocal properties of the coupling dyads:

$$\underline{\boldsymbol{\alpha}}_{ee} = \underline{\boldsymbol{\alpha}}_{ee}^{T},\ \boldsymbol{\alpha}_{me} = -\boldsymbol{\alpha}_{em}^{T},\ \underline{\mathbf{C}}_{tt} = \underline{\mathbf{C}}_{tt}^{T},\ \mathbf{C}_{zt} = -\mathbf{C}_{tz}^{T}, \tag{4.2}$$

where the superscript T indicates the transpose operation, to ensure that the generalized polarizability tensor has also a reciprocal form:

$$\underline{\underline{\boldsymbol{\alpha}}}_{s} = \begin{pmatrix} \alpha_{xx}^{ee} & \alpha_{xy}^{ee} & \alpha_{xz}^{em} \\ \alpha_{yx}^{ee} & \alpha_{yy}^{ee} & \alpha_{yz}^{em} \\ \alpha_{zx}^{me} & \alpha_{zy}^{me} & \alpha_{zz}^{mm} \end{pmatrix} = \begin{pmatrix} \underline{\boldsymbol{\alpha}}_{s}^{ee} & \boldsymbol{\alpha}_{s}^{em} \\ \left(-\boldsymbol{\alpha}_{s}^{em}\right)^{T} & \alpha_{s}^{mm} \end{pmatrix}. \tag{4.3}$$

In general, the elements of the generalized polarizability tensor are dependent on the incidence angle, as a symptom of spatial dispersion in the array, due to the influence of the coupling dyadics. For smaller periods, however, these effects are usually small. The induced dipole moments on all the other inclusions are related to $\mathbf{p}_{00}$, $\mathbf{m}_{00}$ through a simple phase shift associated to the momentum of the impinging excitation, which is conserved.

It follows that, within the dipolar limit, the tensor $\underline{\underline{\boldsymbol{\alpha}}}_{s}$ compactly describes the metasurface interaction with an arbitrary impinging plane wave, which effectively induces an averaged electric surface current density tangential to the plane

$$\mathbf{K}_{e} = \frac{j\omega \mathbf{p}_{00}}{d_x d_y}\ \left[A/m\right], \tag{4.4}$$

and a normal magnetic surface current density

$$\mathbf{K}_m = \frac{j\omega m_{00}}{d_x d_y}\hat{\mathbf{z}}\,[V/m]. \tag{4.5}$$

We have indicated the units of $\mathbf{K}_e$ and $\mathbf{K}_m$ in these formulas for clarity.

4.2.1 Transverse-Magnetic (TM) excitation

For TM polarized excitation, without losing in generality

$$\mathbf{H}_{\mathbf{inc}} = \frac{E_0}{\eta_0} e^{-j\sqrt{k_0{}^2 - k_x{}^2}z} e^{-jk_x x}\hat{\mathbf{y}}, \tag{4.6}$$

where k_0 is the wave number in free-space. The associated incident electric field is

$$\mathbf{E}_{\mathbf{inc}} = e^{-j\sqrt{k_0{}^2 - k_x{}^2}z} e^{-jk_x x} E_0 \left(\frac{\sqrt{k_0{}^2 - k_x{}^2}}{k_0}\mathbf{x} - \frac{k_x}{k_0}\hat{\mathbf{z}} \right). \tag{4.7}$$

The induced averaged surface currents radiate plane waves described by the vector potentials

$$\mathbf{A} = \frac{-j\mu_0}{2\sqrt{k_0{}^2 - k_x{}^2}} \mathrm{e}^{-j\sqrt{k_0{}^2 - k_x{}^2}z}\mathbf{K}_e, \tag{4.8}$$

and

$$\mathbf{F} = \frac{-j\epsilon_0}{2\sqrt{k_0{}^2 - k_x{}^2}} \mathrm{e}^{-j\sqrt{k_0{}^2 - k_x{}^2}z}\mathbf{K}_m. \tag{4.9}$$

From these expressions, it is easy to calculate the transmitted and reflected fields. First, by combining all the previous equations, we find the total transmitted magnetic fields associated with the magnetic potential $\mathbf{A}$:

$$\mathbf{H_t} = \mathbf{H_{inc}} + \frac{jE_0 e^{-j\left(k_x x + \sqrt{k_0^2 - k_x^2}z\right)}}{2d_x d_y \eta_0}\left(\alpha_{yx}^{ee}\sqrt{k_0^2 - k_x^2}\hat{\mathbf{x}} - \alpha_{xx}^{ee}\sqrt{k_0^2 - k_x^2}\hat{\mathbf{y}} - \alpha_{yx}^{ee}k_x\hat{\mathbf{z}}\right), \quad (4.10)$$

and the corresponding reflected magnetic field

$$\mathbf{H_r} = \frac{jE_0 e^{-j\left(k_x x - \sqrt{k_0^2 - k_x^2}z\right)}}{2d_x d_y \eta_0}\left(-\alpha_{yx}^{ee}\sqrt{k_0^2 - k_x^2}\hat{\mathbf{x}} + \alpha_{xx}^{ee}\sqrt{k_0^2 - k_x^2}\hat{\mathbf{y}} - \alpha_{yx}^{ee}k_x\hat{\mathbf{z}}\right). \quad (4.11)$$

Therefore, the transmission and reflection coefficients for electric fields due to the induced electric current density are compactly given by:

$$\begin{aligned} T_{mm}^{e} &= 1 - \frac{jk_0\cos\theta}{2d_x d_y}\alpha_{xx}^{ee} \\ T_{em}^{e} &= -\frac{jk_0}{2d_x d_y}\alpha_{yx}^{ee} \\ R_{mm}^{e} &= -\frac{jk_0\cos\theta}{2d_x d_y}\alpha_{xx}^{ee} \\ R_{em}^{e} &= -\frac{jk_0}{2d_x d_y}\alpha_{yx}^{ee} \end{aligned}, \quad (4.12)$$

where $\cos\theta = \sqrt{k_0^2 - k_x^2}/k_0$. $T_{mm}\left(R_{mm}\right)$ and $T_{em}\left(R_{em}\right)$ are the transmission (reflection) coefficients for TM incident polarization radiating TM and TE polarizations, respectively.

The electric potential $\mathbf{F}$ similarly generates a transmitted electric field

$$\mathbf{E_t} = -\frac{jE_0 e^{-j\left(k_x x + \sqrt{k_0^2 - k_x^2}z\right)}}{2d_x d_y}\alpha_{zx}^{me}k_x\hat{\mathbf{y}}, \quad (4.13)$$

and a reflected field

$$\mathbf{E_r} = -\frac{jE_0 e^{-j\left(k_x x - \sqrt{k_0^2 - k_x^2}z\right)}}{2d_x d_y}\alpha_{zx}^{me}k_x\hat{\mathbf{y}}. \quad (4.14)$$

Therefore the transmission and reflection coefficients due to the magnetic current density for TM excitation are:

$$\begin{aligned} T_{mm}^{m} &= 0 \\ T_{em}^{m} &= -\frac{jk_0 sin\theta}{2d_x d_y}\alpha_{zx}^{me} \\ R_{mm}^{m} &= 0 \\ R_{em}^{m} &= -\frac{jk_0 sin\theta}{2d_x d_y}\alpha_{zx}^{me} \end{aligned} \quad . \tag{4.15}$$

Summing Eq. (4.12) and Eq. (4.15) we find the total transmission and reflection coefficients for TM excitation:

$$\begin{aligned} T_{mm} &= T_{mm}^{e} + T_{mm}^{m} = 1 - \frac{jk_0 \cos\theta}{2d_x d_y}\alpha_{xx}^{ee} \\ T_{em} &= T_{em}^{e} + T_{em}^{m} = -\frac{jk_0}{2d_x d_y}\left(\alpha_{yx}^{ee} + sin\theta\alpha_{zx}^{me}\right) \\ R_{mm} &= R_{mm}^{e} + R_{mm}^{m} = -\frac{jk_0 \cos\theta}{2d_x d_y}\alpha_{xx}^{ee} \\ R_{em} &= R_{em}^{e} + R_{em}^{m} = -\frac{jk_0}{2d_x d_y}\left(\alpha_{yx}^{ee} + sin\theta\alpha_{zx}^{me}\right) \end{aligned} \quad . \tag{4.16}$$

The above equations compactly describe the interaction of the metasurface with arbitrary TM impinging waves. Notice that the relations $T_{mm} = 1 + R_{mm}$ and $T_{em} = R_{em}$ hold due to the continuity of the tangential electric field on the surface, which was supposed here to be infinitesimally thin.

4.2.2 Transverse-Electric (TE) plane wave incidence

For transverse electric (TE) excitation, we can assume without losing generality that the impinging electric field is given by

$$\mathbf{E}_{\mathbf{inc}} = E_0 e^{-j\sqrt{k_0{}^2 - k_x{}^2}z} e^{-jk_x x}\hat{\mathbf{y}}\,. \tag{4.17}$$

The radiated fields can be similarly calculated as in the previous section, but now also the normal component of the magnetic field can contribute to induce transverse electric currents on the surface. The transmitted electric field produced by the electric current density is

$$\mathbf{E}_{\mathbf{t}} = \mathbf{E}_{\mathbf{inc}} - \frac{jE_0 e^{-j\left(k_x x + \sqrt{k_0{}^2 - k_x{}^2}z\right)}}{2d_x d_y} \begin{pmatrix} \frac{\sqrt{k_0{}^2 - k_x{}^2}}{k_0}\left(k_x \alpha_{xz}^{em} + k_0 \alpha_{xy}^{ee}\right)\mathbf{x} \\ + \frac{k_0}{\sqrt{k_0{}^2 - k_x{}^2}}\left(k_x \alpha_{yz}^{em} + k_0 \alpha_{yy}^{ee}\right)\hat{\mathbf{y}} \\ - \frac{k_x}{k_0}\left(k_x \alpha_{xz}^{em} + k_0 \alpha_{xy}^{ee}\right)\hat{\mathbf{z}} \end{pmatrix}, \tag{4.18}$$

and the corresponding reflected field is

$$\mathbf{E}_{\mathbf{r}} = -\frac{jE_0 e^{-j\left(k_x x - \sqrt{k_0{}^2 - k_x{}^2}z\right)}}{2d_x d_y} \begin{pmatrix} \frac{\sqrt{k_0{}^2 - k_x{}^2}}{k_0}\left(k_x \alpha_{xz}^{em} + k_0 \alpha_{xy}^{ee}\right)\mathbf{x} \\ + \frac{k_0}{\sqrt{k_0{}^2 - k_x{}^2}}\left(k_x \alpha_{yz}^{em} + k_0 \alpha_{yy}^{ee}\right)\hat{\mathbf{y}} \\ + \frac{k_x}{k_0}\left(k_x \alpha_{xz}^{em} + k_0 \alpha_{xy}^{ee}\right)\hat{\mathbf{z}} \end{pmatrix}. \tag{4.19}$$

Therefore the transmission and reflection coefficients due to electric current density are similarly calculated as

$$
\begin{aligned}
T_{ee}^{e} &= 1 - jk_0\left(\frac{sec\theta\alpha_{yy}^{ee} + tan\theta\alpha_{yz}^{em}}{2d_x d_y}\right) \\
T_{me}^{e} &= -jk_0\frac{\alpha_{xy}^{ee} + sin\theta\alpha_{xz}^{em}}{2d_x d_y} \\
R_{ee}^{e} &= -jk_0\left(\frac{sec\theta\alpha_{yy}^{ee} + tan\theta\alpha_{zz}^{mm}}{2d_x d_y}\right) \\
R_{me}^{e} &= -jk_0\frac{\alpha_{xy}^{ee} + sin\theta\alpha_{xz}^{em}}{2d_x d_y}
\end{aligned}
\quad . \tag{4.20}
$$

Also the magnetic current density may be induced by both electric and magnetic fields. The transmitted electric field due to its contribution is given by

$$
\mathbf{E_t} = -\frac{jE_0 e^{-j\left(k_x x + \sqrt{k_0^2 - k_x^2}\,z\right)} k_x}{2d_x d_y\sqrt{k_0^2 - k_x^2}}\left(k_x\alpha_{zz}^{mm} + k_0\alpha_{zy}^{me}\right)\hat{\mathbf{y}}\,, \tag{4.21}
$$

and the reflected field is

$$
\mathbf{E_r} = -\frac{jE_0 e^{-j\left(k_x x - \sqrt{k_0^2 - k_x^2}\,z\right)} k_x}{2d_x d_y\sqrt{k_0^2 - k_x^2}}\left(k_x\alpha_{zz}^{mm} + k_0\alpha_{zy}^{me}\right)\hat{\mathbf{y}}\,. \tag{4.22}
$$

Therefore, transmission and reflection coefficients for TE excitation induced by the magnetic current density are

$$
\begin{aligned}
T_{ee}^{m} &= -\frac{jk_0}{2d_x d_y}\left(\tan\theta\alpha_{zy}^{me} + \sin\theta\tan\theta\alpha_{zz}^{mm}\right) \\
T_{me}^{m} &= 0 \\
R_{ee}^{m} &= -\frac{jk_0}{2d_x d_y}\left(\tan\theta\alpha_{zy}^{me} + \sin\theta\tan\theta\alpha_{zz}^{mm}\right) \\
R_{me}^{m} &= 0
\end{aligned}
\quad . \tag{4.23}
$$

By combining (4.20) and (4.23) we find the total transmission and reflection coefficients for TE excitation:

$$
\begin{aligned}
T_{ee} &= T_{ee}^{e} + T_{ee}^{m} = 1 - jk_0\left(\frac{\sec\theta\alpha_{yy}^{ee} + \sin\theta\tan\theta\alpha_{zz}^{mm}}{2d_x d_y}\right) \\
T_{me} &= T_{me}^{e} + T_{me}^{m} = -jk_0\left(\frac{\alpha_{xy}^{ee} + \sin\theta\alpha_{xz}^{em}}{2d_x d_y}\right) \\
R_{ee} &= R_{ee}^{e} + R_{ee}^{m} = -jk_0\left(\frac{\sec\theta\alpha_{yy}^{ee} + \sin\theta\tan\theta\alpha_{zz}^{mm}}{2d_x d_y}\right) \\
R_{me} &= R_{me}^{e} + R_{me}^{m} = -jk_0\left(\frac{\alpha_{xy}^{ee} + \sin\theta\alpha_{xz}^{em}}{2d_x d_y}\right)
\end{aligned}
\quad . \tag{4.24}
$$

Also in this case $T_{ee(mm)} = 1 + R_{ee(mm)}$, $T_{em(me)} = R_{em(me)}$, as expected.

4.2.3 Circularly polarized plane wave incidence

Since we are interested in the overall chiral response of the metasurface, we can now transform the reflection and transmission tensors obtained in the previous subsections from a linear into a circular basis, assuming circularly polarized inputs. This is easily obtained by considering the following transformation:

$$
\begin{aligned}
T_{LL} &= \frac{1}{2}\left(T_{ee} - iT_{em} + iT_{me} + T_{mm}\right) \\
T_{LR} &= \frac{1}{2}\left(-T_{ee} - iT_{em} - iT_{me} + T_{mm}\right) \\
T_{RL} &= \frac{1}{2}\left(-T_{ee} + iT_{em} + iT_{me} + T_{mm}\right) \\
T_{RR} &= \frac{1}{2}\left(T_{ee} + iT_{em} - iT_{me} + T_{mm}\right)
\end{aligned}
\quad . \tag{4.25}
$$

which constructs the transmission matrix for circularly polarized inputs

$$
\mathbf{T}_{cp} = \begin{pmatrix} T_{LL} & T_{LR} \\ T_{RL} & T_{RR} \end{pmatrix}, \tag{4.26}
$$

where the second letter in the subscript of each element refers to the polarization of excitation (LCP or RCP) and the first one to the transmitted polarization. We can express the elements of (4.26) in terms of the polarizability elements, obtaining:

$$T_{LL}=\left(1+\frac{\alpha_{xz}^{em}k_0\sin\theta}{2d_xd_y}\right)-\frac{ik_0}{4d_xd_y}\left(\alpha_{xx}^{ee}\cos\theta+\alpha_{yy}^{ee}\sec\theta+\alpha_{zz}^{mm}\sin\theta\tan\theta\right), \quad (4.27)$$

$$T_{LR}=\frac{ik_0}{4d_xd_y}\left(2i\alpha_{xy}^{ee}-\alpha_{xx}^{ee}\cos\theta+\alpha_{yy}^{ee}\sec\theta+\alpha_{zz}^{mm}\sin\theta\tan\theta\right), \quad (4.28)$$

$$T_{RL}=\frac{ik_0}{4d_xd_y}\left(-2i\alpha_{xy}^{ee}-\alpha_{xx}^{ee}\cos\theta+\alpha_{yy}^{ee}\sec\theta+\alpha_{zz}^{mm}\sin\theta\tan\theta\right), \quad (4.29)$$

$$T_{RR}=\left(1-\frac{\alpha_{xz}^{em}k_0\sin\theta}{2d_xd_y}\right)-\frac{ik_0}{4d_xd_y}\left(\alpha_{xx}^{ee}\cos\theta+\alpha_{yy}^{ee}\sec\theta+\alpha_{zz}^{mm}\sin\theta\tan\theta\right). \quad (4.30)$$

Similar expressions can be derived for the reflection coefficients, not reported here for brevity.

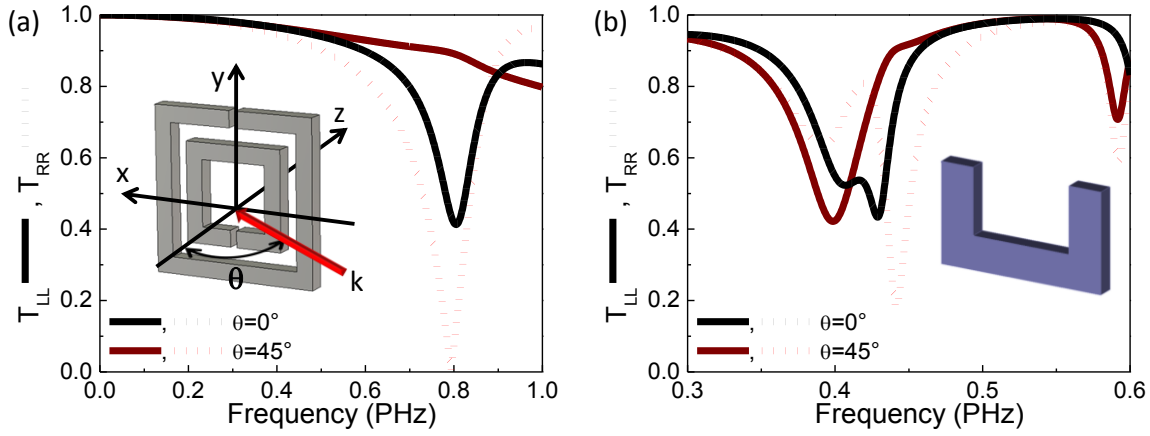

Figure 4.1: Comparison of T_{LL} (solid curves) and T_{RR} (dotted curves) at normal (black) and oblique incidence (45°, red), for (a) PEC and (b) silver split-ring-resonator metasurfaces. The unit cell element and direction of propagation is shown in the insets. In both cases, the metasurface lies on the plane and lacks mirror symmetry along the y direction, creating a nonzero term, which is responsible for the difference between T_{LL} and T_{RR} at oblique incidence.

By inspecting Eqs. (4.27)-(4.30), we find that a nonzero difference between T_{LL} and T_{RR} can only occur at oblique incidence, i.e., $\theta \neq 0$. This is due to our assumptions of infinitesimally thin surface and reciprocal response, which makes a planar 2-D surface excited at normal incidence inherently achiral for symmetry. In addition, even at oblique incidence, LCP and RCP response may be distinguishable only when the bianisotropy term α_{xz}^{em} is nonzero, which requires no mirror symmetry along $\vec{y}$. Analogously, if the plane of incidence is in the yz plane, the polarizability tensor element responsible for the difference between the two handedness is α_{yz}^{em}, which is nonzero for inclusions without mirror symmetry along $\vec{x}$, consistent with the discussions in [37]. This is shown in Figure 4.1 for two representative inclusions with asymmetric properties along $\vec{y}$. When excited at normal incidence, the metasurfaces provide $T_{LL} = T_{RR}$, but when excited at 45° in the xz plane, the two transmission coefficients support a different response for the two circular polarizations, with sharp differences around the inclusion resonance. Although this phenomenon is inherently narrowband, it may be exploited to induce chiral response on a single, ultrathin surface, which may be of interest for several optical applications (see [37] and references therein).

4.2.4 Surface impedance model

It is obvious from the previous results that a single, ultrathin metasurface can hardly provide chiral response over a broad bandwidth. For this reason, we aim to apply our results to model stacks of cascaded multilayered structures, which we can analyze using the transmission-line approach based on the results of the previous sections. This approach assumes that the main coupling mechanism among parallel metasurfaces is associated with the zero-th order diffraction from the surface, consistent with the previous analysis. This assumption is valid as long as the distance between neighboring

surfaces is larger than the period among inclusions in each plane [44]. For simplicity, we will limit our analysis to normal incidence, which ensures that the magnetic current density does not contribute to radiation, consistent with (4.15), (4.23). This ensures that our metasurface can be modeled as a 2×2 shunt admittance element with surface impedance $\underline{\mathbf{Z}}_s$ or admittance $\underline{\mathbf{Y}}_s$:

$$\underline{\mathbf{Z}}_s = \begin{pmatrix} Z_{xx} & Z_{xy} \\ Z_{yx} & Z_{yy} \end{pmatrix} = \underline{\mathbf{Y}}_s^{-1}. \tag{4.31}$$

Each element in the matrix $Z_{mn} = r_{mn} + ix_{mn}$ is a complex quantity with real part r_{mn} denoting the resistance and imaginary part x_{mn} representing the reactance. They define the relation between total electric fields on the surface and induced average current density:

$$\mathbf{K}_e = \hat{\mathbf{z}} \times \left(\mathbf{H}_{tot}\big|_{z=0^+} - \mathbf{H}_{tot}\big|_{z=0^-} \right) = \underline{\mathbf{Z}}_s^{-1} \cdot \mathbf{E}_{tot}\big|_{z=0}. \tag{4.32}$$

By using the previous results, we can obtain in closed form all the elements of the impedance tensor:

$$\underline{\mathbf{Z}}_s = \frac{\eta_0}{2\left(\left(1-T_{mm}\right)\left(1-T_{ee}\right)-T_{em}T_{me}\right)} \begin{pmatrix} T_{mm}\left(1-T_{ee}\right)+T_{em}T_{me} & T_{me} \\ T_{em} & T_{ee}\left(1-T_{mm}\right)+T_{em}T_{me} \end{pmatrix}. \tag{4.33}$$

Equation (4.33) effectively relates the impedance description to the previous analysis, connecting the surface impedance to the generalized polarizability of each metasurface. Conversely, it may also be used to retrieve the effective surface impedance with simple scattering measurements, since the transmission (reflection) coefficients are measurable quantities. Similarly to Eqs. (4.16)-(4.24), transmission (reflection) coefficients in linear basis may be expressed in terms of the impedance matrix elements as

$$
\begin{aligned}
T_{ee} &= \frac{-4Z_{xy}Z_{yx} + 2Z_{yy}\left(2Z_{xx} + \eta_0\right)}{-4Z_{xy}Z_{yx} + \left(2Z_{yy} + \eta_0\right)\left(2Z_{xx} + \eta_0\right)} \\
T_{em} &= \frac{2Z_{yx}\eta_0}{-4Z_{xy}Z_{yx} + \left(2Z_{yy} + \eta_0\right)\left(2Z_{xx} + \eta_0\right)} \\
T_{me} &= \frac{2Z_{xy}\eta_0}{-4Z_{xy}Z_{yx} + \left(2Z_{yy} + \eta_0\right)\left(2Z_{xx} + \eta_0\right)} \\
T_{mm} &= \frac{-4Z_{xy}Z_{yx} + 2Z_{xx}\left(2Z_{yy} + \eta_0\right)}{-4Z_{xy}Z_{yx} + \left(2Z_{yy} + \eta_0\right)\left(2Z_{xx} + \eta_0\right)}
\end{aligned}, \tag{4.34}
$$

and (4.25) may be used to convert them into a circular basis.

After some manipulations, we find that a nonzero impedance on the off-diagonal term $Z_{xy} = r_{xy} + ix_{xy}$ is responsible for a nonzero value of

$$
\Delta_c = T_{LR} - T_{RL} = \frac{i4Z_{xy}\eta_0}{4{Z_{xy}}^2 - \left(2Z_{xx} + \eta_0\right)\left(2Z_{yy} + \eta_0\right)}. \tag{4.35}
$$

Consistent with the previous results, reciprocity at normal incidence requires $T_{LL} = T_{RR}$, and the magnitude of the ratio between cross-polarization terms can be simply written as

$$
\left|\frac{T_{LR}}{T_{RL}}\right|^2 = \frac{\left(r_{xx} - r_{yy} + \left(x_{xy} + x_{yx}\right)\right)^2 + \left(r_{xy} + r_{yx} - \left(x_{xx} - x_{yy}\right)\right)^2}{\left(r_{xx} - r_{yy} - \left(x_{xy} + x_{yx}\right)\right)^2 + \left(r_{xy} + r_{yx} + \left(x_{xx} - x_{yy}\right)\right)^2}. \tag{4.36}
$$

This result, combined with the fact that a reciprocal metasurface satisfies $\underline{\mathbf{Z}}_s = \underline{\mathbf{Z}}_s^{\,T}$ and a lossless metasurface requires $\underline{\mathbf{Z}}_s = \underline{\mathbf{Z}}_s^{\,*T}$, where the asterisk denotes complex conjugate, indicates that losses are inherently required to introduce circular dichroism and a difference in the observed cross-polarization terms for a single metasurface. In the next chapter, we will first discuss the surface impedance model in

more details and apply these results to the more exciting possibilities offered by stacked metasurfaces.

4.3 REFERENCES

[1] Shelby, R.A., Smith, D.R., and Schultz, S. Experimental verification of a negative index of refraction, Science, 292, pp. 77-79, (2001).

[2] Zharov, A.A., Shadrivov, I.V., and Kivshar, Y.S. Nonlinear properties of left-handed metamaterials, Physical Review Letters, 91, pp. 037401, (2003).

[3] Linden, S., Enkrich, C., Wegener, M., Zhou, J.F., Koschny, T., and Soukoulis, C.M. Magnetic response of metamaterials at 100 terahertz, Science, 306, pp. 1351-1353, (2004).

[4] Smith, D.R., Pendry, J.B., and Wiltshire, M.C.K. Metamaterials and negative refractive index, Science, 305, pp. 788-792, (2004).

[5] Alù, A., and Engheta, N. Achieving transparency with plasmonic and metamaterial coatings, Physical Review E, 72, pp. 016623, (2005).

[6] Fang, N., Lee, H., Sun, C., and Zhang, X. Sub-diffraction-limited optical imaging with a silver superlens, Science, 308, pp. 534-537, (2005).

[7] Zhang, S., Fan, W.J., Panoiu, N.C., Malloy, K.J., Osgood, R.M., and Brueck, S.R.J. Experimental demonstration of near-infrared negative-index metamaterials, Physical Review Letters, 95, pp. 137404, (2005).

[8] Dolling, G., Enkrich, C., Wegener, M., Soukoulis, C.M., and Linden, S. Simultaneous negative phase and group velocity of light in a metamaterial, Science, 312, pp. 892-894, (2006).

[9] Leonhardt, U. Optical conformal mapping, Science, 312, pp. 1777-1780, (2006).

[10] Schurig, D., Mock, J.J., Justice, B.J., Cummer, S.A., Pendry, J.B., Starr, A.F., and Smith, D.R. Metamaterial electromagnetic cloak at microwave frequencies, Science, 314, pp. 977-980, (2006).

[11] Engheta, N. Circuits with light at nanoscales: Optical nanocircuits inspired by metamaterials, Science, 317, pp. 1698-1702, (2007).

[12] Lezec, H.J., Dionne, J.A., and Atwater, H.A. Negative refraction at visible frequencies, Science, 316, pp. 430-432, (2007).

[13] Rockstuhl, C., Lederer, F., Etrich, C., Pertsch, T., and Scharf, T. Design of an artificial three-dimensional composite metamaterial with magnetic resonances in the visible range of the electromagnetic spectrum, Physical Review Letters, 99, pp. 017401, (2007).

[14] Shalaev, V.M. Optical negative-index metamaterials, Nature Photonics, 1, pp. 41-48, (2007).

[15] Soukoulis, C.M., Linden, S., and Wegener, M. Negative refractive index at optical wavelengths, Science, 315, pp. 47-49, (2007).

[16] Tsakmakidis, K.L., Boardman, A.D., and Hess, O. 'Trapped rainbow' storage of light in metamaterials, Nature, 450, pp. 397-401, (2007).

[17] Landy, N.I., Sajuyigbe, S., Mock, J.J., Smith, D.R., and Padilla, W.J. Perfect metamaterial absorber, Physical Review Letters, 100, pp. 207402, (2008).

[18] Papasimakis, N., Fedotov, V.A., Zheludev, N.I., and Prosvirnin, S.L. Metamaterial Analog of Electromagnetically Induced Transparency, Physical Review Letters, 101, pp. 253903, (2008).

[19] Valentine, J., Zhang, S., Zentgraf, T., Ulin-Avila, E., Genov, D.A., Bartal, G., and Zhang, X. Three-dimensional optical metamaterial with a negative refractive index, Nature, 455, pp. 376-379, (2008).

[20] Liu, N., Langguth, L., Weiss, T., Kastel, J., Fleischhauer, M., Pfau, T., and Giessen, H. Plasmonic analogue of electromagnetically induced transparency at the Drude damping limit, Nature Materials, 8, pp. 758-762, (2009).

[21] Plum, E., Zhou, J., Dong, J., Fedotov, V.A., Koschny, T., Soukoulis, C.M., and Zheludev, N.I. Metamaterial with negative index due to chirality, Physical Review B, 79, pp. 035407, (2009).

[22] J. C. Bose. On the rotation of plane of polarisation of electric waves by a twisted structure, Proceedings of the Royal Society, 63, pp. 146-152, (1898).

[23] Sarkar, T.K., and Sengupta, D.L. An appreciation of J. C. Bose's pioneering work in millimeter waves, IEEE Antennas and Propagation Magazine, 39, pp. 55-63, (1997).

[24] Chiou, T.H., Kleinlogel, S., Cronin, T., Caldwell, R., Loeffler, B., Siddiqi, A., Goldizen, A., and Marshall, J. Circular polarization vision in a stomatopod crustacean, Current Biology, 18, pp. 429-434, (2008).

[25] Roberts, N.W., Chiou, T.H., Marshall, N.J., and Cronin, T.W. A biological quarter-wave retarder with excellent achromaticity in the visible wavelength region, Nature Photonics, 3, pp. 641-644, (2009).

[26] Schwind, R. Polarization vision in water insects and insects living on a moist substrate, Journal of Comparative Physiology a-Sensory Neural and Behavioral Physiology, 169, pp. 531-540, (1991).

[27] Shashar, N., Rutledge, P.S., and Cronin, T.W. Polarization vision in cuttlefish - A concealed communication channel, Journal of Experimental Biology, 199, pp. 2077-2084, (1996).

[28] Zhao, Y., Belkin, M.A., and Alù, A. Twisted optical metamaterials for planarized ultrathin broadband circular polarizers, Nature Communications, 3, pp. 870, (2012).

[29] Gansel, J.K., Thiel, M., Rill, M.S., Decker, M., Bade, K., Saile, V., von Freymann, G., Linden, S., and Wegener, M. Gold Helix Photonic Metamaterial as Broadband Circular Polarizer, Science, 325, pp. 1513-1515, (2009).

[30] Seet, K.K., Mizeikis, V., Matsuo, S., Juodkazis, S., and Misawa, H. Three-dimensional spiral-architecture photonic crystals obtained by direct laser writing, Advanced Materials, 17, pp. 541-545, (2005).

[31] Maruo, S., Nakamura, O., and Kawata, S. Three-dimensional microfabrication with two-photon-absorbed photopolymerization, Optics Letters, 22, pp. 132-134, (1997).

[32] Deubel, M., Von Freymann, G., Wegener, M., Pereira, S., Busch, K., and Soukoulis, C.M. Direct laser writing of three-dimensional photonic-crystal templates for telecommunications, Nature Materials, 3, pp. 444-447, (2004).

[33] Lee, K.S., Yang, D.Y., Park, S.H., and Kim, R.H. Recent developments in the use of two-photon polymerization in precise 2D and 3D microfabrications, Polymers for Advanced Technologies, 17, pp. 72-82, (2006).

[34] Kuwata-Gonokami, M., Saito, N., Ino, Y., Kauranen, M., Jefimovs, K., Vallius, T., Turunen, J., and Svirko, Y. Giant optical activity in quasi-two-dimensional planar nanostructures, Physical Review Letters, 95, pp. 227401, (2005).

[35] Rogacheva, A.V., Fedotov, V.A., Schwanecke, A.S., and Zheludev, N.I. Giant gyrotropy due to electromagnetic-field coupling in a bilayered chiral structure, Physical Review Letters, 97, pp. 177401, (2006).

[36] Decker, M., Klein, M.W., Wegener, M., and Linden, S. Circular dichroism of planar chiral magnetic metamaterials, Optics Letters, 32, pp. 856-858, (2007).

[37] Plum, E., Liu, X.X., Fedotov, V.A., Chen, Y., Tsai, D.P., and Zheludev, N.I. Metamaterials: Optical Activity without Chirality, Physical Review Letters, 102, pp. 113902, (2009).

[38] Wei, Z., Cao, Y., Fan, Y., Yu, X., and Li, H. Broadband polarization transformation via enhanced asymmetric transmission through arrays of twisted complementary split-ring resonators, Applied Physics Letters, 99, pp. 221907, (2011).

[39] Demetriadou, A., and Pendry, J.B. Extreme chirality in Swiss roll metamaterials, Journal of Physics-Condensed Matter, 21, pp. 376003, (2009).

[40] Maradudin, A. A. Structured Surfaces as Optical Metamaterials, eds. Alù, A., and Engheta, N., Chapter 3 "Optical Wave Interaction with Two-Dimensional Arrays of Plasmonic Nanoparticles" (Cambridge University Press, New York) pp. 58-93, (2011)

[41] Liu, X.-X., and Zhao, Y., Determination of full dynamic polarizability tensor of arbitrary sub-wavelength inclusions in meta-arrays, under review.

[42] Sersic, I., Tuambilangana, C., Kampfrath, T., and Koenderink, A.F. Magnetoelectric point scattering theory for metamaterial scatterers, Physical Review B, 83, pp. 245102, (2011).

[43] Serdyukov, A.N., Semchenko, I.V., Tretyakov, S.A., and Sihvola, A. Electromagnetics of Bi-anisotropic Materials: Theory and Applications (Gordon and Breach, Amsterdam), (2001).

[44] Zhao, Y., Engheta, N., and Alù, A. Homogenization of plasmonic metasurfaces modeled as transmission-line loads, Metamaterials, 5, pp. 90-96, (2011).

[45] Johnson, P.B., and Christy, R.W. Optical constants of noble metals, Physical Review B, 6, pp. 4370-4379, (1972).

Chapter 5: A Surface Impedance Model for Homogenized Two Dimensional Metasurface

In the previous chapter, we discussed the theoretical analysis of a single metasurface using the Green's function approach, and we have shown such single metasurface may exhibit circularly polarized filtering effect only at oblique incidence for any reciprocal surface, which is often not practical and narrowband. To achieve the goal of circularly polarized vision, normal incidence and broadband are required, consequently we proceed to more complicated designs by involving more layers of metasurfaces and the proper arrangements of their stacking to provide us with more degrees of freedom in the designs.

Before we can proceed with the multilayer approach, we need to seek a better way to model the complex wave-matter interaction between single and multiple metasurfaces with the electromagnetic waves to simplify the numerical calculations. In this chapter, we will focus on discussing the analytical model of cascaded plasmonic metasurfaces excited by normally incident plane waves using a transmission-line shunt admittance model, which relates the effective surface admittance of a single metasurface to its inclusion polarizability and its plane wave reflection and transmission coefficients. We apply these concepts to predict the wave interaction of more complicated setups in which two or more stacked surfaces are separated by a varying distance, and possibly rotated with respect to one another, for normal incidence excitation. We show that the analytical model holds very well under suitable conditions, and we verify our analytical results with full-wave numerical simulations, including material dispersion and loss of optical materials.

5.1 INTRODUCTION

Metamaterials are usually described through an averaged effective bulk permittivity and permeability, in a similar manner metasurfaces may be described by an averaged surface impedance (or admittance), compactly characterizing their bulk wave interaction properties. These concepts have been introduced several years ago to simplify the design and modeling of properly patterned conductors, or frequency selective surfaces, at microwave frequencies for antenna and filtering applications [1].

Using the optical nanocircuit concepts [2],[3], analogous impedance concepts may be extended to the optical domain to characterize and model planar and conformal 2D arrays, in a similar fashion as they have been applied to realize 3D optical metamaterials [4]. In particular in the field of optics, metasurfaces may offer various advantages for some applications compared to bulk metamaterials in terms of ease of fabrication (3-D optical metamaterials are more challenging to realize), integration with other photonic devices and extremely low profile. In addition, the exotic features of plasmonic materials [5] in the visible domain may provide the necessary tools to induce compact resonances and anomalous optical response with naturally available materials.

In this chapter, we aim at modeling thin plasmonic metasurfaces with an averaged transmission-line shunt admittance tensor based on the dipolar polarizability of the inclusions forming the array, taking rigorously into account the full dynamic interaction within the array and the possible cross-polarization coupling. In particular, we aim at verifying whether this compact description, which may be retrieved for an isolated array excited at normal incidence from its reflection and transmission properties, as already shown for isolated metafilms [6], may hold to describe their optical interaction in the case of more complex setups, in which cascaded and possibly rotated metasurfaces are considered. We investigate and compare homogenized metasurface models with full-

wave numerical simulations based on finite-integration techniques, in order to outline the limitations and ultimate conditions under which the averaged optical surface impedance concept may accurately describe the complex wave interaction of planar plasmonic metasurfaces.

5.2 PLANE-WAVE INTERACTION WITH PLANAR METASURFACES

Consider a two dimensional metasurface consisting of generically shaped inclusions with periods d_x, d_y, illuminated by an arbitrarily polarized plane wave, as depicted in Figure 5.1. The array is positioned at $z = 0$ and the impinging plane wave impinges on the surface at an arbitrary angle θ, similarly as the configuration in the previous chapter. The excitation may be decomposed, without loss of generality, into combinations of transverse-electric (TE) and transverse-magnetic (TM) polarizations with respect to the z axis. Moreover, we assume in our analysis that the inclusions are much smaller than the wavelength of operation $\left(k_0 d << 1\right)$, with k_0 being the background wave number, and that they are not too densely packed, so that we can model their interaction within the dipolar approximation, i.e., higher-order multiples may be neglected. It has been shown that a plasmonic metasurface may behave as an effective homogeneous impedance surface, as long as these conditions are satisfied [7],[8]. Under these assumptions, the metasurface features, and in particular its anomalous resonance, are mainly based on the electromagnetic properties of the individual inclusions, and less on lattice effects, as they would be in regular gratings. Since we assume that the metasurface is ultrathin, the normal component of the current distribution may be safely neglected and the geometry and properties of the inclusions may be compactly described in the dipolar limit by the transverse electric polarizability tensor $\underline{\boldsymbol{\alpha}}$, which relates the induced dipole moment to the tangential component of the local electric field at the

particle location: $\mathbf{p} = \underline{\boldsymbol{\alpha}} \cdot \left(\mathbf{E}_{loc} \times \hat{\mathbf{z}} \right)_t$, where the subscript t indicates that the vector has only two components, tangential to the metasurface plane. For nanorods (as in the inset of Figure 5.2a), no polarization coupling occurs and the 2×2 polarizability tensor is diagonal; for more complicated shapes, such as C-shaped inclusions (Figure 5.2c), the polarizability tensor is full. For simplicity of analysis, we neglect here the possible presence of artificial magnetic and/or bianisotropic effects, which may arise at oblique incidence in the general case. In the following numerical examples, we will focus on normal illumination, for which these effects cannot arise. An extended model will be presented in a future contribution, including these and other possible higher-order effects.

The local electric field on the inclusions under these assumptions may be generally written as the superposition of the impinging field $\mathbf{E_{inc}}$ and the contribution from all the other inclusions in the array:

$$\left(\mathbf{E}_{loc} \times \hat{\mathbf{z}} \right)_t = \underline{\mathbf{C}} \cdot \mathbf{p} + \left(\mathbf{E}_{inc} \times \hat{\mathbf{z}} \right)_t , \tag{5.1}$$

where $\underline{\mathbf{C}}$ is the interaction dyadic, in general function of the incidence angle, whose expressions may be calculated by extending the results in [9],[10] to the cross-polarization coupling terms. This 2×2 tensor takes into account, within the dipolar approximation, of the full coupling among the inclusions in the array, and its elements may be calculated with fast-converging expressions using analytical techniques analogous to [9],[10]. Using the definition of polarizability, we can write (5.1) as

$$\mathbf{p} = \left(\underline{\boldsymbol{\alpha}}^{-1} - \underline{\mathbf{C}} \right)^{-1} \cdot \left(\mathbf{E}_{inc} \times \hat{\mathbf{z}} \right)_t = \underline{\boldsymbol{\alpha}}_s \cdot \left(\mathbf{E}_{inc} \times \hat{\mathbf{z}} \right)_t , \tag{5.2}$$

compactly describing the polarization properties of the metasurface via the generalized polarizability tensor $\underline{\boldsymbol{\alpha}}_s = \begin{pmatrix} \alpha_{xx} & \alpha_{xy} \\ \alpha_{yx} & \alpha_{yy} \end{pmatrix}$, whose elements embed the coupling effects

within the array. It should be stressed that this tensor is in general a function of the angle of incidence, combining the spatial dispersion effects inherently present in the elements of $\underline{\mathbf{C}}$. It is expected that for sub-wavelength periods these effects may be minor [11].

In the following, we relate the transmission T and reflection R coefficients of the metasurface to this generalized surface polarizability tensor using an averaged field approach consistent with [9],[10], applied here to the full tensor $\underline{\boldsymbol{\alpha}}$, with the objective of analytically modeling the metasurface starting from its scattering properties. We verify and validate this model in the next section. We further assume an $e^{j\omega t}$ temporal dependence.

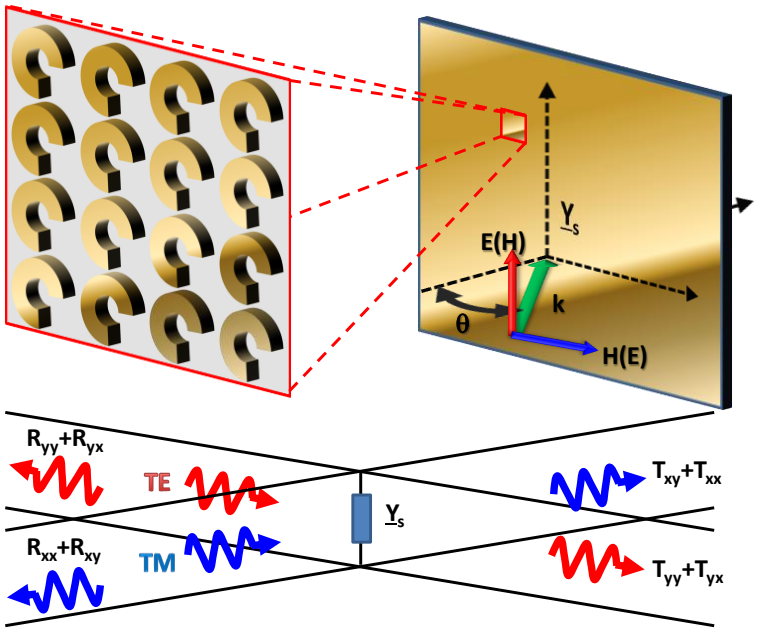

Figure 5.1: Geometry of the problem: a planar metasurface illuminated by an arbitrarily polarized plane wave and its transmission-line model. (Reprinted from Metamaterials 5 (2), 90-96, (2011). Copyright 2011 Elsevier)

From the previous chapter, we know that, for TE excitation the incident electric field can be written as $\mathbf{E}_{\mathbf{inc}} = E_0 e^{-jk_x x} e^{-j\sqrt{k_0^2 - k_x^2}\,z}\mathbf{y}$, with $\theta = \sin^{-1} k_x / k_0$, where we

implicitly assume incidence along one of the array axes for simplicity. In the limit in which the metasurface period is small, of interest here, the induced dipoles radiate only the dominant diffraction order, whose amplitude may be analytically related to the averaged current density $\mathbf{J}_s = j\omega\mathbf{p}/\left(d_x d_y\right)$ in a way analogous to the analysis in [9], generalized here to the presence of cross-polarization coupling.

After some algebra and using standard transmission-line concepts with an $e^{j\omega t}$ time variation, the reflection and transmission coefficients are related to the surface polarizability tensor elements as:

$$\begin{aligned} R_{yy} &= -\frac{j\mu_0\omega^2}{2d_x d_y k_0 \cos\theta}\alpha_{yy} \\ R_{xy} &= -\frac{j\mu_0\omega^2}{2d_x d_y k_0}\alpha_{xy} \\ T_{yy} &= 1-\frac{j\mu_0\omega^2}{2d_x d_y k_0 \cos\theta}\alpha_{yy} \\ T_{xy} &= -\frac{j\mu_0\omega^2}{2d_x d_y k_0}\alpha_{xy} \end{aligned} \quad , \tag{5.3}$$

where μ_0 is the background permeability. The detailed algebraic manipulation can be referred to the last chapter. The generic iy subscript of each element refers to the polarization of the radiated electric field (i) with respect to that of the impinging field, in this case y. The first element in each row therefore indicates the co-polarized radiated fields, i.e., the complex amplitudes of TE reflected and transmitted waves, associated with the diagonal term α_{yy} in the generalized polarizability tensor. The second terms, on the other hand, are associated with the cross-polarization coupling and off-diagonal term α_{xy}.

For TM excitation, the impinging field may be expressed by duality using the impinging magnetic field $\mathbf{H_{inc}} = \frac{E_0}{\eta_0} e^{-jk_x x} e^{-j\sqrt{k_0^2 - k_x^2}z} \mathbf{y}$. In this case, the reflection and transmission coefficients for electric field become:

$$\begin{aligned} R_{xx} &= -\frac{jk_0 cos\theta}{2d_x d_y \epsilon_0} \alpha_{xx} \\ R_{yx} &= -\frac{jk_0}{2d_x d_y \epsilon_0} \alpha_{yx} \\ T_{xx} &= 1 - \frac{jk_0 cos\theta}{2d_x d_y \epsilon_0} \alpha_{xx} \\ T_{yx} &= -\frac{jk_0}{2d_x d_y \epsilon_0} \alpha_{yx} \end{aligned}, \tag{5.4}$$

where ε_0 is the background permittivity and similar considerations hold: the first term in each row corresponds to TM scattered waves, and the second one to cross-polarization coupling. For reciprocal inclusions, for which the tensors $\underline{\boldsymbol{\alpha}}$ and $\underline{\boldsymbol{\alpha}}_s$ are symmetric, the reflection and transmission tensors $\underline{\mathbf{R}}$ and $\underline{\mathbf{T}}$, defined as in (5.3)-(5.4), are also symmetric, as expected. Since we have assumed the presence of only tangential currents, the continuity of tangential electric fields ensures:

$$\underline{\mathbf{I}} + \underline{\mathbf{R}} = \underline{\mathbf{T}}, \tag{5.5}$$

where $\underline{\mathbf{I}}$ is the identity tensor. In practice, this is valid only for optically thin inclusions and in absence of magnetic or bianisotropic effects, for which no normal polarization or magnetization currents arise, as assumed here. An improved model including these effects may be obtained with similar procedures, but this goes beyond the purpose of this chapter.

5.3 ADMITTANCE TENSOR AND TRANSMISSION-LINE MODEL

Under the assumptions of the previous sections, an optically thin metasurface may be effectively modeled as a shunt admittance element in a generalized 2×2 transmission line model, as sketched in the bottom of Figure 5.1. In this section, we derive the expressions that relate the admittance tensor elements to the scattering parameters, in order to retrieve them from numerical simulations. We then validate this transmission-line model by applying it to more complicated scenarios.

5.3.1 Retrieval of the surface admittance tensor elements

In order to model the scattering problem with a transmission-line model, as sketched in Figure 5.1, we need to interpret the tangential components of the total electric field as voltage waves traveling in the direction normal to the metasurface and the magnetic fields as the associated currents [12]. Eq. (5.5) ensures that the metasurface may indeed be modeled as a shunt admittance element, since voltage waves are continuous, and the cross-polarization between TE and TM waves requires a tensorial form $\underline{\mathbf{Y}}_s = \begin{pmatrix} Y_{xx} & Y_{xy} \\ Y_{yx} & Y_{yy} \end{pmatrix}$, satisfying:

$$\mathbf{J}_s = \hat{\mathbf{z}} \times \left(\mathbf{H}_{tot}\big|_{z=0^+} - \mathbf{H}_{tot}\big|_{z=0^-} \right) = \underline{\mathbf{Y}}_s \cdot \mathbf{E}_{tot}\big|_{z=0} \tag{5.6}$$

where we use here the total fields at the metasurface location. Using (5.6), we can relate the elements of the admittance tensor to the transmission coefficients as:

$$\underline{\mathbf{Y}}_s = -\frac{2}{\eta_0} \begin{pmatrix} 1+\dfrac{T_{yy}}{\left(T_{xy}T_{yx}-T_{xx}T_{yy}\right)} & \dfrac{-T_{xy}}{\left(T_{xy}T_{yx}-T_{xx}T_{yy}\right)} \\ \dfrac{-T_{yx}}{\left(T_{xy}T_{yx}-T_{xx}T_{yy}\right)} & 1+\dfrac{T_{xx}}{\left(T_{xy}T_{yx}-T_{xx}T_{yy}\right)} \end{pmatrix}, \tag{5.7}$$

which allows, using (5.2)-(5.4) to describe the metasurface admittance in terms of its polarizability tensor. Eq. (5.7) is also useful for retrieving the admittance model in terms of simple scattering experiments, as the full tensor may be determined once the transmission (or reflection) properties of the metasurface are known for illumination in both polarizations, consistent with Figure 5.1.

5.3.2 Application of the transmission-line model

Although the admittance model provides a compact way to represent the metasurface electromagnetic properties, it would not be of significance if its calculated value were not applicable to more complex scenarios than just the scattering from a single metasurface. We concentrate here on the possibility to apply this model to calculate the scattering properties of two stacked metasurfaces with separation distance t and identical properties, for which one of them has been arbitrarily rotated with an angle φ. As long as the admittance model has a proper meaning, its definition should be able to describe the scattering from a given metasurface even after such rotation, by using the transformation:

$$\underline{\mathbf{Y}}_s^{Rot} = \underline{\mathbf{Q}} \cdot \underline{\mathbf{Y}}_s \cdot \underline{\mathbf{Q}}^T , \tag{5.8}$$

where the rotation matrix $\underline{\mathbf{Q}} = \begin{pmatrix} cos\varphi & sin\varphi \\ -sin\varphi & cos\varphi \end{pmatrix}$ effectively rotates the reference system of Figure 5.1.

As an example, the transmission coefficients in Eq. (5.4) are modified after such rotation as:

$$T_{xx}^{Rot} = \frac{4+\left(-Y_{xx}+Y_{yy}\right)\eta_0 cos2\varphi+\left(Y_{xx}+Y_{yy}\right)\eta_0-\left(Y_{xy}+Y_{yx}\right)\eta_0 sin2\varphi}{4+2\left(Y_{xx}+Y_{yy}\right)\eta_0+\left(-Y_{xy}Y_{yx}+Y_{xx}Y_{yy}\right)\eta_0{}^2}$$
$$T_{yx}^{Rot} = \frac{2\eta_0\left(-Y_{yx}cos^2\varphi+\left(Y_{xx}-Y_{yy}\right)cos\varphi sin\varphi+Y_{xy}sin^2\varphi\right)}{4+2\left(Y_{xx}+Y_{yy}\right)\eta_0+\left(-Y_{xy}Y_{yx}+Y_{xx}Y_{yy}\right)\eta_0{}^2} \quad , \qquad (5.9)$$

where $\eta_0 = \sqrt{\mu_0/\varepsilon_0}$ and the other scattering coefficients may be obtained applying reciprocity and Eq. (5.5).

In the case of two stacked metasurfaces, one of them arbitrarily rotated, we can calculate the total reflection and transmission coefficients using simple transmission-line formulas, as long as the separation t is large enough to ensure that the coupling is dominated by the zero-th diffraction order and the admittance model holds. In such scenario, the overall admittance may be seen as the cascade of the two admittance tensors $\underline{\mathbf{Y}}_s^{Rot}+\eta_0^{-1}\underline{\mathbf{I}}$ and $\underline{\mathbf{Y}}_s$, separated by a transmission-line segment of length t. Using generalized ABCD matrices the total transmission and reflection from the stack may be calculated for an arbitrary number of metasurfaces, as long as the surface admittance tensors are known.

5.4 NUMERICAL SIMULATIONS AND DISCUSSIONS

In this section, we validate the transmission-line model described in the previous section with full-wave numerical simulations of specific examples of interest, using commercially available software based on finite integration technique [13]. In particular, we test whether the retrieved admittance properties obtained for the excitation of one single metasurface may be used to model rotated and stacked arrays. We consider here gold metasurfaces using experimentally extracted values of permittivity [14], whose inclusion shape is depicted in the insets of Figure 5.2. In particular, two sample metasurfaces are considered: one with nanorod inclusions (Figure 5.2a) and the other

with C-shaped inclusions (Figure 5.2c), as representative metasurfaces of interest. The nanorods have a length of 70nm and width 20nm; the C-shaped inclusions have outer radius of 40nm, inner radius of 20nm, and an opening of 60° arc; all metasurfaces have thickness of 20nm, and a square lattice with period of 100nm.

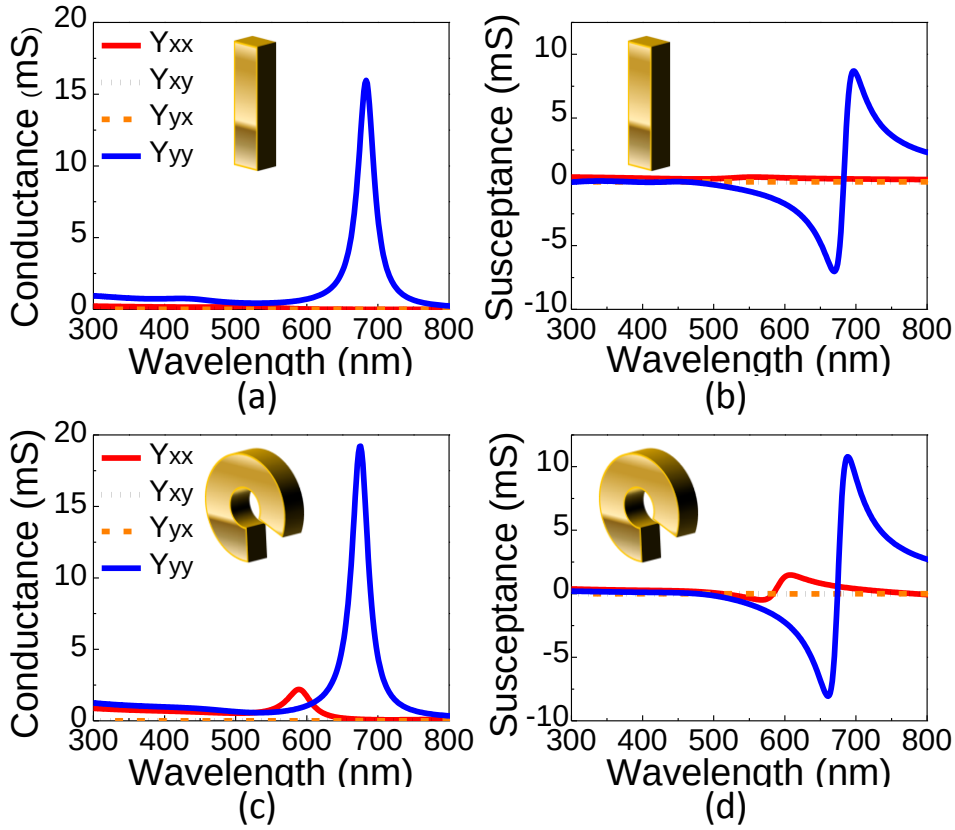

Figure 5.2: Retrieved surface admittance based on Eq. (5.7) for metasurfaces with (a), (b): nanorod inclusions; (c), (d): C shaped inclusions. Panels (a) and (c) show the real parts; (b) and (d) show the imaginary parts. (Reprinted from Metamaterials 5 (2), 90-96, (2011). Copyright 2011 Elsevier)

Figure 5.2 shows the calculated metasurface admittance $\underline{\mathbf{Y}}_s$ (real and imaginary parts), retrieved using Eq. (5.7) from the simulated transmission coefficients for normal incidence. We have verified that in both cases Eq. (5.5) is satisfied to a very large degree, ensuring that the shunt admittance model is appropriate. It is seen how the surface

conductance is moderate all over the spectrum of interest, except at the inclusion resonance, ensuring that absorption in the gold inclusions is quite moderate in this regime, consistent with the fact that the coupling among nanoparticles may improve the robustness to Ohmic absorption [4]. As expected, the nanorod metasurface (panels a,b) has zero cross-polarization terms and response dominated by the diagonal term along the nanorod direction. In particular, its susceptance is resonant around $680\,\mathrm{nm}$, ensuring a strong resonant response and correspondingly large reflection. In contrast, the C-shaped metasurface (panels c,d) has a full admittance tensor and a more complex response, as expected from this geometry. The two diagonal elements of the admittance tensor are still dominant, and they support two resonances at different wavelengths. It is noticed, in particular, that for the C-shaped metasurface our assumption of negligible magnetic and bianisotropic effects holds only for normal incidence, as assumed in these simulations.

Figures 5.3 and 5.4 validate the surface admittance models of Figure 5.2 by comparing the transmission spectra (amplitude and phase) for the case of rotated metasurfaces. The simulated transmission curves for rotation angles of $45°$ (panels a,b) and 90° (c,d) are compared with the analytical curves obtained after analytically rotating the surface admittance retrieved in Figure 5.2 before rotation, using (5.8)-(5.9). For both types of inclusions, the analytically predicted transmission coefficients match extremely well with those extracted from numerical simulations, ensuring that the transmission-line model is invariant with the angle.

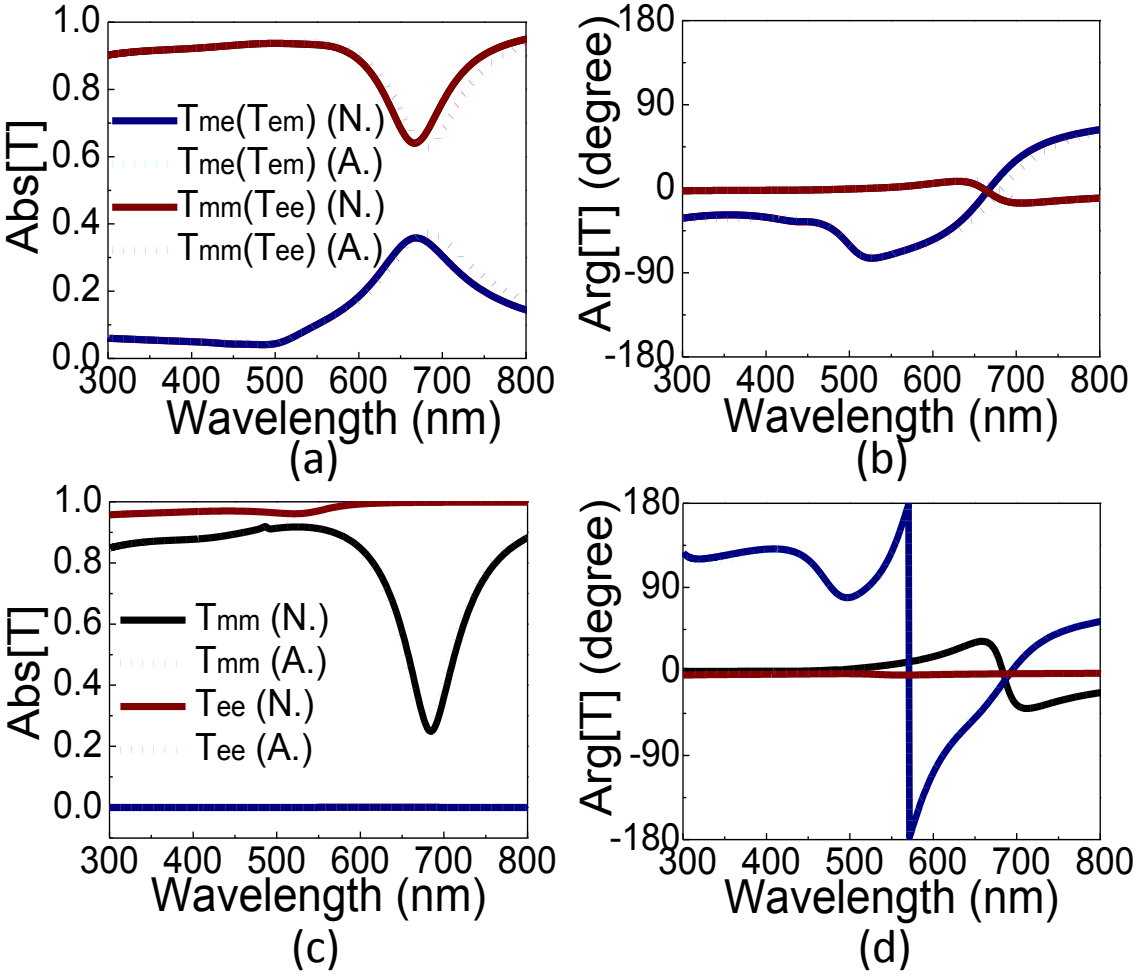

Figure 5.3: For nanorod inclusions (Figure 5.2a,b), comparison between the simulated transmission coefficients after rotation and the analytical model (5.9), for rotation angles of: (a,b) 45° and (c,d) 90°. Solid curves represent numerical simulations, dotted curves refer to analytical results. (Reprinted from Metamaterials 5 (2), 90-96, (2011). Copyright 2011 Elsevier)

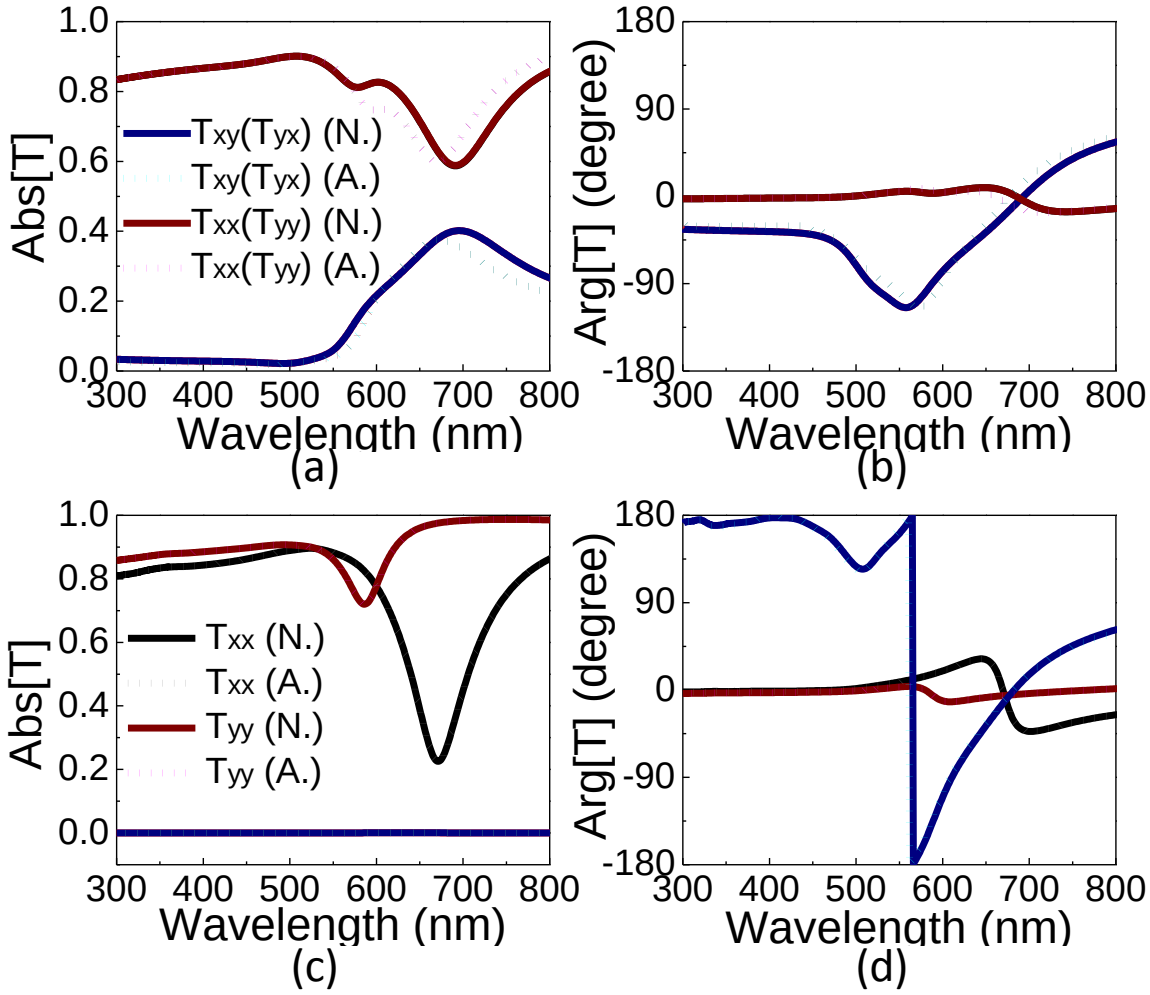

Figure 5.4: For C-shaped inclusion (Figure 5.2c,d), similar to Figure 5.3: comparison between the simulated transmission coefficients after rotation and the analytical model (5.9), for rotation angles of: (a,b) 45° and (c,d) 90°. Solid curves represent numerical simulations, dotted curves refer to analytical results. (Reprinted from Metamaterials 5 (2), 90-96, (2011). Copyright 2011 Elsevier)

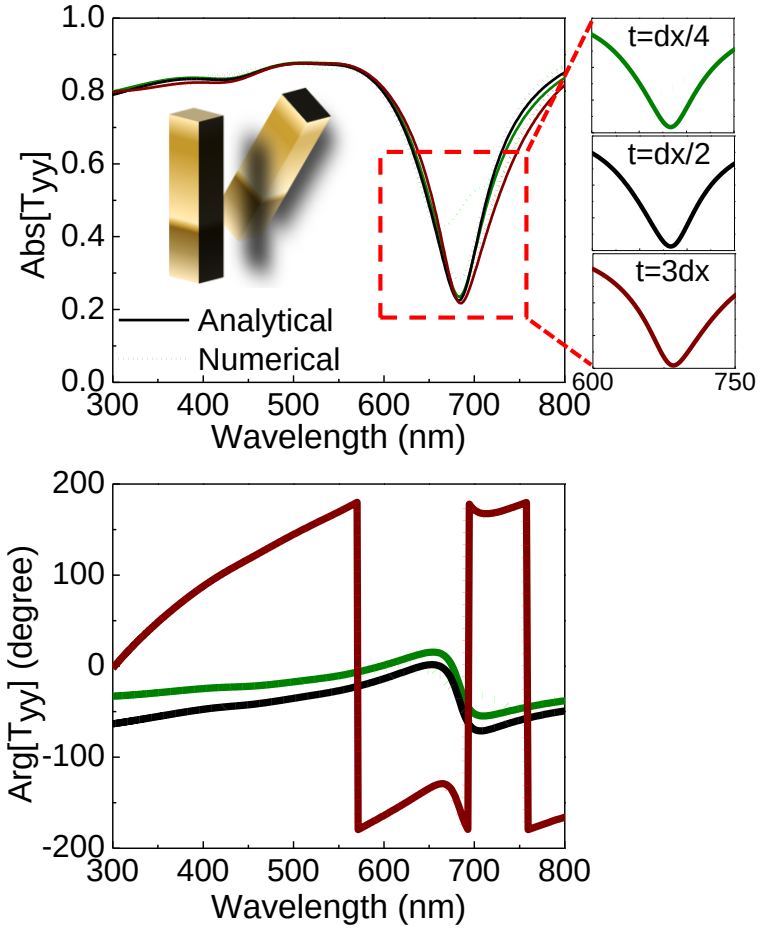

Figure 5.5: Transmission coefficient of two cascaded metasurfaces with different separation distances, as indicated in the legend. Dotted curves represent numerical simulations, solid curves refer to analytical transmission-line models. (Reprinted from Metamaterials 5 (2), 90-96, (2011). Copyright 2011 Elsevier)

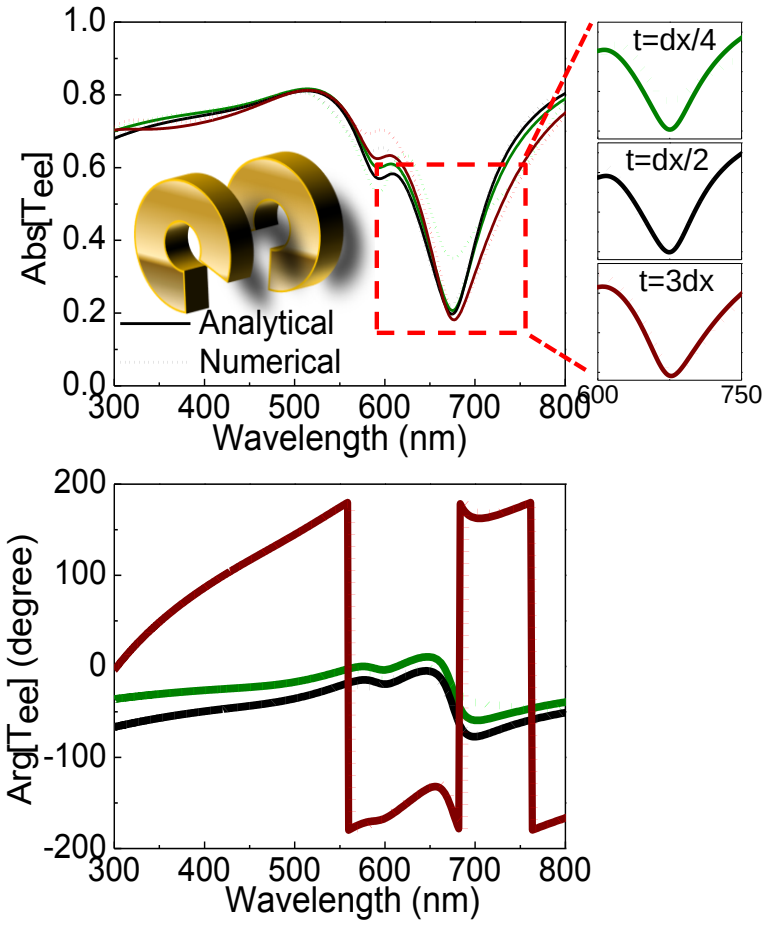

Figure 5.6: Transmission coefficient of two cascaded metasurfaces with different separation distances, as indicated in the legend. Dotted curves represent numerical simulations, solid ones refer to analytical transmission-line models. The inset shows the unit cells of the cascaded structure, that the second metasurface with unit cell inclusion rotated as an in-plane angle with respect to the first metasurface. The outer radius of the split ring is 40 nm, and the inner radius is 20nm, embedded in a 100 nm by 100 nm square lattice, and an opening of 60° arc; both metasurfaces have thickness of 20 nm.

For 45° rotation, small discrepancies arise at higher frequencies, due to the variations in the effective lattice configuration after rotation, which affects the contribution of the interaction dyadic $\underline{\mathbf{C}}$ to the admittance tensor. For 90° rotation, due to the square lattice, the curves exactly overlap, as was expected, whereas for all other angles some small discrepancies arise in the frequency regions where the interaction

constants are more effective. In particular, due to the lattice configuration, 45° rotation is the worst-case scenario. Yet, our analytical model captures with high precision an arbitrary rotation and it can accurately describe the metasurface wave interaction, both in amplitude and phase. Analogous results may be obtained for the reflection coefficients, satisfying Eq. (5.5).

In Figure 5.5 we analyze the more complex scenario of a stack of two nanorod metasurfaces, one of them rotated by 60°, as schematically depicted in the inset of Figure 5.5. The figure shows the magnitude and phase of the transmission coefficient T_{yy}, calculated using full-wave numerical simulations (dotted lines), and compared with the one obtained from the transmission-line model (solid lines), as described in the previous section, using the original surface admittance model retrieved in Figure 5.2 (a,b). The figure refers to three different separation distances between the two metasurfaces: $t = d_x / 4$ (green curves), $t = d_x / 2$ (black), $t = 3d_x$ (red). In all the considered examples the analytical model matches with the simulated results with good accuracy. When the separation distance is very small, however, the analytical model fails, to some extent, to reproduce correctly the sharp variations at the transmission dip near the metasurface resonance (highlighted in the inset of Figure 5.5a), due to the strong coupling among the two metasurfaces via higher-order evanescent diffraction orders. For larger separation distances, these higher-order effects are expectedly negligible, and excellent agreement is again obtained, ensuring that the transmission-line admittance model is accurate even in describing the complex wave interaction between two stacked metasurfaces with arbitrary rotation. Extension to a larger number of stacked layers is easily envisioned using simple transmission-line formulas. The propagation properties may be generally obtained using *ABCD* matrices representing the arbitrary gaps between neighboring metasurfaces, providing the ability to model complex optical

metamaterial geometries as stacks of impedance surfaces applying the formalism in [15],[16].

A similar phenomenon is observed for two stacked metamsurfaces with C shaped inclusions. Figure 5.6 shows the comparison between analytical results and full-wave simulations for two cascaded metasurfaces made of gold split ring resonator inclusions, for a fixed rotation angle of 60° and a varying distance between the two surfaces. It is seen that for distances smaller than a quarter of the period of the metasurface the discrepancy becomes noticeable, indicating a noticeable amount of near-field coupling involving higher-order evanescent diffraction orders.

5.5 REFERENCES

[1] B. A. Munk, Frequency Selective Surfaces: Theory and Design, first ed., Wiley, New York, 2000.

[2] N. Engheta, Circuits with light at nanoscales: Optical nanocircuits inspired by metamaterials, Science 317, 1698-1702, (2007).

[3] N. Engheta, A. Salandrino, A. Alù, Circuit elements at optical frequencies: nanoinductors, nanocapacitors and nanoresistors, Phys. Rev. Letters 95, 095504, (2005).

[4] A. Alù, Engheta, N. Three-dimensional nanotransmission lines at optical frequencies: A recipe for broadband negative-refraction optical metamaterials, Phys. Rev. B 75, 024304, (2007).

[5] C. F. Bohren, D. R. Huffman, Absorption and Scattering of Light by Small Particles, first ed., Wiley, New York,1983.

[6] C. L. Holloway, M. A. Mohamed, E. F. Kuester, Reflection and transmission properties of a metafilm: with an application to a controllable surface composed of resonant particles, IEEE Trans. Electromagn. Compat. 47, 853-865, (2005).

[7] C.L. Holloway, A. Deinstfrey, E.F. Kuester, J. F. O'Hara, A. K. Azad, A. J. Taylor, A discussion on the interpretation and characterization of metafilms-metasurfaces: the twodimensional equivalent of metamaterials, Metamaterials 3, 100–112, (2009).

[8] F. J. Garcia-Vidal, L. Martin-Moreno, J. B. Pendry, Surfaces with holes in them: new plasmonic metamaterials, J. Opt. A: Pure Appl. Opt. 7, S97-S101, (2005).

[9] A. Alù, N. Engheta, Optical Wave Interaction with Two-Dimensional Arrays of Plasmonic Nanoparticles, in: A. A. Maradudin (Ed.), Structured Surfaces as Optical Metamaterials, Cambridge University Press, in press.

[10] A. J. Viitanen, I. Hanninen, S. A. Tretyakov, Analytical model for regular dense arrays of planar dipole scatterers, Prog. in Electromagn. Res. 38, 97-110, (2002).

[11] J. A. Gordon, C.L. Holloway, A. Deinstfrey, A physical explanation of angle-independent reflection and transmission properties of metafilms/metasurfaces, IEEE Antennas Wireless Propag. Lett., 8, 1127-1130, (2009).

[12] R. E. Collin, Field Theory of Guided Waves, second ed., Wiley-IEEE Press, New York, 1990.

[13] CST Microwave Studio^{TM} 2010, CST of America, Inc.

[14] P. B. Johnson, R. W. Christy, Optical constants of the noble metals, Phys. Rev. B 6, 4370-4379, (1972).

[15] C. R. Simovski, Analytical modelling of double-negative composites, Metamaterials 2, 169-185, (2008).

[16] D. R. Smith, Analytic expressions for the constitutive parameters of magnetoelectric metamaterials, Phys. Rev. E 81, 036605, (2010).

Chapter 6: Design Single Plasmonic Metasurfaces to Manipulate Light Polarization

From the theoretical analysis in Chapter 4 and 5, we understand that a single metasurface cannot differentiate different the handedness of circularly polarization at normal incidence, whereas it doesn't prevent us from *generating* circular polarizations using such a thin metasurfaces, since it is mainly attributed to the phase effect. In this chapter, we present an example to design a circular polarization converter: an ultrathin quarter-wave plate based on plasmonic metasurfaces. After exploring the theoretical possibilities offered by thin surfaces to manipulate the impinging polarization, we present here optimal designs to realize quarter-wave metasurface plates, analyzing their frequency and angular response. The designs we discussed here may provide large degree of linear polarization output for circularly polarized input over a broad bandwidth in the optical regime and vice versa. Although not the ultimate goal of differentiating (filtering) circular polarizations, which will be discussed in the next chapters, the geometry we presented in this chapter also have the advantages to be implemented within currently available lithographic techniques and can be easily integrated with other optical devices for polarization manipulation, detection and sensing at the nanoscale.

6.1 Introduction

Currently, circular polarizers and sensors may be realized using anisotropic or chiral devices [1], but with specific thickness limitations and quite bulky configurations. Integrating these polarizers within an ultrathin device may be of great interest in order to combine circular polarization information with nanophotonic devices and advanced sensors [2]. In this regard, recent progress in plasmonics can provide unprecedented opportunities to manipulate light polarization at the nanoscale, by exploiting the strong

field localization and enhancement due to the localized light interaction with surface plasmons [3]. Recent results have shown that crossed resonant plasmonic nanoantennas [4]-[5], corrugated elliptical gratings [7], patterned metallic films [8]-[9], planar chiral structures [11]-[12] and three-dimensional metamaterials [13] may indeed provide strong manipulation of polarization, with clear advances over currently available technology in terms of required thickness and/or bandwidth of operation.

In this chapter, we analyze in detail the potentials of plasmonic metasurfaces to manipulate the light polarization state and we discuss the specific design and optimization of ultrathin quarter-wave plasmonic plates. We propose two complementary designs based on orthogonally patterned nanorods and a specifically tailored form of anisotropy that introduces a phase shift of $\pi/2$ between two orthogonal polarizations at the operating wavelength. This concept is realized by detuning the resonance of each nanorod by slightly varying the individual aspect ratio, in a fashion similar to what proposed in recent papers [5]-[6],[9]. Since the phase of the scattered fields sharply varies with frequency around the nanorod resonance, it is possible to tailor the phase shift between the scattered waves of two orthogonal nanorods by slightly changing their relative length around the resonant one. We analyze with full-wave simulations the overall angular and bandwidth performance of arrays of such inclusions, highlighting their optimal performance properties and their advantages in terms of lithographic realization and integration with sensors and other related technology. In the following, we present an extensive analysis of the physical mechanism behind this operation and perspectives on its potential application for practical quarter-wave plates.

6.2 THEORETICAL FORMULATION

Consider the ultrathin, arbitrary planar metasurface with sub-wavelength thickness $d << \lambda_0$ placed on the plane $z = 0$, a similar configuration that we first analyzed in Chapter 4. We can define the general transmission matrix $\underline{\mathbf{T}}$, describing the complex amplitudes of transmitted waves

$$\underline{\mathbf{T}} = \begin{pmatrix} T_{xx} & T_{xy} \\ T_{yx} & T_{yy} \end{pmatrix}, \tag{6.1}$$

where the arbitrary element T_{lm} represents the complex amplitude of the transmitted wave, linearly polarized in the m direction for excitation in the l direction. We assume an $e^{-i\omega t}$ time-harmonic dependence and for simplicity we focus in (6.1) on normal incidence illumination.

For a metasurface period smaller than the wavelength so that only the zero-th diffraction order can propagate away from the xy plane, we can describe the metasurface with its average surface admittance $\underline{\mathbf{Y}}_\mathbf{s} = Y_{xx}\hat{\mathbf{x}}\hat{\mathbf{x}} + Y_{xy}\hat{\mathbf{x}}\hat{\mathbf{y}} + Y_{yx}\hat{\mathbf{y}}\hat{\mathbf{x}} + Y_{yy}\hat{\mathbf{y}}\hat{\mathbf{y}}$, which relates the averaged electric field to the induced electric polarization current density $\mathbf{J}_{av} = \underline{\mathbf{Y}}_\mathbf{s} \cdot \mathbf{E}_{av}$. We can neglect magnetic effects for excitation at normal incidence, since the metasurface has negligible thickness [13]-[18]. By matching the boundary conditions on the metasurface, it is possible to relate the surface admittance tensor to $\underline{\mathbf{T}}$, as we have shown in Chapter 5, Eq. (5.7) [15],[18]:

$$\underline{\mathbf{Y}}_s = -\frac{2}{\eta_0}\begin{pmatrix} 1+\dfrac{T_{yy}}{\left(T_{xy}T_{yx} - T_{xx}T_{yy}\right)} & \dfrac{-T_{xy}}{\left(T_{xy}T_{yx} - T_{xx}T_{yy}\right)} \\ \dfrac{-T_{yx}}{\left(T_{xy}T_{yx} - T_{xx}T_{yy}\right)} & 1+\dfrac{T_{xx}}{\left(T_{xy}T_{yx} - T_{xx}T_{yy}\right)} \end{pmatrix}. \tag{6.2}$$

Equation (6.2) relates the surface admittance to its transmission properties, allowing its design for the specific functionality of interest. The admittance can be used

as a building block in a more complex nanocircuit [18]-[20] or to tailor and manipulate the impinging signal. Here we explore the fundamental limits in manipulating the polarization state of impinging light, with special interest to circular polarization.

In the most general case, the transmission matrix (6.1) may be written in a circularly polarized base:

$$\underline{\mathbf{T}}_{CP} = \begin{pmatrix} T_{LL} & T_{LR} \\ T_{RL} & T_{RR} \end{pmatrix} = \begin{pmatrix} \dfrac{T_{xx} + T_{yy} + i\left(T_{xy} - T_{yx}\right)}{2} & \dfrac{T_{xx} - T_{yy} - i\left(T_{xy} + T_{yx}\right)}{2} \\ \dfrac{T_{xx} - T_{yy} + i\left(T_{xy} + T_{yx}\right)}{2} & \dfrac{T_{xx} + T_{yy} - i\left(T_{xy} - T_{yx}\right)}{2} \end{pmatrix}, \quad (6.3)$$

where, similar to the notation in (6.1), T_{LR} denotes the transmission coefficient for left-handed circularly polarized (LCP) waves for right-handed (RCP) illumination, and similarly for all the other elements. Using (6.2), we can write $\underline{\mathbf{T}}_{CP}$ in terms of the surface admittance and it is easy to verify that $\left|T_{LL}\right| = \left|T_{RR}\right|$ for any lossless metasurface made of reciprocal materials, as $T_{xy} = T_{yx}$ for normal incidence. By introducing absorption it may be possible to relax this constraint and introduce small circular dichroism that may distinguish between the two circular polarizations [21], but this phenomenon has limited bandwidth and practical application. Similarly, by exciting at oblique incidence, we may be able to introduce an effective nonreciprocal response, associated with the inclusion bianisotropy [22]-[23]. It may be shown, in fact, that a possible inclusion asymmetry may produce a magneto-electric coupling effect that allows $T_{xy} \neq T_{yx}$, introducing a difference between LCP and RCP response for a single metasurface [24]. For an ultrathin surface, however, this effect may be obtained only for oblique incidence, which effectively breaks the 2D symmetry of an ultrathin surface. Usually these effects are weak and difficultly exploited in a practical configuration due to their narrow bandwidth. For these reasons, we focus in the following on manipulating the

phase difference between T_{LL} and T_{RR}, rather than their amplitude, to effectively realize ultrathin quarter-wave plates, similar to a birefringent crystal but over a negligible thickness. This operation may be obtained without cross-coupling terms in $\underline{\mathbf{T}}$, i.e., for $T_{xy} = T_{yx} = 0$ in a suitably chosen reference system.

A birefringent crystal manipulates the state of polarization by introducing a phase delay of one linearly polarized component of the impinging field over the other. At the exit of the crystal, if the cumulative phase difference is exactly 90 degrees, LCP/RCP inputs will result in linear orthogonal polarizations. We aim at designing a metasurface operating in the same way, but over a single ultrathin surface. The required transmission matrix

$$\underline{\mathbf{T}} = \begin{pmatrix} \tau & 0 \\ 0 & \pm i\tau \end{pmatrix}$$

may be obtained with a surface admittance tensor (6.2)

$$\underline{\mathbf{Y}}_s = \begin{pmatrix} \frac{2}{\eta_0}\frac{1-\tau}{\tau} & 0 \\ 0 & \frac{2}{\eta_0}\frac{\mp i-\tau}{\tau} \end{pmatrix}, \tag{6.4}$$

where τ is a complex quantity $\tau = re^{i\theta}$.

In the limit of small absorption, the real part of the diagonal elements in (6.4) is zero, which may be obtained only when $\theta = \mp\frac{\pi}{4}$ and $r = \frac{\sqrt{2}}{2}$, i.e.:

$$\underline{\mathbf{Y}}_s = \frac{2}{\eta_0}\begin{pmatrix} \pm i & 0 \\ 0 & \mp i \end{pmatrix}, \tag{6.5}$$

and the corresponding transmission matrix coincides with the Jones matrix of a lossless quarter-wave plate. We also notice that the continuity of the electric and magnetic fields on an ideally thin metasurface require that the reflection matrix satisfies

$\underline{\mathbf{R}} = \underline{\mathbf{T}} - \underline{\mathbf{I}} = -\underline{\mathbf{T}}^T$, where $\underline{\mathbf{I}}$ is the identity matrix and the superscript T indicates the transpose operation [25]. This implies that, when Eq. (6.5) is satisfied, the metasurface reflection matrix also satisfies similar quarter-wave plate conditions and the total transmitted power is half of the impinging one. This will be particularly relevant in the next section, when we consider complementary plasmonic metasurfaces. In the following, we aim at realizing a plasmonic metasurface with admittance tensor given by (6.5), which realizes a transmission matrix equivalent to a lossless quarter-wave plate, but in an ultrathin geometry.

6.3 PLASMONIC METASURFACE DESIGN

The ideal quarter-wave plate response (6.5) may be obtained by considering a metasurface with two orthogonal symmetry axes. Nanocrosses have been proposed to locally convert linear to circular polarization [4] and arrays of orthogonal nanoslits have been recently suggested to realize ultrathin wave-plates [5]. We explore in this context plasmonic inclusions to realize the optimal local impedance response (6.5) using orthogonal arrays of nanorods or nanoslits, slightly off resonance. An ideal lossless metasurface made of nanoslits in a plasmonic thin screen provides identically zero reflection and total transmission at resonance, with a transmission phase that rapidly switches from 90 to 270 degrees around this resonance. If we interleave two arrays of orthogonal nanoslits, one operating slightly above and one slightly below their resonance, as recently suggested in [5], we may achieve a precise 90 degree phase shift between the two transmitted waves. We aim here at tuning the length of the nanoslits to satisfy as closely as possible Eq. (6.5), both in amplitude and phase at the design wavelength $\lambda_0 = 650\,nm$.

We have used full-wave numerical simulations based on finite-integration technique [26] to realize this optimal condition in the geometry shown in Figure 6.1 and verify its wave-plate operation. We assume in our simulations a silver permittivity following the Drude model $\varepsilon_{Ag} = \varepsilon_0 \left(\varepsilon_\infty - \frac{f_p^{\,2}}{f\left(f - i\gamma\right)} \right)$, with $\varepsilon_\infty = 5$, $f_p = 2.175\,\mathrm{PHz}$ and $\gamma = 4.35\mathrm{THz}$ [27]. Each optimized unit cell is formed by two orthogonal rectangular nanoslits with a separation gap g = 10 nm, a vertical arm length L_y = 160nm and a lateral arm length L_x = 60 nm. Both nanoslits have a width w = 20nm and the screen thickness is d = 40nm. The lattice constants are a_x = 100nm, a_y = 180nm. This configuration may be experimentally realized by evaporating a thin silver film and then apply e-beam lithography followed by reactive ion etching, or by directly writing using focused ion-beam. For now, we do not consider the presence of a substrate in our design, which may be required in its practical realization ($d_s = 0$). We will consider its effects in the following.

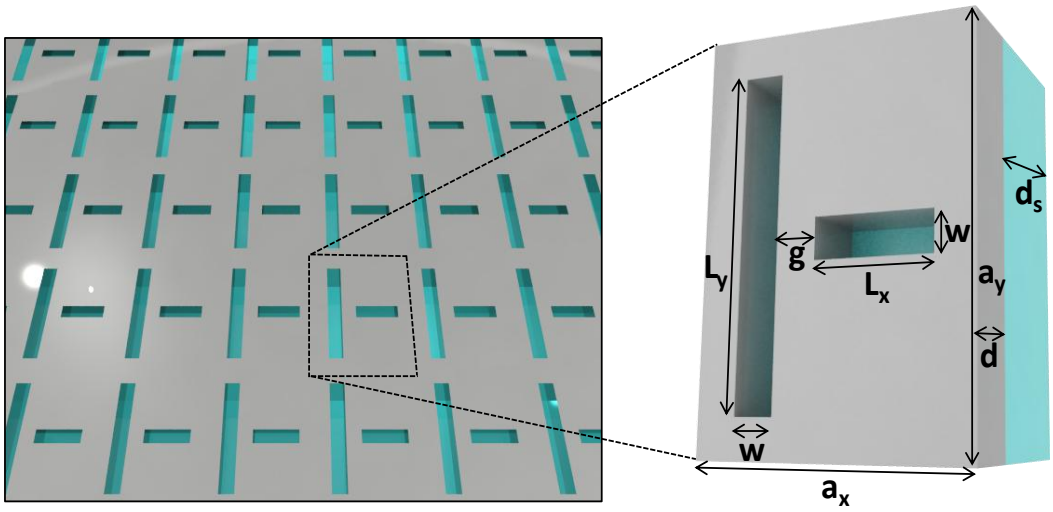

Figure 6.1: Nanoslit plasmonic metasurface, its unit cell and the corresponding geometrical parameters. (Reprinted from Phys. Rev. B 84, 205428 (2011). Copyright 2011 American Physical Society)

As shown in Figure 6.2a, this optimized metasurface shows two distinct resonances when illuminated with orthogonal linear polarizations aligned along the nanoslits. At the design wavelength, the two nonzero diagonal terms of the transmission matrix have same amplitude $|T_{xx}| = |T_{yy}| \sim \frac{\sqrt{2}}{2}$, and a phase difference (Figure 6.2b) exactly equal to 90 degrees, ensuring that its operation as an ideal ultrathin low-loss quarter-wave plate is obtained. Even though silver has some absorption in the visible, the transmission amplitudes satisfy very closely the requirements of a lossless quarter-wave plate. Indeed, we verify in Figure 6.3c that the absorption effects are minimal all over the frequency range of interest, and the transmittance and reflectance spectra are close to 50%.

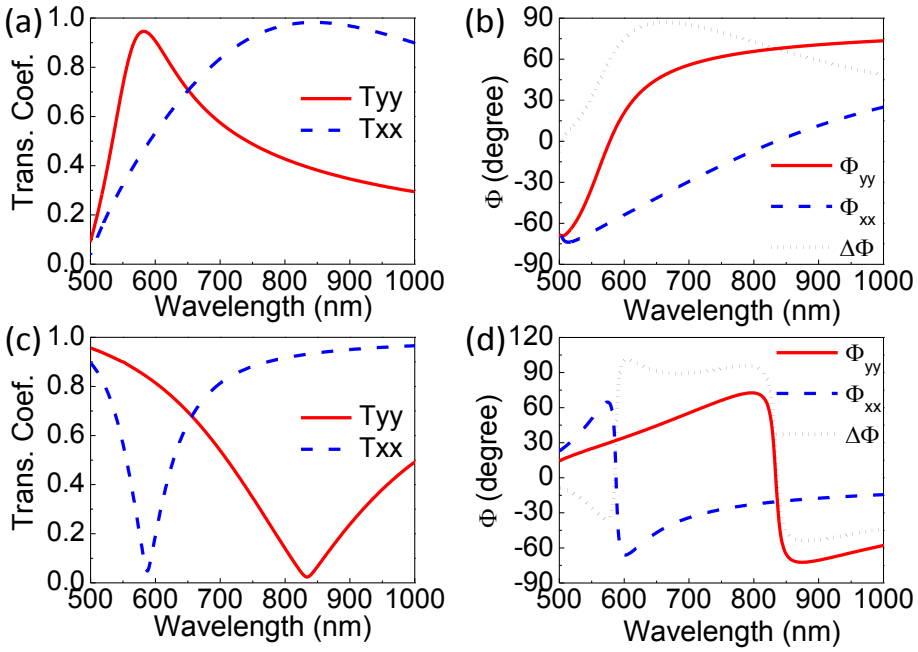

Figure 6.2: (a) Amplitude and (b) phase of the transmission coefficients for linearly polarized excitations, for the optimized metasurface geometry of Figure 6.1. (c,d) Similar plots for the complementary geometry, composed of plasmonic nanorods. (Reprinted from Phys. Rev. B 84, 205428 (2011). Copyright 2011 American Physical Society)

As noticed above, we may also consider the complementary geometry formed by interleaved arrays of plasmonic nanorods. Applying Babinet's principle [28] properly extended to plasmonic screens [29]-[30], we expect that the transmission properties of a complementary array of silver nanorods with same design parameters as in Figure 6.2 may be approximately equal to the reflection matrix of the nanoslit array $\mathbf{R} = -\mathbf{T}^T$ at the design wavelength. Since also $-\mathbf{T}^T$ satisfies the ideal quarter-wave plate conditions, the complementary design may provide similar optical response. Because silver has finite conductivity, we do not achieve exact complementary response, but we have verified that by slightly modifying the design of the complementary array (L_y=140nm, L_x=65nm), we achieve the quarter-wave plate condition at the design wavelength of 650 nm. The corresponding results are shown in Figure 6.2c-d, which indeed show complementary transmission properties compared to the nanoslit geometry and identical response at the design wavelength.

Figure 6.3 shows amplitude and phase of the transmitted fields, and the total transmission, reflection, and absorption spectra for circularly polarized inputs in both designs. Panels (a), (b) and (c) refer to the nanoslit metasurface, while (d), (e) and (f) refer to the complementary nanorod metasurface. It is seen that, as predicted, $|T_{LL}| = |T_{RR}|$ at all frequencies and both metasurfaces realize the desired transmission conditions, in both amplitude and phase, around the same design wavelength. Due to frequency dispersion, the ideal quarter-wave plate conditions can be met only at a single wavelength, at the point of intersection of the transmission curves in Figure 6.2. However, when the ratio of linearly polarized components of the transmitted wave are within the range $0.8 \sim 1.2$, as shown in the shadowed region in Figure 6.3a and 6.3c, the performance as a quarter-wave plate is still acceptable. We define the wavelength range over which this condition is met the *amplitude bandwidth* of the given metasurface.

Panels (b) and (e) show the phase difference of the transmitted linearly polarized components. It is found that an acceptable range is ± 10 degrees for RCP and $170 \sim 190$ degrees for LCP, as indicated by the shadowed rgions in Figure 6.3b and 6.3d, which defines the metasurface *phase bandwidth*. The QWP bandwidth of operation of the metasurface generally coincides with the minimum between these two bandwidths but, as detailed in the following, for specific operations one of the two bandwidths may be more relevant and dominate the response.

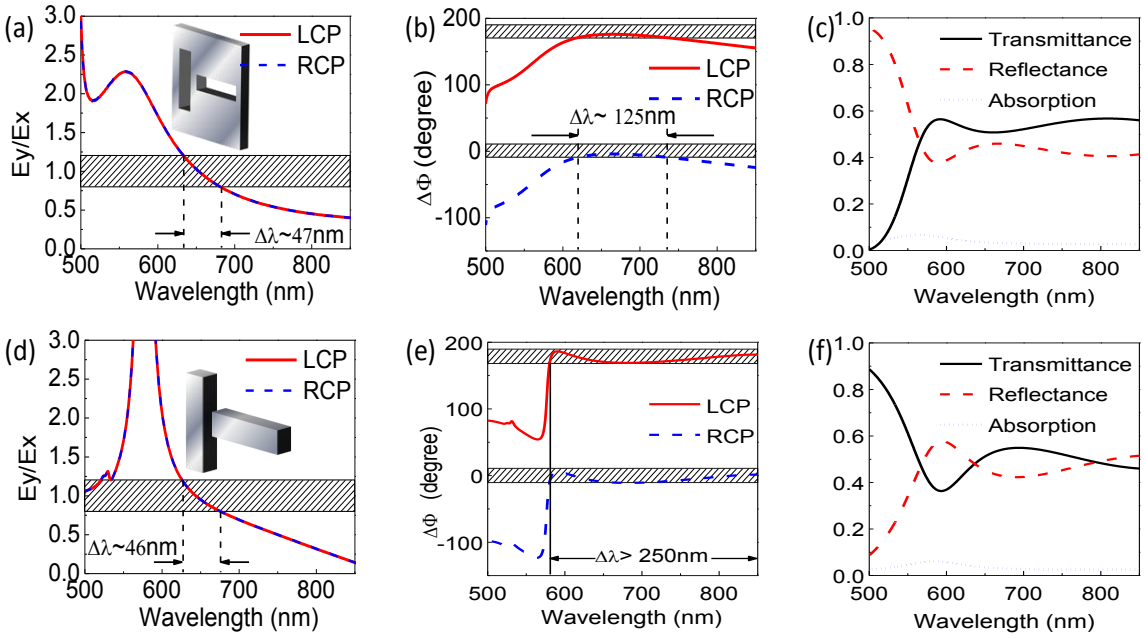

Figure 6.3: Amplitude and phase of the transmitted fields for circularly polarized excitations. (a) Amplitude ratio of transmitted E_y / E_x for LCP and RCP excitation for the nanoslit metasurface of Figure 6.1; (b) phase difference between E_y and E_x; (c) transmittance, reflection and absorption spectra for the nanoslit metasurface; (d,e,f) similar plots for the complementary nanorod metasurface. (Reprinted from Phys. Rev. B 84, 205428 (2011). Copyright 2011 American Physical Society)

A good figure of merit to analyze the performance of these metasurfaces, in particular for integration with polarization imaging sensors, is represented by their degree of linear polarizaiton (DoLP), defined as $DoLP = \frac{\sqrt{S_1^2 + S_2^2}}{S_0}$, with S_0, S_1, S_2 being the Stokes parameters. This quantity effectively represents how linearly polarized is the transmitted wave for circularly polarized inputs. In this case, the *phase bandwidth* is evidently more relevant, since we are not concerned about the specific direction of linear polarization output.

Figure 6.4 shows the DoLP of both the nanoslit and nanorod metasurfaces. The bandwdith over which the DoLP is nearly unity closely corresponds to the phase bandwdith shown in Figure 6.3, which is significantly broad considered the ultrathin features of the device. We have also calculated the angle of polarization of the transmitted wave within the bandwidth in which DoLP is near unity, as shown in panels (a) and (b). At the design frequency, as expected, both designs provide linear polarization at 45 degrees, but this angle changes within the bandwidth of operation, due to the dispersion of $|T_{xx}|/|T_{yy}|$. For the nanoslit metasurface, we obtain linearly polarized transnmission at an angle ranging from 28° to 55° with respect to the x axis within the bandwidth of interest (616 to 746 nm); with the nanorod metasurface the angle of linear polarization (AoLP) varies from 1° to 86°, within the broader range 573-934nm. The nanorod metasurface ensures a broader phase bandwidth, and a correspondingly larger range over which the DoLP is unity, which spans almost the entire visible. Using the reciprocity theorem, we expect to obtain circularly polarized output with linearly polarized input at the AoLP indicated in Figure 6.4(a) and (b). For this dual operation, the amplitude bandwidth is relevant, since the fast- and slow-axes of the quarter-wave plate

metasurface effectively rotate with the wavelength of operation and are not necessarily aligned with the rods or slits.

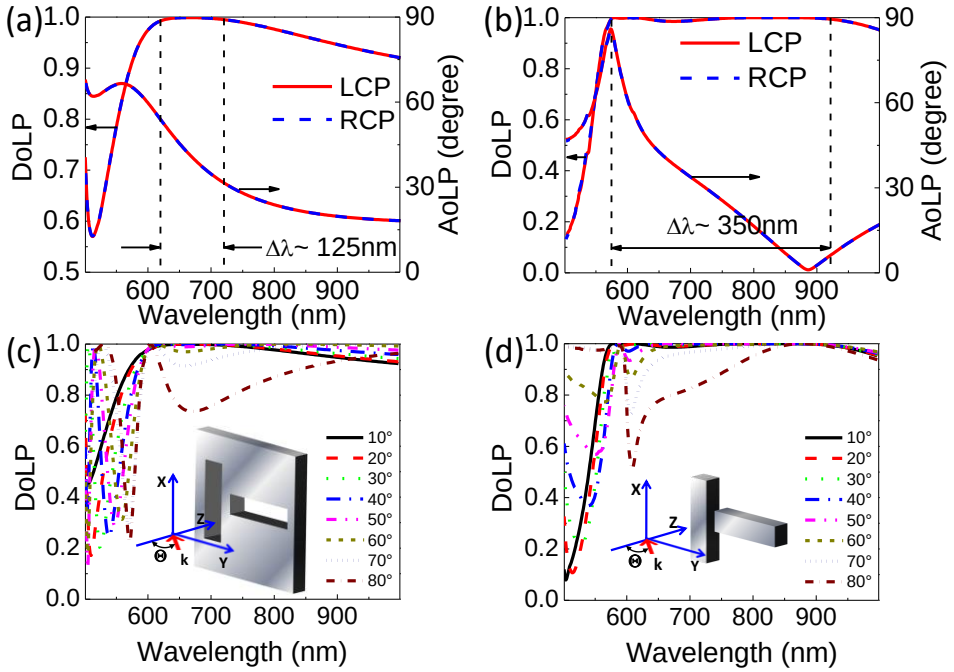

Figure 6.4: Degree of linear polarization for (a) nanoslit and (b) nanorod metasurfaces for RCP and LCP excitation, (c,d) similar plots for oblique incidence and RCP excitation. (a,b) show also the corresponding angle of linear polarization. (Reprinted from Phys. Rev. B 84, 205428 (2011). Copyright 2011 American Physical Society)

An additional relevant aspect to consider for these ultrathin designs is their robustness to variations in incidence angle, as we investigate in Figs. 6.4(c) and 6.4(d). In particular, we show the DoLP for incidence angles varying from 10° to 80° for both nanoslit and nanorod metasurfaces, when RCP light impinges on the surface. For incidence angles up to 40°, a relatively large bandwidth with unity DoLP is obtained; as the incidence angle increases further, the bandwidth of operation decreases due to the

occurrence of resonance dips caused by the coupling with long-range surface plasmons [31].

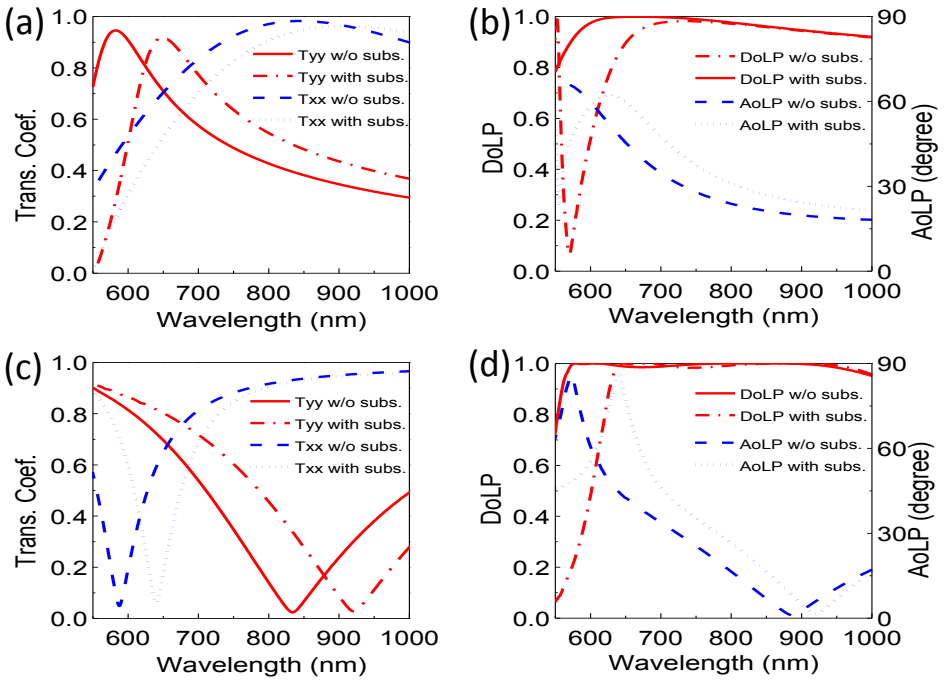

Figure 6.5: Comparison of: (a) transmission coefficients and (b) DoLP for the metasurfaces made of slit inclusions, with and without the presence of a substrate; (c,d) same for dipole inclusions. (Reprinted from Phys. Rev. B 84, 205428 (2011). Copyright 2011 American Physical Society)

In reality, a supporting substrate needs to be taken into account for the practical realization of these devices. By adding a non-dispersive silicon dioxide substrate, with relative permittivity 2.25, the inclusion resonance is shifted to longer wavelengths [32], so the optimal design needs to take into account its influence. In Figure 6.5 we show how the previous results are affected by such a glass substrate, by keeping the design unchanged. First, it is observed that the quarter-wave plate operation is shifted to the longer wavelength of 704nm. In addition, the functionality is no longer ideal, since the

phase relation among the two orthogonal linearly polarized transmitted waves is slightly changed, as the two transmission curves intersect with a phase difference of 83° instead of 90°. Still, the performance in terms of DoLP and AoLP is pretty robust. Obviously, a new design considering the substrate presence may further improve the overall functionality.

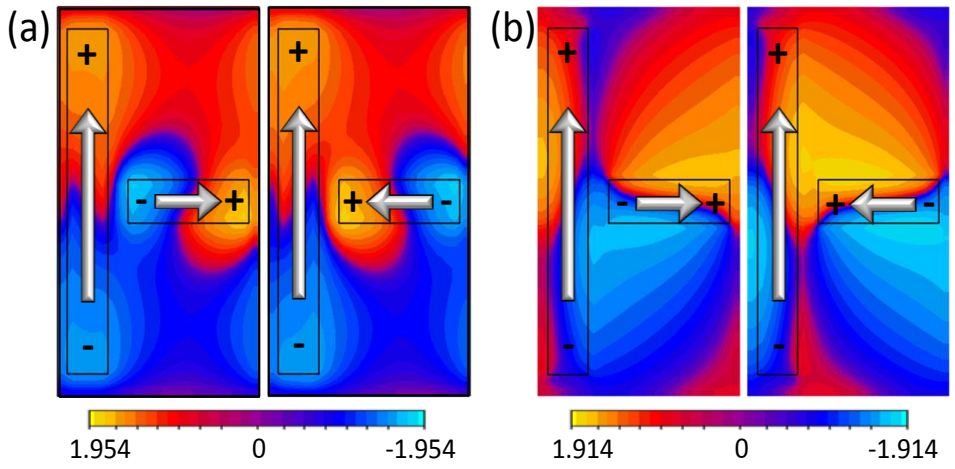

Figure 6.6: Normalized normal component of the magnetic field distribution (snapshot in time) at the metasurface output for: (a) nanoslit, (b) nanorod metasurfaces. In both cases, the input is LCP (left) and RCP (right) and the magnetic field is normalized to the impinging amplitude. (Reprinted from Phys. Rev. B 84, 205428 (2011). Copyright 2011 American Physical Society)

Finally, Figure 6.6 shows the distribution of the normal component of the magnetic field distribution (snapshot in time, normalized to the impinging transverse field) at the design frequency at the output of the two considered metasurfaces (a, nanoslit; b, nanorod) for circularly polarized excitation at normal incidence. The two plots in each panel correspond to LCP (left) and RCP (right) inputs. It is seen how the two excitations provide similar phase distribution around the inclusions, indicating typically dipolar polarizations for both orthogonal elements, respectively in phase and out

of phase with each other, depending on the circularly polarized input. We have sketched in the figure the dipolar response of each rod, which confirms the nanoscale physical mechanism behind the operation as an ultrathin quarter-wave plate. Indeed, for a circular polarization input, which is formed by two linear polarizations 90 degrees out of phase, the metausrface inclusions are polarized in phase, ensuring linearly polarized transmitted and reflected fields. On purpose, we show here the *normal* component of the magnetic fields, which allows isolating the metasurface response without interference with the purely tangential excitation fields.

6.4 CONCLUSIONS

We have investigated in this chapter the functionality and design of plasmonic metasurfaces formed by orthogonal elongated nanorods and complementary nanoslits to realize ultrathin quarter-wave plates. Based on a simple impedance model to describe the array interaction, we have achieved polarization control of the impinging light and optimized its bandwidth of operation. Our full wave simulations confirm the expected response and show a rather robust performance in terms of incidence angle and bandwidth of operation. Practical integration of these designs within optical sensors and cameras will be explored in the near-future to realize polarizers and sensors for circularly polarized light.

6.5 REFERENCES

[1] Y. H. Huang, Y. Zhou, and S. T. Wu, Opt. Express 15, 6414 (2007).

[2] V. Gruev, R. Perkins, and T. York, Opt. Express 18, 19087 (2010).

[3] N. Yu, P. Genevet, M. A. Kats, F. Aieta, J. P. Tetienne, F. Capasso, Z. Gaburro, *Science* in press, (2011).

[4] P. Biagioni, J. S. Huang, L. Duo, M. Finazzi, and B. Hecht, Phys. Rev. Lett. 102, 256801 (2009).

[5] E. H. Khoo, E. P. Li, and K. B. Crozier, Opt. Lett. 36, 2498(2011).

[6] A. Pors, M. G. Nielsen, G. Della Valle, M. Willatzen, O. Albrektsen, and S. I. Bozhevolnyi, Opt. Lett. 36, 1626 (2011).

[7] Drezet, C. Genet, and T. W. Ebbesen, Phys. Rev. Lett. 101, 043902 (2008).

[8] T. Li, H. Liu, S. M. Wang, X. G. Yin, F. M. Wang, S. N. Zhu, and X. A. Zhang, Appl. Phys. Lett. 93, 021110 (2008).

[9] F. I. Baida, M. Boutria, R. Oussaid, and D. Van Labeke, Phys. Rev. B 84, 035107 (2011).

[10] S.-Y. Hsu, K.-L. Lee, E.-H. Lin, M.-C. Lee, and P.-K. Wei, Appl. Phys. Lett. 95, 013105 (2009).

[11] Bai, Y. Svirko, J. Turunen, and T. Vallius, Phys. Rev. A 76, 023811 (2007).

[12] W.-X. Huang, Y. Zhang, X.-M. Tang, L.-S. Cai, J.-W. Zhao, L. Zhou, Q.-J. Wang, C.-P. Huang, and Y.-Y. Zhu, Opt. Lett. 36, 3359 (2011).

[13] J. K. Gansel, M. Thiel, M. S. Rill, M. Decker, K. Bade, V. Saile, G. von Freymann, S. Linden, and M. Wegener, Science 325, 1513 (2009).

[14] A. Alù and N. Engheta, in *Structured Surfaces as Optical Metamaterials*, edited by A. A. Maradudin (Cambridge University Press, 2011).

[15] M. Beruete, M. Sorolla, R. Marques, J. D. Baena, and M. Freire, Electromagnetics 26, 247 (2006).

[16] L. Holloway, M. A. Mohamed, E. F. Kuester, and A. Dienstfrey, IEEE Trans. Electromagn. Compat. 47, 853 (2005).

[17] A. Luukkonen, C. Simovski, G. Granet, G. Goussetis, D. Lioubtchenko, A. V. Raisanen, and S. A. Tretyakov, IEEE Trans. Antennas Propag. 56, 1624 (2008).

[18] Y. Zhao, N. Engheta, and A. Alù, Metamaterials, Special Issue for Metamaterials'2010, in press (2011).

[19] A. Alù, A. Salandrino, and N. Engheta, J. Opt. Soc. Am. B 24, 3014 (2007).

[20] N. Engheta, A. Salandrino, and A. Alù, Phys. Rev. Lett. 95 (2005).

[21] F. Bohren and D. R. Huffman, *Absorption and scattering of light by small particles* (John Wiley & Sons, New York, 1983).

[22] P. A. Belov, S. I. Maslovski, K. R. Simovski and S. A. Tretyakov, Technical Phys. Lett. 29, 718 (2003).

[23] R. Marques, F. Mesa, J. Martel and F. Medina, IEEE Trans. on Antennas and Propagation 51, 2572 (2003).

[24] Plum, X.-X. Liu, V. A. Fedotov, Y. Chen, D. P. Tsai, and N. I. Zheludev, Phys. Rev. Lett. 102, 113902 (2009)

[25] M. Born, and E. Wolf, *Principles of Optics*, 7th ed., New York: Cambridge University Press, 1999.

[26] CST Microwave Studio 2010, CST of America, Inc., www.cst.com

[27] P. B. Johnson and R. W. Christy, Phys. Rev. B 6, 4370 (1972).

[28] Falcone, T. Lopetegi, M. A. G. Laso, J. D. Baena, J. Bonache, M. Beruete, R. Marqués, F. Martín, and M. Sorolla, Phys. Rev. Lett. 93, 197401 (2004).

[29] C. Rockstuhl, T. Zentgraf, T. P. Meyrath, H. Giessen, and F. Lederer, Opt. Express 16, 2080 (2008).

[30] T. Zentgraf, T. P. Meyrath, A. Seidel, S. Kaiser, H. Giessen, C. Rockstuhl, and F. Lederer, Phys. Rev. B 76, 033407 (2007).

[31] Raether, Surface plasmons on smooth and rough surfaces and on gratings (Springer, Berlin, 1988).

[32] D. H. Dawes, R. C. McPhedran, and L. B. Whitbourn, Appl. Optics 28, 3498 (1989).

Chapter 7: Experimental Realization of Broadband Optical Meta-Waveplates Based on Single Metasurface

In the previous chapter, we discussed the design of a circular polarization converter based on an ultrathin metasurface: a plasmonic meta-waveplate, which could generate circularly polarized lights with linearly polarized impinging waves. One common issue hindering the extension of quarter wave plate phenomenon to broadband operations is the fact that the response of optical metasurfaces is inherently narrowband and mechanisms to increase their bandwidth often clash with causality and passivity constraints of materials. In this chapter, we are able to experimentally demonstrate that broadband, strong polarization conversion and quarter-wave plate functionality may be achieved using a single, ultrathin planar metasurface in the visible regime. The realized device is based on the design proposed in the previous chapter: interleaved silver nanorods with properly tailored frequency dispersion, which introduces an abrupt flat $90°$ phase shift for orthogonal polarizations over a thickness of few tens of nanometers, achieving achromatic quarter-wave plate behavior covering a good portion of the visible spectrum. Analogous design principles are extended to cover the entire visible spectrum and beyond.

7.1 Introduction

Conventional circular polarization is obtained by stacking a linear polarizer with bulky quarter-wave plates made by birefringent materials. This configuration cannot be easily integrated in a nanophotonic system, and it is inherently narrow bandwidth, as conventional quarter-wave plates rely on wavelength-dependent dispersion of the birefringence phenomenon. For this reason, metamaterials have been recently explored and proposed to realize quarter-wave plates and circular polarizers in compact, planarized

and easily integrated designs [5]-[11]. Especially interesting in this context are plasmonic metasurfaces [12]-[18], which are able to induce strong electron-photon interaction within a thickness of few nanometers, as proposed by several groups both theoretically and experimentally [5]-[11],[19]-[21]. As in the case of metamaterials, their extreme thickness and subwavelength resonant effects limit their functionality to a narrow bandwidth, with evident constraints on their impact and applicability in realistic optical systems. Broadband circular polarization conversion has been recently realized in 3D optical metamaterials [12],[22] using helical or twisted arrangements of resonant inclusions. In a very recent study [23], broadband polarization conversion was realized over a much reduced thickness in the mid-IR region. This effect relies on the cross-polarization properties of optical phased antenna arrays, which inherently limits the overall conversion efficiency. In addition, the output circularly polarized wave is radiated at an oblique angle, whose radiation direction may vary for different frequencies, posing limitations to its practical applicability. In the following, we show that broadband quarter-wave plate operation at normal incidence with large conversion efficiency based on the dominant diffraction order can be achieved using a single, ultrathin patterned plasmonic surface, only few nanometers thick, by properly tailoring the frequency dispersion of closely spaced silver nanorods operated off resonance.

Waveplate functionality may be obtained over a thin surface by introducing an abrupt jump in the phase of transmitted light, tailored to be a function of the impinging polarization. This may be achieved in the form of a localized birefringence using anisotropic nanoparticle arrays[5],[10],[21],[24]. A nanorod is the simplest form of anisotropic nanoparticle, as it mainly interacts with the impinging polarization parallel to its axis. When plasmonic effects are considered, resonant dipolar response may be obtained for a length significantly shorter than the excitation wavelength, which may be

further controlled by the rod thickness that modulates its surface plasmon properties. The corresponding phase of the induced dipole moment shows fast variations around this resonance wavelength, essentially flipping by up to $180°$.

7.2 DESIGN OF BROAD BAND DISPERSION

We again consider two orthogonally patterned nanorods with lengths l_x, l_y arranged in a planar rectangular array with periods d_x, d_y, as we have theoretically considered in the previous Chapter [25], and as shown schematically in the inset of Figure 7.1(a). Each nanorod interacts with the polarization parallel to the rod axis, with a wavelength response determined by the resonant dispersion of the rods and by the array interaction. Transmission may be easily related to the polarizability tensor $\underline{\underline{\boldsymbol{\alpha}}}$ of the rods and the interaction dyadic $\underline{\underline{\mathbf{C}}}_{\text{int}}$ of the array [26],[28]. The rod polarizability may be well approximated by the three-axial ellipsoid quasi-static polarizability with semi-axes $w/2$, $z/2$, and $l/2$, which provides a diagonal tensor $\underline{\underline{\boldsymbol{\alpha}}}$ with elements $\alpha_{ii} = \frac{\pi}{8} wzl \frac{\varepsilon_{Ag} - \varepsilon_m}{3\varepsilon_m + 3L_i\left(\varepsilon_{Ag} - \varepsilon_m\right)}$, $i = \mathbf{x}, \mathbf{y}, \mathbf{z}$, where L_i is the shape factor, along with the width w, the thickness z and the length l of the nanorod, and ε_{Ag}, ε_m are the permittivities of the rod and of the surrounding medium, respectively[29]. As long as the array periods are smaller than the wavelength, we can model the surface with its averaged transverse polarization current, and the corresponding transmission matrix can be calculated through the formula:

$$1.\quad \underline{\mathbf{T}} = \begin{pmatrix} T_{xx} & 0 \\ 0 & T_{yy} \end{pmatrix} = \begin{pmatrix} 1 - \frac{j\mu_0 \pi fc}{d_x d_y} \frac{\alpha_{xx}}{1 - C_{xx}\alpha_{xx}} & 0 \\ 0 & 1 - \frac{j\mu_0 \pi fc}{d_x d_y} \frac{\alpha_{yy}}{1 - C_{yy}\alpha_{yy}} \end{pmatrix}, \quad (7.1)$$

where f is the frequency of operation, c is the speed of light in vacuum, and μ_0 is the permeability of free space. The above formula allows tailoring amplitude and phase of the transmission coefficients in the two orthogonal polarizations as a function of the rod geometry and array periods[29]. Our goal is to tailor the polarizability dispersion of the nanorods to realize a flat phase difference between T_{xx} and T_{yy} over frequency.

Consider a first scenario in which the two nanorods within the unit cell have the same length $l_x = l_y = 160\,\text{nm}$, width $w = 20\,\text{nm}$ and thickness $z = 8\,\text{nm}$, with array periods $d_x = 200\,\text{nm}$ and $d_y = 170\,\text{nm}$ (inset of Figure 7.1(b)). The corresponding transmission coefficients for impinging orthogonal linear polarizations along the rods are shown in Figure 7.1(b), with two pronounced resonant dips, obtained using full wave numerical simulations. Despite the rods having the same dimensions, the different array interaction in the two polarizations produces a slight detuning of the two resonances[31]. For this specific design, at the intersection of the two transmission curves between resonant dips we meet the conditions to realize an ultrathin quarter-wave plate[25], i.e., a phase difference $\Delta\Phi = \Phi_{xx} - \Phi_{yy}$ for the transmission coefficients equal to $90°$, which is plotted over wavelength in Figure 7.1(f) (black line). This was obtained by properly tuning the rod thickness z to modify the surface plasmon propagation along the rods and induce the required phase shift. Albeit this design provides a quarter-wave plate functionality, it only covers a very narrow range of wavelengths between the array resonances. To broaden this effect, we consider detuning one of the two resonances in Figure 7.1(c), by shortening one rod to $l_x = 60\,\text{nm}$, which shifts its resonance to the visible range. By properly adjusting the thickness to $z = 45\,\text{nm}$, we are able to ensure that the phase dispersion curves (dashed lines in Figure 7.1(c)) follow each other closely in the range between the two resonances, an effect that is reflected into a flat phase

difference $\Delta\Phi$ (Figure 7.1(f), red line) around $90°$ over a broad range of wavelengths in the visible regime.

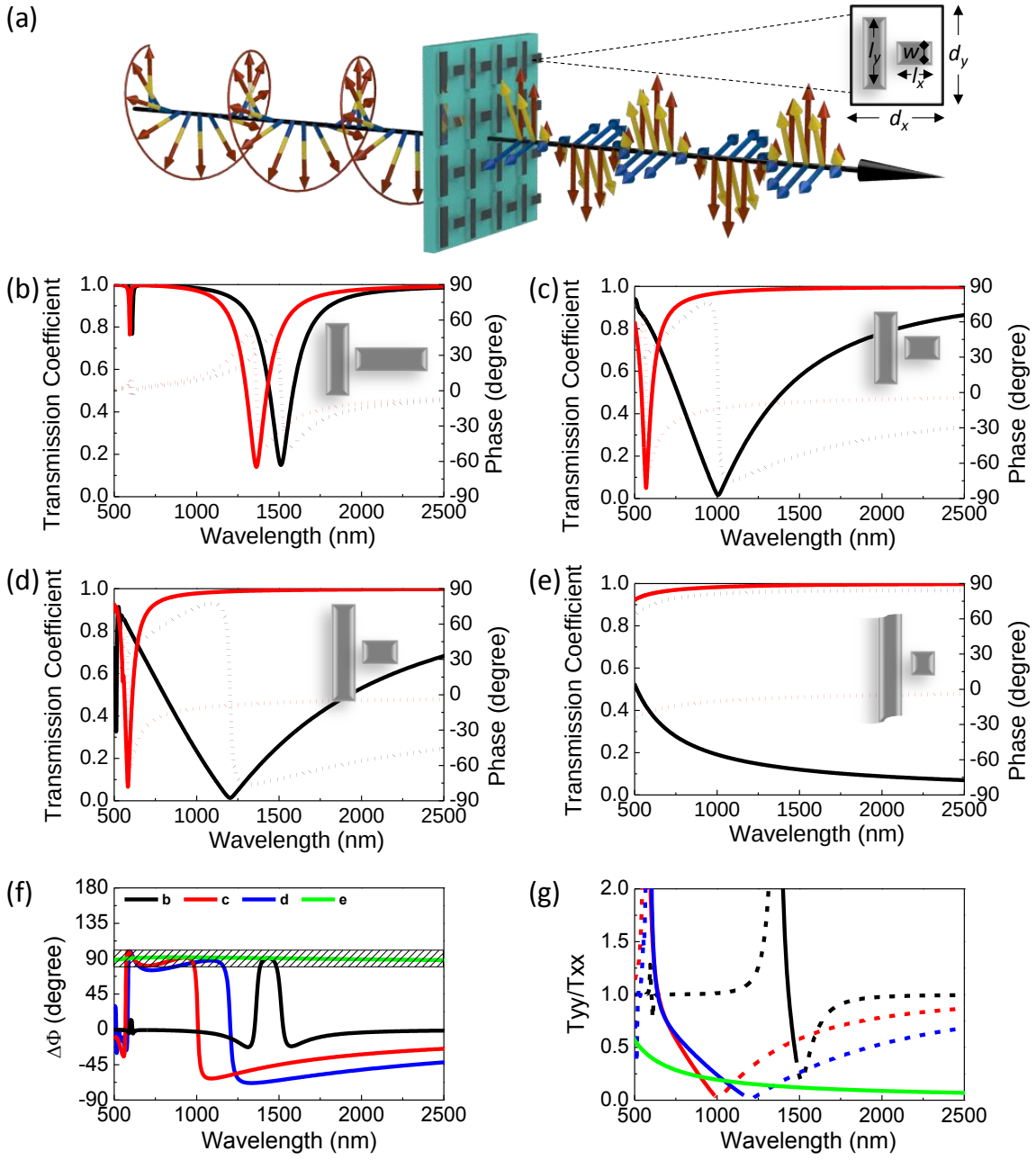

Figure 7.1: (a) Schematic illustration of the functionality of the proposed nanodevice with broadband circular excitation: the transmitted beam is linearly polarized at different angles as a function of the impinging wavelength, covering a broad spectrum. The inset shows the configuration of the unit cell. (b) Transmission coefficients for orthogonal linear polarizations: magnitude (solid curves), phase (dotted). Geometry of the metasurface: l_x=160 nm, l_y=160 nm, thickness z=8 nm, w= 20 nm, all the gaps between dipoles are kept at 10 nm. (c) Transmission coefficients for the second design, similar to (b), except that l_x=60 nm, l_y=160 nm and z=45 nm. (d) Similar to the previous panels, but with l_x=60 nm, l_y=240 nm and z=50 nm. (e) Extreme design for ultrabroad bandwidth: the vertical rods are connected into a continuous wire with width w=20nm, the horizontal rod is a square with side dimension l_x=10 nm, z=60nm. (f) Extracted phase difference between the two orthogonal linear excitations for the three designs. The shadowed area marks the acceptable phase difference that can realize a quarter-wave plate. (g) Amplitude ratio of the transmitted fields polarized along the vertical and horizontal directions. Black, red, blue and green curves correspond to the designs in panels (b), (c), (d) and (e) respectively. The solid portion of each curve corresponds to the range over which the phase difference $\Delta\Phi$ is near $90°$. (Reprinted with permission from Nano Lett., 2013, 13 (3), pp 1086–1091. Copyright 2013 American Chemical Society)

Further increasing the distance between the two resonances, by pushing l_y to $240\,\text{nm}$ and tuning $z = 50\,\text{nm}$ (Figure 7.1(d)), provides an even broader bandwidth over which the phase is around $90°$. In this case the two phase dispersion curves start slightly diverging from each other near the shorter rod resonance, which moderately affects the performance at shorter wavelengths. In spite of that, the waveplate still covers a fairly flat cumulative bandwidth of ~570nm.

To push this concept even further, we consider the final design in Figure 7.1(e), in which the vertical rods are joined, and the horizontal rods are reduced to a square with $l_x = 10\,\text{nm}$. This solution is necessary to eliminate part of the unwanted phase dispersion by effectively moving the vertical resonance to very long wavelengths. In this case, the presence of the small square nanoantenna is still necessary, since it allows interacting with the horizontal polarization and control the phase difference. Without it the elongated

wires would essentially form a linear polarizer, offering much less polarization control[32]. By controlling the coupling between the long wire and the small dipole, the phase difference $\Delta\Phi$ may be made extremely flat at $90°$ for the specific thickness $z = 60\,nm$ over a huge spectrum (Figure 7.1(f), green line), spanning the entire visible and near-IR.

It is interesting to observe how, by simply tuning the location of the two orthogonal array resonances and choosing a suitable subwavelength thickness to modify the phase dispersion of the induced surface plasmons supported by the rods, we are able to essentially create achromatic waveplate functionality over an ultrabroad wavelength range. Contrary to a conventional birefringent slab, the optimal thickness increases with larger anisotropy of the surface, a counterintuitive effect that is associated with the fact that a plasmonic nanorod resonance moves to shorter wavelengths when its thickness is reduced[33].

We notice that, within the bandwidth of operation, the ratio of transmitted amplitudes for the two orthogonal linear polarizations varies in all the proposed designs, as shown in Figure 7.1(g), due to the different amplitude dispersion of the two rods, one operated past its resonance, one before it. In this panel, the solid portion of each curve corresponds to the wavelength range of interest, over which the phase difference $\Delta\Phi$ is near $90°$. This amplitude variation reflects into a frequency dispersion of the effective fast and slow axes of the proposed waveplate[25]. For circular polarization excitation, the transmitted beam is always linearly polarized, but at an angle that depends on the wavelength of excitation (color), as schematically illustrated in Figure 7.1(a) and experimentally demonstrated in the following.

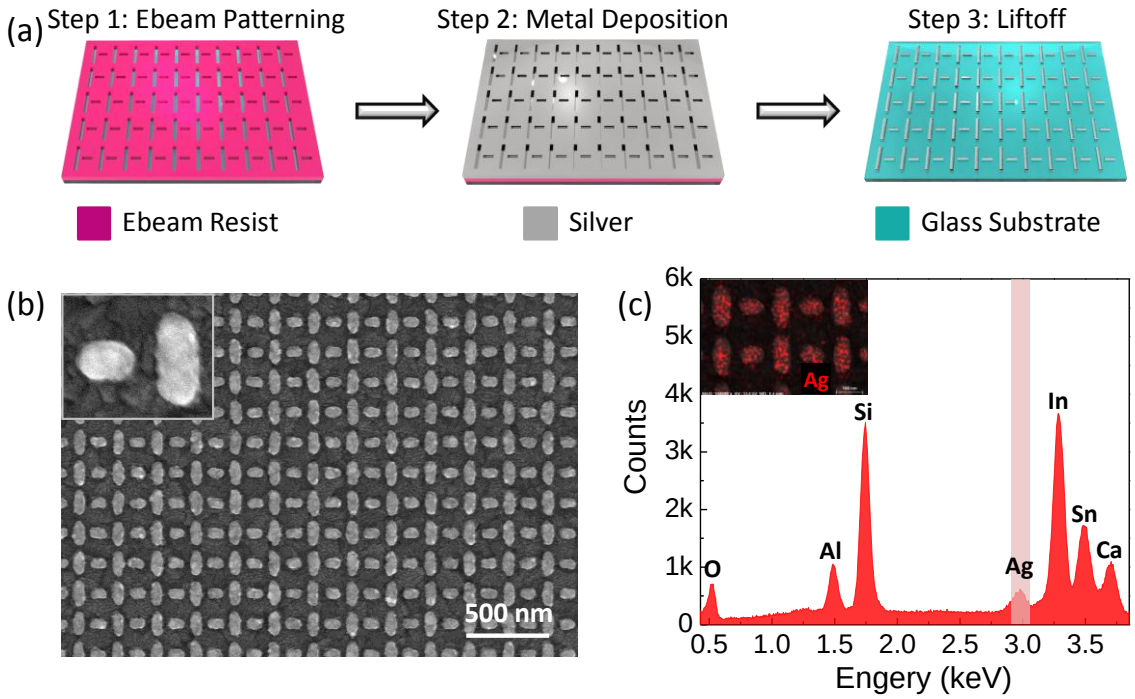

Figure 7.2: (a) Nanofabrication flow. (b) Scanning electron microscope (SEM) images of silver nanodipoles on ITO coated glass. The inset shows the dimension of the two orthogonal nanorods: $l_x = 95\,\text{nm}$, $w_x = 65\,\text{nm}$, $l_y = 150\,\text{nm}$, $w_y = 60\,\text{nm}$. (c) Energy dispersive X-ray spectrum (EDS) of the structure showing the constituent materials, where Al and Ca are dopants of the glass substrate. The inset shows the mapping of silver (red) superimposed to the SEM image. (Reprinted with permission from Nano Lett., 2013, 13 (3), pp 1086–1091. Copyright 2013 American Chemical Society)

7.3 Experimental validation of broadband quarter wave plate at the visible frequency

To test and experimentally verify the possibilities offered by this phenomenon, we have experimentally realized the design of Figure 7.1(c) by patterning orthogonal arrays of silver nanorods on a silica substrate. Due to the resolution limitation of our electron-beam lithography tools, we have slightly released the minimum dimensions of our initial design. In addition, we have taken into account the effect of the substrate, which red-shifts the resonances and reduces the phase difference $\Delta\Phi$. To counterbalance this

effect, we slightly adjusted the aspect ratio of each nanorod to optimize the bandwidth of operation.

The fabrication flow is shown in Figure 7.2(a). A one inch by one inch sized optical flat glass with 0.7mm thickness (C1737-0107, Corning low-alkaline earth from Delta Technologies) pre-coated with indium-tin oxide (ITO) was used as the substrate. Positive tone ebeam resist ZEP 520 (ZEON, Japan) was first diluted with Anisole (99%, Sigma-Aldrich), then spun onto the substrate to obtain a thickness of $100\,\text{nm}$ with less than $5\,\text{nm}$ thickness variation, characterized using spectroscopic ellipsometry (J.A. Woollam M-2000 DI Ellipsometer). The pattern was written using a JBX-6000FS/E ebeam aligner at an accelerating voltage of 50KV. After exposure, the sample was developed in Emyl Acetate (ZEON, Japan). A $2\,\text{nm}$ germanium adhesive layer and $55\,\text{nm}$ silver were sequentially deposited onto the sample using a CHA ebeam evaporator. The deposition rate of the germanium layer was precisely controlled under 0.2 Å/sec in order to minimize the thickness inhomogeneity during metallization.[34] Then, the sample underwent a liftoff process in N-methyl-2-pyroridone (Sigma-Aldrich) to complete the device fabrication.

Figure 7.2(b) shows the scanning electron microscope (SEM) image of the fabricated metasurface, which is composed of interleaved nanorods with a lateral length $l_x = 95\,\text{nm}$ and a vertical length $l_y = 150\,\text{nm}$, a horizontal width $w_x = 65\,\text{nm}$ and a vertical width $w_y = 60\,\text{nm}$. The nanorods are embedded within a $240\,\text{nm} \times 190\,\text{nm}$ rectangular lattice with inter-particle spacing of $40\,\text{nm}$. An energy dispersive x-ray spectrum (EDS) is shown in Figure 7.2(c) to reveal the constituent materials of the sample. The impurity lines in the EDS come from the ITO coated glass substrate.

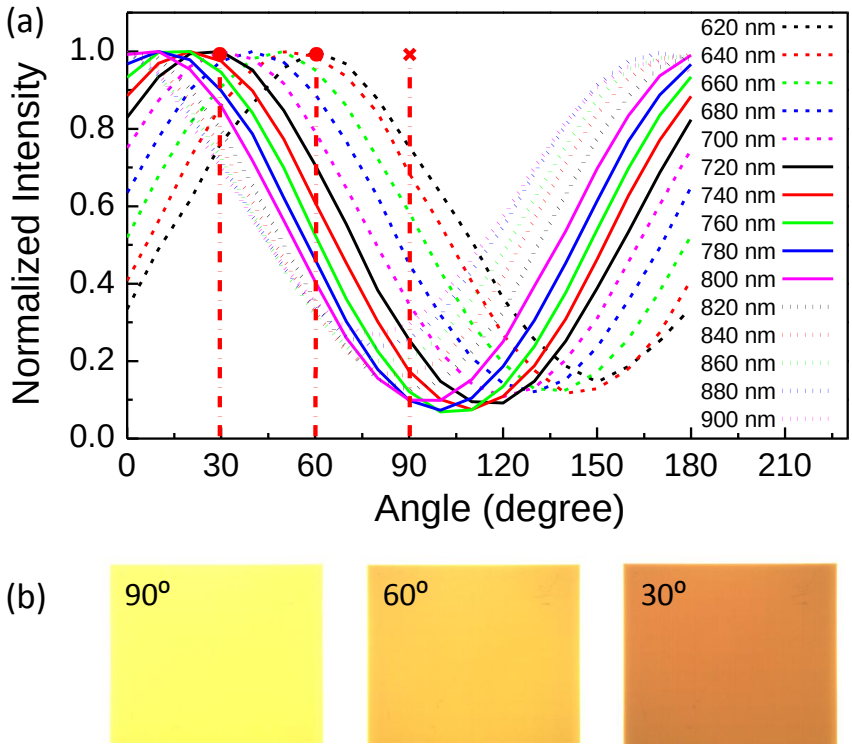

Figure 7.3: (a) Normalized amplitude measured at the output of the device for circularly polarized input by rotating a linear polarizer in front of the detector. (b) Polarizing microscope image of the device for white light illumination (field of view: $1\,\text{mm} \times 0.86\,\text{mm}$) showing color tuning for three different polarization angles in front of the detector. (Reprinted with permission from Nano Lett., 2013, 13 (3), pp 1086–1091. Copyright 2013 American Chemical Society)

We first excited the metasurface with monochromatic circularly polarized light generated using a white light source sequentially passing through a spectrometer and polarizing optics. A Halogen broadband light source was coupled through an optical fiber into the spectrometer (Princeton instrument SpectraPro-2500i), which is controlled using a Labview system to set the scan wavelength. The circular excitation was generated by passing the output light from the spectrometer sequentially through a linear polarizer (Thorlabs LPVIS050) and a broadband quarter-wave plate (Thorlabs AQWP05M-980). In order to obtain a moderate intensity at the output to meet the sensitivity of the detector

at higher frequencies, instead of a collimated beam, a slightly converging beam with a solid angle of 10 degrees was formed with a long focal length lens to focus the beam onto the sample. A second analyzer (Thorlabs LPVIS050) was used after the sample to check the angular response of the device. The final output was then fed into an InGaAs detector (Princeton instrument Model ID441-C). Wavelengths were scanned from 620 nm to 900 nm with a 20 nm interval, and the output intensity was recorded at each wavelength as a function of the polarizing angle of a second linear polarizer situated in front of the detector, and normalized as shown in Figure 7.3(a). A strong dependence of the measured intensity as a function of the linear polarization angle is achieved, confirming a large degree of linear polarization and extinction ratio over the whole bandwidth of analysis. The dips of each curve, which would ideally approach zero in our simulations from 620 nm to 830 nm, show a residual nonzero value, possibly associated with the absorption of the germanium adhesive layer, degradation due to material oxidation and/or small fabrication imperfections.

In Figure 7.3(a) we also show three vertical dash-dot lines corresponding to three specific observation angles for our second linear polarizer at 90 º, 60 º and 30 º. In Figure 7.3(b) we show the corresponding image obtained under a polarizing microscope with white light illumination. The color change by rotating the microscope polarizer reflects the wavelength of maximum transmission for the specific angle, as indicated by the dots in Figure 7.3(a), providing an interesting functionality as color filter, as proposed in a recent paper for a related plasmonic metasurface geometry[35]. Due to the low sensitivity of our detector at 580 nm, the corresponding curve for the maximum at 90 º polarization was not recorded in Figure 7.3(a) (marked as a "cross" at the end of the corresponding vertical line), but a clear yellow color is observed in the microscope image, ensuring that the polarization properties extend to the yellow range.

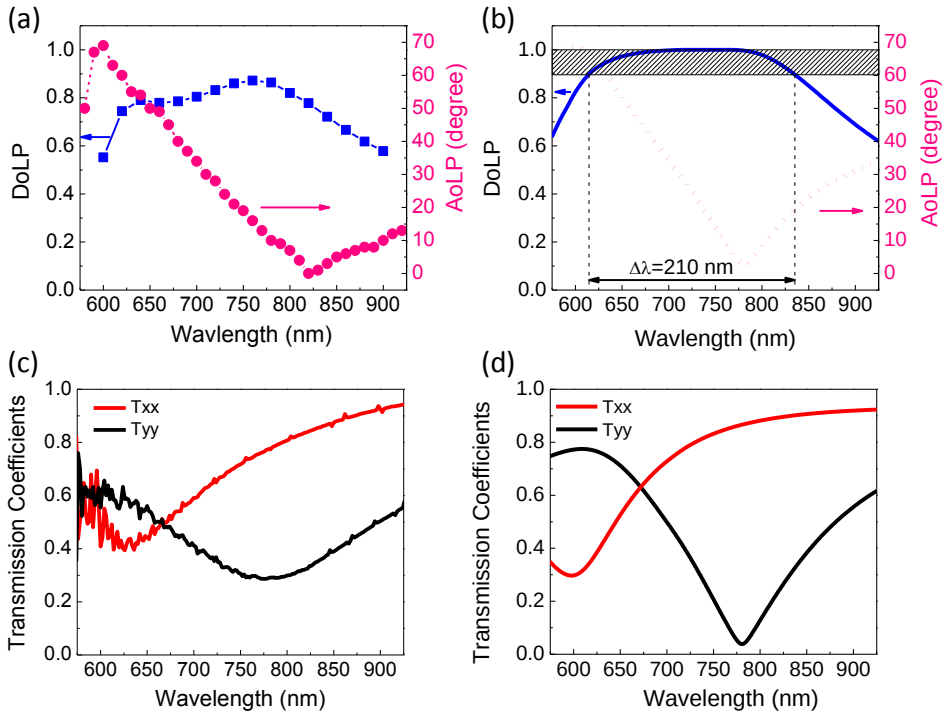

Figure 7.4: (a) Experimentally measured degree of linear polarization (DoLP) and angle linear polarization (AoLP) for circularly polarized excitation. (b) Corresponding full wave simulations for panel (a). (c) Experimental measurement of the transmission coefficients for linearly polarized excitation along the two nanorod axes. (d) Corresponding full wave simulations for panel (c). (Reprinted with permission from Nano Lett., 2013, 13 (3), pp 1086–1091. Copyright 2013 American Chemical Society)

From the measurements of Figure 7.3(a), we have extracted the overall degree of linear polarization and corresponding angle of linear polarization of our device for circular polarization excitation, shown in Figure 7.4(a). There is a broad range of wavelengths over which the degree of linear polarization is remarkably large, in good agreement with full-wave simulations (Figure 7.4(b)). Our simulations were performed by assuming nondispersive ITO ($\varepsilon_{ITO} = 2.56$) and silica ($\varepsilon_{SiO_2} = 2.1$) and a Drude model[36] for silver with $\varepsilon_{Ag} = \varepsilon_0 \left(\varepsilon_\infty - \frac{f_p^{\,2}}{f\left(f - i\gamma\right)} \right)$, $\varepsilon_\infty = 5$, $f_p = 2.175\,\mathrm{PHz}$ and $\gamma = 4.35\mathrm{THz}$. As highlighted above, the angle of linear polarization changes with

wavelength, and at $\lambda \cong 670\,\text{nm}$ it is 45°, which implies that the effective optical axes of the waveplate align with the orthogonal nanorods, achieving the functionality originally described in Ref. [25]. At this specific wavelength, the two transmission curves for linear polarization excitation intersect, as we experimentally confirmed in Figure 7.4(c) using linearly polarized excitation. The measurement was obtained by scanning the wavelength from 575 nm to 925 nm at a 2 nm resolution. Despite the detector's lower sensitivity at wavelengths shorter than 620 nm, the measured curves still agree well with our simulations (Figure 7.4(d)) and indicate that, despite some inevitable thickness inhomogeneity and material losses, which reduce the resonance strength at shorter wavelengths, the realized device provides broadband quarter-wave plate functionality over an ultrathin thickness. Compared to other recently realized devices based on V-shaped nanoantennas[20], this concept provides broader bandwidth of operation and larger coupling efficiency. Since our operation is based on the dominant diffraction order of the periodic array, we ensure a peak conversion efficiency approaching 50% over the entire wavelength of operation, which is only limited by material loss.

7.4 CONCLUSIONS

In this chapter we have shown that broadband polarization conversion and quarter-wave plate functionality may be achieved over a single ultrathin plasmonic metasurface with few tens of nanometers thickness, by tailoring the frequency dispersion of silver nanorods operated off-resonance. The proposed metasurface concept can provide broadband full control of the transmitted phase at the nanoscale, and it may be extended to different values of phase retardation, even locally varied over the surface, and span a broad spectrum in the visible, near-infrared and even THz range. These concepts may have a profound impact on novel integrated nanophotonic devices, as a

new platform for biosensing, polarization imaging, enhanced night vision devices, modulators, phase retarders, nanoantennas and nano-transmit-arrays.

7.5 REFERENCES

[1] Cronin, T. W.; Shashar, N.; Caldwell, R. L.; Marshall, J.; Cheroske, A. G.; Chiou, T. H. Integr. Comp. Biol. 43, 549-558, (2003).

[2] Lythgoe, J. N.; Hemmings, C. C. Nature 213, 893-894, (1967).

[3] Yaroslavsky, A. N.; Neel, V.; Anderson, R. R. J. Invest. Dermatol. 121, 259-266, (2003).

[4] Sparks, W. B.; Hough, J.; Germer, T. A.; Chen, F.; DasSarma, S.; DasSarma, P.; Robb, F. T.; Manset, N.; Kolokolova, L.; Reid, N.; Macchetto, F. D.; Martin, W. PNAS 106, 7816-7821, (2009).

[5] Baida, F. I.; Boutria, M.; Oussaid, R.; Van Labeke, D. Phys. Rev. B, 84, 035107, (2011).

[6] Papakostas, A.; Potts, A.; Bagnall, D. M.; Prosvirnin, S. L.; Coles, H. J.; Zheludev, N. I. Phys. Rev. Lett., 90, 107404, (2003).

[7] Biagioni, P.; Huang, J. S.; Duo, L.; Finazzi, M.; Hecht, B. Phys. Rev. Lett., 102, 256801, (2009).

[8] Khoo, E. H.; Li, E. P.; Crozier, K. B. Opt. Lett., 36, 2498-2500, (2011).

[9] Pors, A.; Nielsen, M. G.; Della Valle, G.; Willatzen, M.; Albrektsen, O.; Bozhevolnyi, S. I. Opt. Lett., 36, 1626-1628, (2011).

[10] Ogut, E.; Sendur, K. Appl. Phys. Lett., 96, 141104, (2010).

[11] Drezet, A.; Genet, C.; Ebbesen, T. W. Phys. Rev. Lett., 101, 043902, (2008).

[12] Gansel, J. K.; Thiel, M.; Rill, M. S.; Decker, M.; Bade, K.; Saile, V.; Von Freymann, G.; Linden, S.; Wegener, M. Science, 325, 1513-1515, (2009).

[13] Jen, Y.-J.; Lakhtakia, A.; Yu, C.-W.; Lin, C.-F.; Lin, M.-J.; Wang, S.-H.; Lai, J.-R. Nat. Commun., 2, 363, (2011).

[14] Shalaev, V. M. Nat. Photonics, 1, 41-48, (2007).

[15] Fedotov, V. A.; Schwanecke, A. S.; Zheludev, N. I.; Khardikov, V. V.; Prosvirnin, S. L. Nano Lett., 7, 1996-1999, (2007).

[16] Decker, M.; Ruther, M.; Kriegler, C. E.; Zhou, J.; Soukoulis, C. M.; Linden, S.; Wegener, M. Opt. Lett., 34, 2501-2503, (2009).

[17] Zhou, J.; Dong, J.; Wang, B.; Koschny, T.; Kafesaki, M.; Soukoulis, C. M. Phys. Rev. B, 79, 121104, (2009).

[18] Alù, A.; Yaghjian, A. D.; Shore, R. A.; Silveirinha, M. G. Phys. Rev. B, 84, 054305, (2011).

[19] Hsu, S.-Y.; Lee, K.-L.; Lin, E.-H.; Lee, M.-C.; Wei, P.-K. Appl. Phys. Lett., 95, 013105, (2009).

[20] Kats, M. A.; Genevet, P.; Aoust, G.; Yu, N.; Blanchard, R.; Aieta, F.; Gaburro, Z.; Capasso, F. PNAS, 109, 12364-12368, (2012).

[21] Li, T.; Liu, H.; Wang, S.-M.; Yin, X.-G.; Wang, F.-M.; Zhu, S.-N.; Zhang, X. Appl. Phys. Lett., 93, 021110, (2008).

[22] Zhao, Y.; Belkin, M. A.;Alù, A. Nat. Commun., 3, 870, (2012).

[23] Yu, N.; Aieta, F.; Genevet, P.; Kats, M. A.; Gaburro, Z.; Capasso, F. Nano Lett., ASAP, (2012).

[24] Feng, L.; Liu, Z.; Lomakin, V.; Fainman, Y. Appl. Phys. Lett., 96, 041112, (2010).

[25] Zhao, Y.; Alù, A. Phys. Rev. B, 84, 205428, (2011).

[26] Alù, A.; Engheta, N., Structured Surfaces as Optical Metamaterials. Cambridge University Press: 2011.

[27] Auguie, B.; Barnes, W. L. Phys. Rev. Lett., 101, 143902, (2008).

[28] Silveirinha, M. G. Phys. Rev. E, 73, 046612, (2006).

[29] Bohren, C. F.; Huffman, D. R., Absorption and Scattering of Light by Small Particles. John Wiley & Sons: 1998.

[30] Zhao, Y.; Alù, A.; Engheta, N. Metamaterials, 5, 90-96, (2011).

[31] Zhang, S.; Genov, D. A.; Wang, Y.; Liu, M.; Zhang, X. Phys. Rev. Lett., 101, 047401, (2008).

[32] Ekinci, Y.; Solak, H. H.; David, C; Sigg, H. Opt. Express, 14, 2323-2334, (2006).

[33] Alù, A.; Engheta, N. Phys. Rev. Lett., 101, 043901, (2008).

[34] Kobayashi, N. P.; Islam, M. S.; Wu, W.; Chaturvedi, P.; Fang, N. X.; Wang, S. Y.; Williams, R. S. Nano Lett., 9, 178-182, (2009).

[35] Ellenbogen, T.; Seo, K.; Crozier, K. B. Nano Lett., 12, 1026-1031, (2012).

[36] Johnson, P. B.; Christy, R. W. Phys. Rev. B, 6, 4370-4379, (1972).

Chapter 8: Experimental Realization of Twisted Optical Metamaterials

After designing, optimizing and realizing single element nanoantennas and densely packed 2D arrays of them, we have the confidence to march to our ultimate design of cascading metasurfaces to create a broadband circular polarization filter effect inspired by the circularly polarized visions in biological species. At this moment, we have collected all the tools both theoretically, numerically and experimentally to enable us to fulfill this aim.

The reason of using a multilayer stacked metasurface arises from the fact that optical metamaterials are usually based on planarized, complex-shaped, resonant nanoinclusions. Although 3D geometries may provide a more straightforward design in terms of the central focus of this study—the broadband chirality to manipulate circular polarization at the nanoscal—yet their fabrication becomes challenging as their critical dimensions get smaller, especially in the optical regime. In this chapter, we present the cascaded metasurface designs and experimental validation for the realization of optical metamaterials, showing that 3D effects may be obtained without complicated inclusions, but instead by tailoring the relative orientation within the lattice. Here we apply this concept to realize planarized, broadband bianisotropic metamaterials as stacked nanorod arrays with a tailored rotational twist. Due to the coupling among closely spaced twisted plasmonic metasurfaces, metamaterials realized with conventional lithography may effectively operate as 3D helical structures with broadband bianisotropic optical response. The proposed concept is also shown to relax alignment requirements common in 3D metamaterial designs. The realized sample constitutes an ultrathin, broadband circular polarizer that may be directly integrated within nanophotonic systems.

8.1 INTRODUCTION

Circular dichroism, bianisotropy and magneto-electric coupling, found in chiral molecules, are at the origin of the different optical response of natural materials to left-handed (LCP) and right-handed circularly polarized (RCP) excitations. Based on these concepts, 3D chiral structures such as helices may be used to realize circular polarizers [1],[2]. Similarly, cholesteric liquid crystals are composed of chiral molecules with a helical pitch that may be used to selectively filter one circular polarization based on Bragg reflection [3]-[6]. Conventional circular polarizers based on these concepts typically operate over narrow frequency bands[4], which may be broadened by stacking multiple polarizers or introducing a gradient in the helical pitch [3],[6]. However, modest bandwidth increases are usually achieved at the price of much bulkier devices, difficultly integrated within today's nanophotonic systems.

Recent advances in metamaterials [3],[7]-[11] have opened new routes towards integrated circular polarizers with low profile and larger bandwidths of operation. In part inspired by biological species that are well equipped with broadband, conformal circular polarization sensors [12], optical activity and circular dichroism have been shown in either planar [13]-[18] or three-dimensional metamaterials [3],[19]-[20]. Planar structures generally exhibit much weaker circular dichroism compared to three-dimensional geometries, since an infinitesimally thin device is inherently achiral, and excitation at oblique incidence or some form of nonreciprocal response is required to distinguish between LCP and RCP transmissivity [21]. In this context, the concept of extrinsic chirality has been recently put forward, showing that, by pairing two closely spaced planarized inclusions with some form of 3D chirality, may produce a narrow-band chiral response near their resonance [13]-[18] .

3D chiral metamaterials have more appealing properties as circular polarizers, but periodic arrays with subwavelength chiral features and precise alignment are challenging to realize at visible wavelengths, despite several available top-down [3] and bottom-up [19] fabrication approaches. An exciting possibility in this context is provided by direct laser writing [22],[23], which ensures large flexibility in the shape of the realizable 3D metamaterial inclusions. Broadband infrared circular polarizers based on gold helical metamaterials [1] have been recently demonstrated using this technique; however, realizing these structures in the visible is hindered by the minimum realizable features imposed by the diffraction limit.

We propose here an alternative venue to realize strong, broadband bianisotropic effects in metamaterials, not based on chirality at the inclusion level, but instead on the relative orientation of strongly anisotropic achiral surfaces, introducing and applying the concept of twisted metamaterials. Our design is based on stacked planar metasurfaces realized with conventional lithographic techniques, suitably rotated from one layer to the next. Our goal is to show that, by introducing a twist in the lattice orientation of metamaterial inclusions, we can relax the usual requirements on fabrication and achieve exotic effects analogous to 3D metamaterials, but with much simpler fabrication schemes. In this context, it has been recently shown at microwave frequencies [18] that broadband linear polarization conversion may be obtained by coupling together twisted magnetic inclusions. Here we show that broadband circular polarization selectivity may be achieved in twisted arrays of metasurfaces without the need of complicated inclusion shape, with no requirement on the relative alignment, and at optical frequencies. We use a generalized Bloch analysis to model the cascaded structure [24], in combination with optical transmission-line theory [25], and show that this concept may relax several

constraints in the realization of 3D bianisotropic metamaterials, including inclusion shape requirements and lateral alignment between neighboring inclusions.

8.2 DESIGN OF TWISTED METAMATERIALS

8.2.1 Concept and optimization of twisted metamaterials

Consider first a single plasmonic metasurface made of gold [26] nanorods, with thickness $t = 50\,nm$, periods $d_x = 300$ nm, $d_y = 300$ nm, length $l = 250$ nm and width $w = 60$ nm. The shape of the nanorods is chosen to produce strong, resonant anisotropy within the plane, but it is strictly achiral. Due to the sub-wavelength thickness t, LCP and RCP transmissivities are expected to be identical for normal incidence at all frequencies. This may be readily proven by modeling the metasurface with its equivalent anisotropic shunt admittance $\underline{\mathbf{Y}}_s$ [27], which relates the averaged tangential polarization currents $\mathbf{J}_s$ to the total tangential electric field $\mathbf{E}_{tot}$ on the surface $\mathbf{J}_s = \hat{\mathbf{z}} \times \left(\mathbf{H}_{tot}\big|_{z=0^+} - \mathbf{H}_{tot}\big|_{z=0^-} \right) = \underline{\mathbf{Y}}_s \cdot \mathbf{E}_{tot}\big|_{z=0}$, producing a discontinuity in the total tangential magnetic fields $\mathbf{H}_{tot}$ on the array plane $z = 0$. By considering the reciprocity requirement $\underline{\mathbf{Y}}_s = \underline{\mathbf{Y}}_s^{\,T}$, where the superscript T denotes transpose, it follows that LCP and RCP transmissivities are bound to be equal [28]: $|T_{LL}| = |T_{RR}|$. A small cross-coupling component $T_{LR} = T_{RL}$ also arises, but it is not relevant to the following discussion.

To convert the strong surface anisotropy around the nanorod resonance into chiral bianisotropy, we consider cascading two identical metasurfaces with a subwavelength separation distance L and a specific rotation angle θ of the second surface compared to the first one (Figure 8.1(a)). In this context, 3D chiral inclusions have been obtained by pairing two strongly coupled 2D chiral planar particles [17], rotated one with respect to the other, based on the concept of extrinsic chirality. We consider here completely achiral

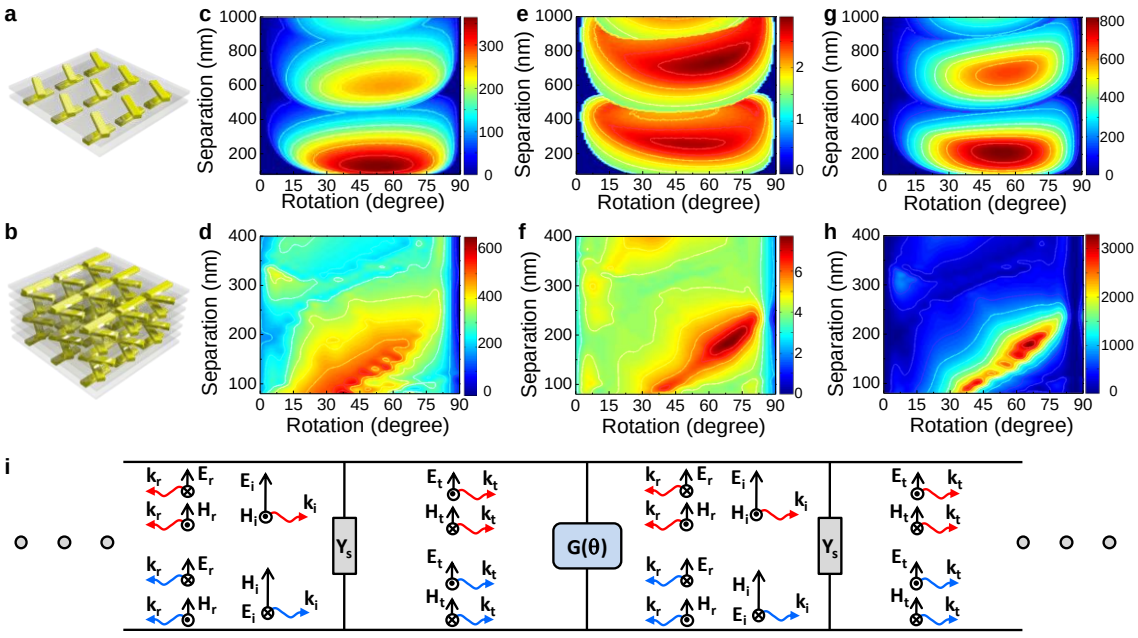

Figure 8.1: Circular polarization selectivity of twisted metamaterials. (a) Illustration of a pair of stacked metasurfaces with rotational twist θ and separation distance d, together with (b) calculated bandwidth in nanometers, (c) extinction ratio, (d) and figure of merit as defined in the text. (e) Illustration of a seven-layer twisted metamaterial, and corresponding (f) calculated bandwidth, (g) extinction ratio, (h) and figure of merit. (i) Transmission-line model, where $\underline{\mathbf{Y}}_s$ is the surface admittance of a single metasurface, $\underline{\mathbf{G}}(\theta)$ is the rotation matrix. (Reprinted with permission from Nature Communications 3, 870 doi:10.1038/ncomms1877. Copyright 2012 Nature Publishing Group)

inclusions (simple nanorods) forming strongly anisotropic arrays, with the aim of converting their anisotropy into magneto-electric coupling by rotation, as a pure lattice effect. As discussed in Ref. [27], our transmission-line model may be successfully applied to model this configuration, as sketched in the circuit model of Figure 8.1i, which includes a transmission-line segment to model each gap between neighboring metasurfaces and the rotation matrix $\underline{\mathbf{G}} = \begin{pmatrix} cos\theta & sin\theta \\ -sin\theta & cos\theta \end{pmatrix}$ describing the relative rotation of the second impedance tensor compared to the first one $\underline{\mathbf{Y}}_2 = \underline{\mathbf{G}}^{\mathrm{T}} \cdot \underline{\mathbf{Y}}_1 \cdot \underline{\mathbf{G}}$. In this scenario, T_{LL} and T_{RR} through the stack are no longer bound to have the same

magnitude and, using our analytical model, we are able to conveniently assess the predicted circular polarization properties of the metasurface pair by calculating the extinction ratio $\left|T_{\mathrm{RR}}/T_{\mathrm{LL}}\right|$ at each wavelength as a function of L and θ. Figure 8.2(a) shows, as an example, the wavelength dispersion of $\left|T_{\mathrm{LL}}\right|$ and $\left|T_{\mathrm{RR}}\right|$ for $L=120$ nm and $\theta=60°$. A right-handed rotation of the second array with respect to the first one produces preferential transmission of RCP waves, with maximum separation near the array resonance, spanning over a moderate wavelength range (~700 nm). We define the circular polarizer bandwidth of this pair as the span of wavelengths over which the extinction ratio is larger than $\sqrt{2}$ for clockwise rotation $0<\theta<90°$. In Figure 8.1 we show the calculated bandwidth (Figure 8.1(b)), the corresponding average extinction ratio $\left|T_{\mathrm{RR}}/T_{\mathrm{LL}}\right|$ (Figure 8.1(c)) and the overall figure of merit (FoM, Figure 8.1(d)), defined as the product of bandwidth and extinction ratio, as a function of L and θ. It is seen that optimal performance is obtained for subwavelength separation distances and for a rotation angle around $\theta\sim60°$. We did not consider here distances smaller than 80 nm, since our analytical model neglects higher-order Floquet modes in the coupling between neighboring metasurfaces, losing its accuracy for smaller distances. In any case, it is found that the optimal distance is in the range $L\sim150$ nm, and closer metasurfaces cannot achieve as large FoM. In this range, we have verified that our analytical results match very well with full-wave simulations of the pair.

Since a pair of achiral, anisotropic metasurfaces can support circular polarization selectivity over a moderately broad bandwidth after properly rotating one of them, it may be expected that by stacking a larger number of closely spaced metasurfaces with sequential rotation the FoM may increase, similar to the bandwidth increase in metamaterials formed by a large number of closely spaced resonant inclusions. We verify this possibility in the second row of Figure 8.1, in which we show analogous results for a

stack of seven metasurfaces for fixed separation distance L and angle of rotation θ between any two consecutive elements, as in Figure 8.1b. Indeed, it is seen that bandwidth, extinction ratio and overall FoM can dramatically increase by combining closely spaced metasurfaces with proper sequential rotation and period. This is indeed consistent with the way the bandwidth of metamaterials drastically increases compared to the resonance of their individual inclusions, provided that they are densely packed [29]. Optimal parameters are found in a similar range of L and θ, but with more selectivity in terms of their value for optimal performance.

8.2.2 Functionality and operation

To show how the bandwidth evolves when stacking metasurfaces with sequential rotation, we show in Figure 8.2 the evolution of the transmission coefficients for $L =$ 120 nm and $\theta = 60°$ when increasing the number of layers, as indicated in each inset. By cascading more layers, the bandwidth is gradually broadened, spanning nearly the entire visible range in the case of seven layers (Figure 8.2(f)), with also a much increased extinction ratio. For a right-handed twist, LCP waves are reflected within the bandwidth of operation, whereas RCP is transmitted, consistent with the previous discussion. It appears that, by increasing the number of stacked metasurfaces, we are able to move from a simple resonant response to a continuous stopband, transitioning from a one-element filter to a homogeneous twisted metamaterial.

In this regard, we have extended our analytical model to analyze the eigenmodal properties of this rotated stack for a number of layers $N \to \infty$, considering the generalized Bloch eigenmodes supported in a suitable reference system that rotates with each successive layer, analogous to the approach used to analyze linear arrays of rotated

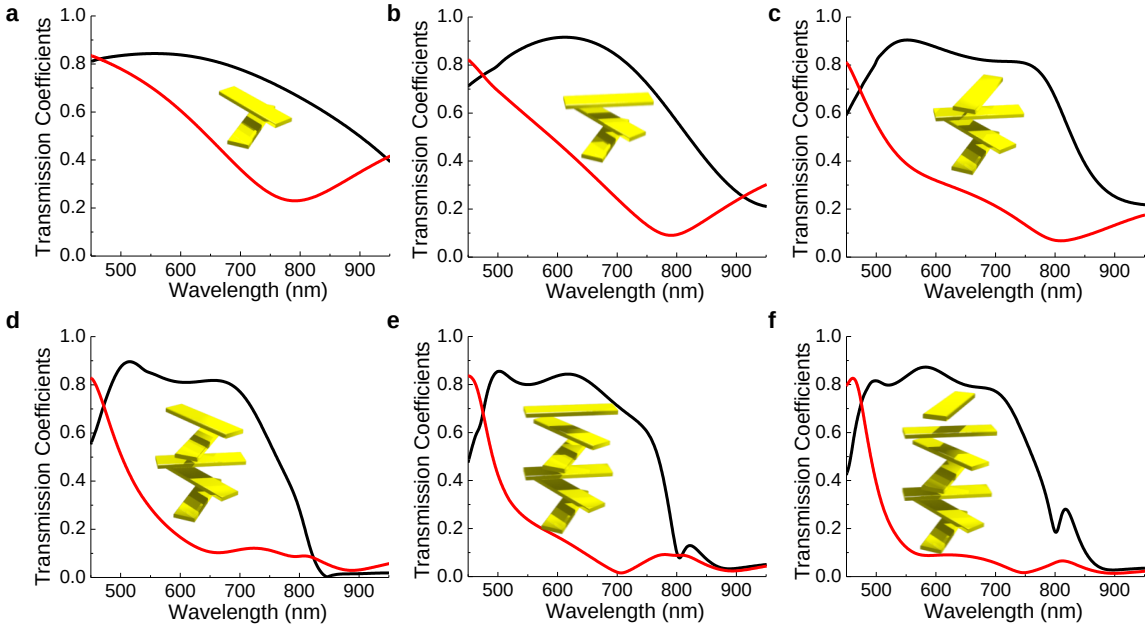

Figure 8.2: Evolution of the frequency response by increasing the number of stacks. Transmission of LCP and RCP waves through a stack of rotated metasurfaces by increasing the number of layers (L = 120 nm, θ = 60°). In (a)-(f) the number of layers increases from two to seven, with the insets illustrating one unit cell of the corresponding twisted metamaterial slab along the direction of propagation. (Reprinted with permission from Nature Communications 3, 870 doi:10.1038/ncomms1877. Copyright 2012 Nature Publishing Group)

particles [24]. Although the details of this homogenization theory for twisted metamaterials go beyond the focus of the present work, it is relevant to point out that we have verified how one of the two generalized eigenmodes supported by the homogenized twisted metamaterial, based on the parameters of Figure 8.2, is indeed characterized by purely LCP fields, and supports a continuous stopband spanning the visible range. This finding highlights the unique response of twisted metamaterials compared to extrinsic chirality or nematic liquid crystals: the subwavelength sequential rotation through the stack effectively transforms the strong resonant anisotropy of each metasurface into a unique form of broadband magneto-electric coupling, responsible for circularly-polarized

eigenmodes, sustained by the lattice rather than by the chirality of the individual inclusions. Period and twist angle of the stack can then be optimized to broaden and tune the stopband of one of them, to ensure the optimal operation as a circular polarizer.

It should be stressed that the functionality of the twisted metamaterial slab introduced here is very distinct from cholesteric liquid crystals or helicoidal materials [30], which also support circular polarization selectivity by sequential rotation of chiral molecules [4]. In those materials, the anisotropy of each layer is very weak, and the rejection of one circular polarization is obtained over several wavelengths based on Bragg reflection, under the condition that the helical pitch of the crystal is comparable to the wavelength of operation [5]. The operation of twisted metamaterials, on the contrary, is based on strong, resonant anisotropy at the metasurface level (without relying on chirality at all), which is broadened by the strong coupling among closely spaced surfaces, over a subwavelength period. The rotational pitch of the metamaterial considered in Figure 8.2, for instance, is about one tenth of the one that would be required in a cholesteric liquid crystal to obtain some form of polarization selectivity, and we obtain here a much larger extinction ratio, across a subwavelength thickness, with much more broadband response. The rotational twist along the lattice adiabatically transforms linearly polarized eigenmodes, supported by resonant, anisotropic metasurfaces, into circularly polarized ones. The clearest differences between twisted metamaterials and cholesteric liquid crystals or helicoidal materials consist in the drastically larger bandwidth, associated with strong coupling among neighboring metasurfaces, and the fact that cholesteric liquid crystals reflect the handedness associated with the helical rotation due to Bragg reflection, whereas the twisted metamaterial transmits that polarization, since its rotation over a subwavelength scale adiabatically rotates in the same direction as the eigenmodal polarization.

8.2.3 Shift invariance and robustness to misalignments

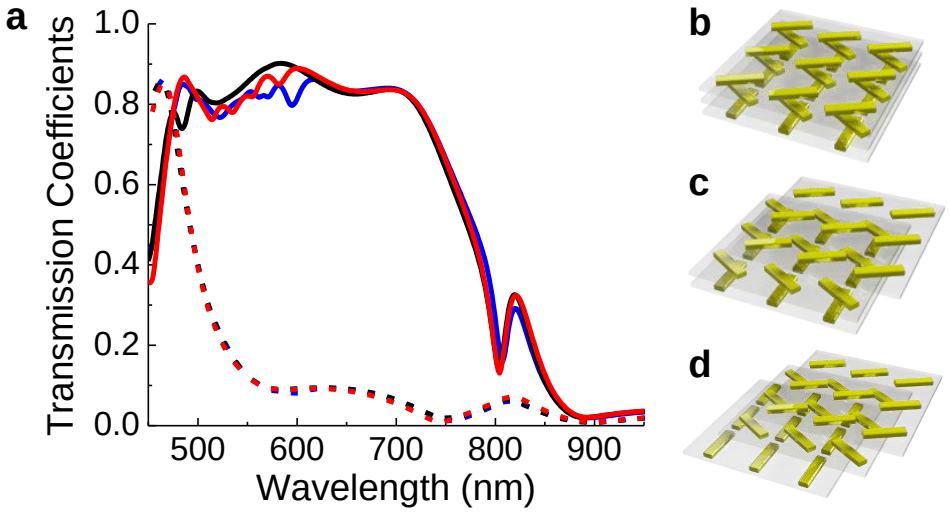

Figure 8.3: Robustness to misalignment. (a) Three sets of transmission coefficients are presented, corresponding to: (b) ideal alignment of three consecutive metasurfaces (black); (c) misalignment of one metasurface along one transverse direction (blue); (d) misalignment of all metasurfaces in the stack in both directions (red); solid curves refer to RCP, dashed curves to LCP. (Reprinted with permission from Nature Communications 3, 870 doi:10.1038/ncomms1877. Copyright 2012 Nature Publishing Group)

One additional advantage of the twisted metamaterial concept is its expected robustness to misalignments, which may be found in layer-by-layer fabrication. Since the proposed concept is based on the metasurfaces coupled through the dominant transverse Floquet mode, and not on the individual inclusion resonant interaction with light, it is expected that arbitrary alignment between neighboring layers should not affect the overall response of the twisted metamaterial. This is obviously drastically different from extrinsic chirality, which is inherently based on the strong coupling between neighboring pairs of rotated inclusions. This is verified numerically in Figure 8.3, where we show LCP and RCP transmission coefficients for a stack of seven layers, similar to Figure 8.2(f), considering different forms of misalignment, as indicated in the insets. When one of three consecutive metasurface is misaligned in one direction (inset (c)), or even when

all of them are misaligned in both directions (inset (d)), still the same transmission curves as in the ideally aligned case (inset (b)) are obtained. The total level of loss is slightly increased when misalignment and disorder is introduced, but without significantly affecting the performance of the device.

To get a better grasp of the origin of this shift invariance, we took one step further in the analysis before we realize the multilayer device. Initially we want to show how the packing density and super-lattice geometries affect the coupling efficiencies to higher order floquet modes. Since the major difference between a metasurface and a grating surface is that the periodicity of a metasurface is much smaller than the wavelength of excitation, so the nearby meta-atoms experience collective and coherent excitations. Consequently, when employing floquet theory, except for the fundamental mode (the zero-th order) that can propagate though the stacked layers, the higher order floquet modes are all evanescent and decaying exponentially away from each metasurface. It is expected that when two metasurfaces are within close vicinity to each other, the excited near fields from the first metasurface will couple strongly to the next. This coupling can be visualized as the coupling efficiency of fundamental modes to higher order floquet modes.

To visualize this, we simulate only one metasurface but with the excitations placed at different distance (d) away from the metasurface to experience the field it will couple to the next metasurface if it were at that location. This result is shown in Figure 8.4 (b) to (d), which was obtained using full wave numerical simulations with an increasing d varying from 60 nm to 200 nm, where d is the center-to-center distance between two adjacent metasurfaces, so that the thickness of the metasurface has been taken into account. Although the metasurface thickness in this study is highly

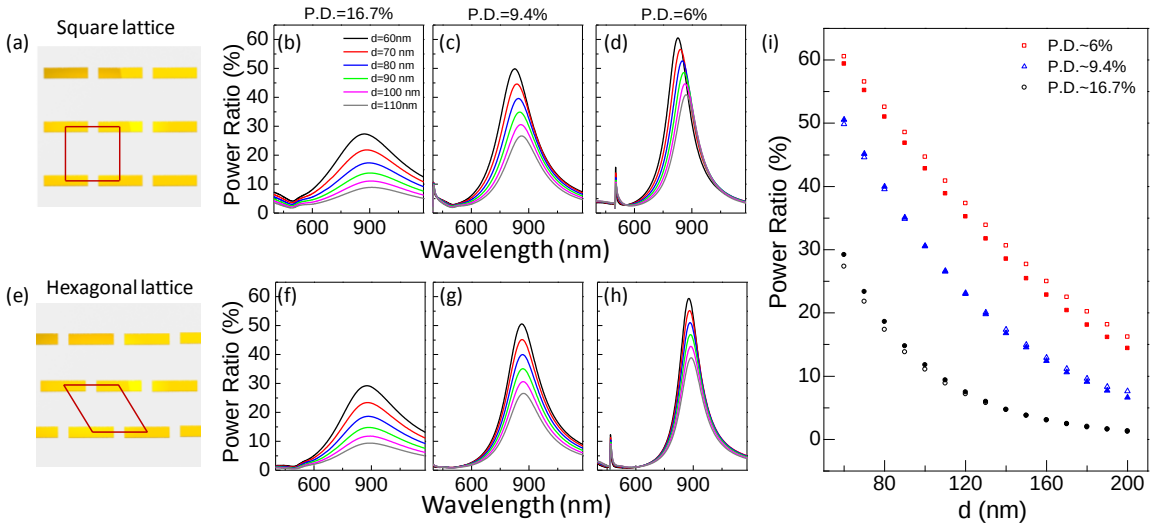

Figure 8.4: Simulation of percentage of power coupled from fundamental modes to higher order floquet modes as a function of wavelength. (a)-(d) the square lattices, and (e)-(h) the hexagonal lattices. The periodicity in consideration for square lattices varies from (b) 300 nm, and (c) 400 nm, to (d) 500 nm. For (f)-(h) hexagonal lattices shows the same packing densities corresponding to (b)-(d). (i) Maximum power ratio collected from the plots as a function of the metasurface separation distance for comparison under different packing geometries. The solid symbols represent hexagonal lattices, and void symbols represent square lattices.

subwavelength ($z < \lambda_0 / 10$, with λ_0 being the wavelength in vacuum), it is no longer negligible when considering near field coupling. When d is within twice of the thickness ($d \leq 100\,nm$), Figure 8.4(b) shows more than 10% of the power will be coupled to the 1st order floquet modes with the fundamental modes circularly polarized for the metasurfaces with a 300 nm square lattice periodicity, whose packing density (P.D.) is 16.7%, defined as the area of the meta-atom divided by the area of the unit cell. The super lattice geometry is illustrated schematically in Figure 8.4(a), with the red lines indicating the unit cell. When the period of the metasurface is gradually increased approaching the excitation wavelength, the percentage of coupling to higher order modes will be increased at the same time; maxima of 50% (Figure 8.4(c)) and 60% (Figure 8.4(d)) power coupling to higher order modes (up to 18 modes) for periods of 400 nm

(P.D.=9.4%) and 500 nm (P.D.=6%) square lattices are observed. This is because the periodicity affects the values of the k vectors of the higher orders, and simultaneously affects the decay rate of the fields. The decay rate will decrease for an increasing period due to a reduced effective permittivity. At the same time, the higher rate of power coupled to higher order floquet modes, the more the spectra will be affected by relative lateral misalignment at the inclusion-level. It is also evident that near the resonance frequency, the coupling is dramatically enhanced, which is due to the strongly localized field oscillation near resonances. In Figure 8.4(f)-(h), we showed similar set of calculations with the same packing densities corresponding to Figure 8.4(b)-(d), but with hexagonal lattice geometries (illustrated in Figure 8.4(e)). The maximum coupling efficiencies for these configurations are summarized in Figure 8.4(i). It is seen that with the same packing densities, the power ratios that couple to higher order floquet modes are similar especially for densely packed cases. However, when the packing density decreases, the hexagonal lattice will exhibit a lower coupling rate, which is evidenced from the red curves in Figure 8.4(i), where the P.D. is equal to 6%; when the distance between metasurfaces are larger, the two curves with different lattice geometries deviate from each other. In other words, to ensure less coupling to the higher order modes (maintaining high coupling ratios to fundamental mode), the meta-atoms composing the surface need to be more densely packed. For instance, for metasurfaces with packing densities of 16.7% (black curves in Figure 8.4(i)), the absolute separation distance between these surfaces needs to be at least the thickness of the metasurface (d>100 nm), and at the same time, larger than ~1/6 of the periodicity to keep the coupling efficiency to higher orders below 10%.

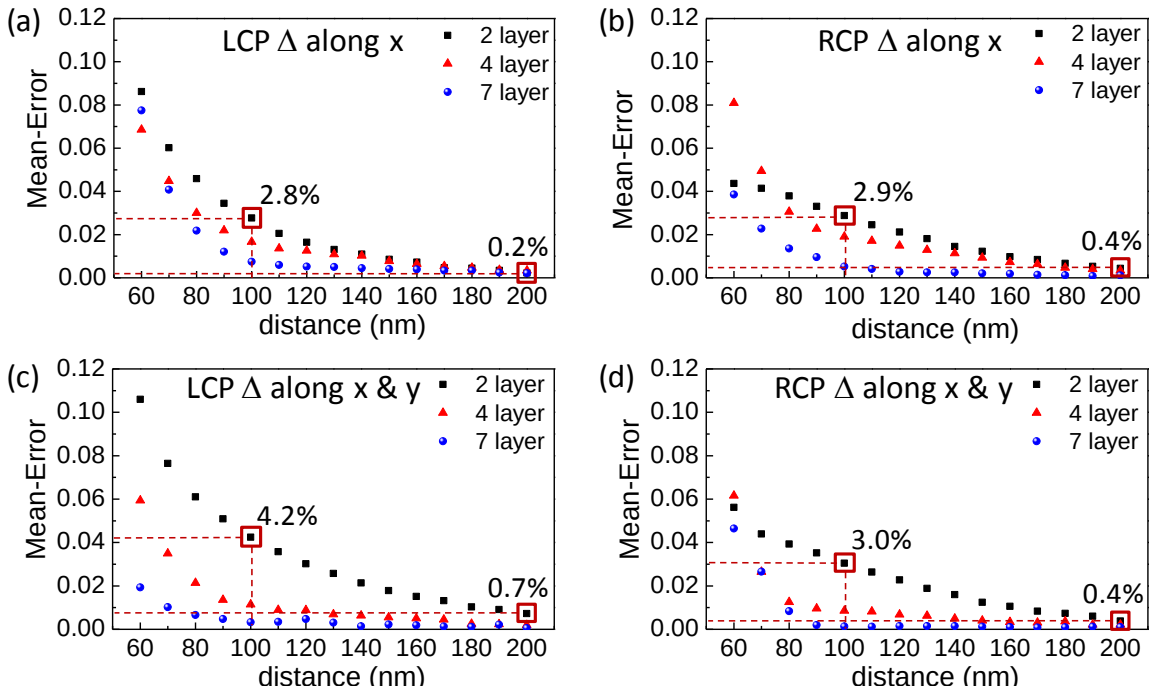

Figure 8.5: Simulated results of Mean-Error when comparing perfectly aligned metasurfaces at the inclusion level to those misaligned for layer numbers of 2, 4 and 7. The Mean-Error is defined as the mean of the Euclidean distance between the aligned and misaligned curves. LCP and RCP denotes the polarization state of the excitation. No analyzer was included in the simulation, so the transmission represents the totally transmitted power without differentiating the polarizations of the transmitted fields. Assume the metasurface is with the z=constant plane. (a), and (b) Shift x denotes the misalignment is along the x direction, with an accumulated shift of L/2, where L is periodicity. (c), and (d) shows the shifts along both the x and the y direction with maximum misalignment of L/2.

To visualize the spectral change due to misalignment, we expressed it in terms of the mean value of the Euclidean distance between the perfectly aligned spectra and the misaligned ones with circular polarized impinging waves normally incident to different layers of stacked metasurfaces. We define this value as "Mean-Error", which is again calculated using full wave numerical simulations, and shown in Figure 8.5. The measurface stack with layer numbers of two, four and seven are analyzed with various d ranging from 60 nm to 200 nm at a 10 nm increment, where the lateral misalignment is

set to increase at the same increment from layer to layer until it reaches the maximum shift of $L/2$, $\Delta = \frac{L}{2(n-1)}$, where L is the unit cell dimension and n is the total number of layers in the stack. Figure 8.5(a) and (b) only consider the shift along the x direction, and Figure 8.5(c) and (d) take into account both x and y shift within the metasurface plane. The red squares in Figure 8.5 indicate the mean-error for 2 layer metasurface stack with d=100nm and d=200nm, respectively, which are later compared to experimental measurements. The mean-error is a good indication of how the misalignment can affect the interaction between layers, and in particular, it indicates how the near field coupling is transferred from layer to layer and affects the final transmission spectra. In both Figure 8.4 and the Figure 8.5, the spacer in the simulations is vacuum, and no adhesive layer is considered; when compared with experimental conditions, the realized device will exhibit spectra that are red-shifted due to the substrate effect. Figure 8.5 shows the error decreases monotonically when the separation distance d between metasurfaces increases. Special attentions are paid to metasurface stacks with d<70 nm, where not necessarily fewer layers present highest mean-error, suggesting the near field coupling plays a dominant role at these distances, inducing extra scattering loss due to the misalignment. When d reduces close to its limit $d = 60$ nm, the absolute thickness of the vacuum spacer is only 10 nm, the fundamental mode can couple more than 50% of power to higher order floquet modes depending on lattice geometries. However, even at the smallest d, the mean-error is within 10%, which suggests that circular polarized excitations are less affected by the near field coupling, therefore confirming our previous assumption that the lattice chirality is mainly attributed to the zero-th diffraction orders for multilayer designs, where the effect from the higher order terms can be neglected as d increases.

To confirm this shift-invariant theory before we proceed to the final multiple layer twisted metamaterial designs, we experimentally realized two layer metasurface stacks for different degrees of misalignment, and analyze the effect from both the misalignment Δ and the layer separation d. The reason we picked two layers has dual sides: on the one hand, two-layer device is the simplest prototype to be realized among all the multilayer designs; on the other hand, based on the analysis in Figure 8.5 two-layer device is the worst case scenario compared to all the multilayer designs in terms of shift invariance. In other words, if the shift invariance is valid in two-layer devices, it will be more robust for more layer cascaded structures based on the same design principles.

We utilized a dedicated etch-back approach to achieve planarization and multilayer fabrication. The fabrication procedure will be discussed with great details in the next section. In total six samples of two-layer metasurface stacks were fabricated with three levels of misalignment registrations and two separation distances as reported in Figure 8.6, which shows SEM images with corresponding illustrations of the three alignment configurations: no misalignment (Figure 8.6(a), (d)), misalignment along only x direction (Figure 8.6(b), (e)), and misalignment along both x and y directions (Figure 8.6(c), (f)) at the inclusion level. Figure 8.6(g)-(i) show the SEM images for these three configurations with d= 100 nm, and Figure 8.6(j)-(l) correspond to d= 200 nm.

Figure 8.7(a) and (b) show the spectral measurements of the transmittance through the six samples; and the corresponding full wave numerical simulations are shown in Figure 8.7(c) and (d). In all the cases, the transmittance curves with right hand circular polarized (RCP) excitation match well with simulation results, but those for left hand excitations (LCP) show some discrepancies. It is because the LCP mode is the one that is aimed to be suppressed through the stacked layers, for an infinite series of these

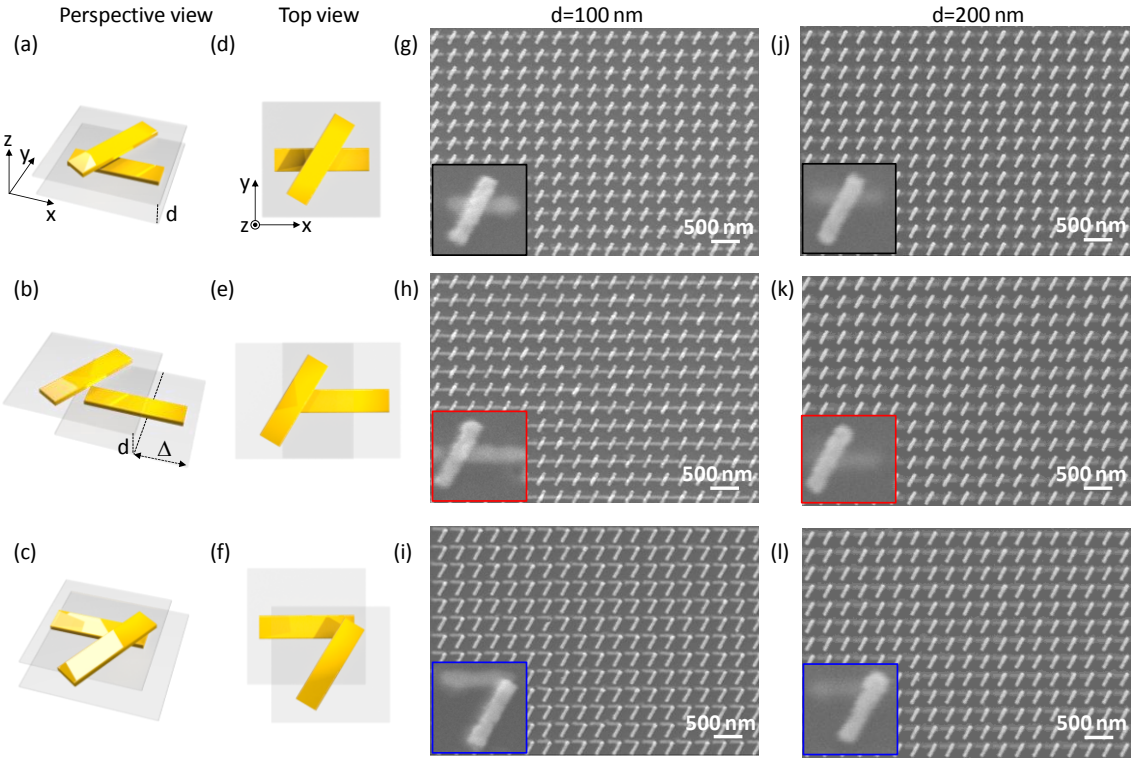

Figure 8.6: Illustration of different registrations of the alignment and the corresponding scanning electron microscope (SEM) images for two-metasurface stack with separation distance d=100nm and d=200nm respectively. Perspective views of the two-metasurface stack with (a) no misalignment, (b) lateral misalignment along the x direction, (c) lateral misalignment along both x and y directions at the inclusion level. (d)-(f) are the corresponding top view images for these configurations. (h)-(i) are SEM images for d=100nm cases for the three registrations; and (j)-(l) are the SEM images for d=200. The scale bars in the SEMs are 500 nm.

metasurface stacks, a complete stop-band can be formed to block the propagation of the LCP mode. Therefore, fabrication imperfections such as local thickness and shape variations are more subjective to affect the designated stop-band of the LCP mode. From these measured spectra, we extracted the previously defined mean-errors, these values for d=100 nm cases are 7.1% for LCP excitation with shift along x, 9.1% for LCP with shift along both directions, 5.7% for RCP with shift along x, and 8.6% for RCP with shift

along both directions. While for d=200 nm, these mean-errors are 2.5%, 1.0%, 1.7% and 0.7%, correspondingly. Although these errors are slightly bigger than what are predicted from Figure 8.5, which are supposed to reduce from 2.8% (or 4.2%) to 0.2% (or 0.7%) with LCP excitations as d increases from 100 nm to 200 nm, the overall predicted trend and final spectra have been well matched between simulations and experiments.

8.3 EXPERIMENTAL REALIZATION AND CHARACTERIZATION OF TWISTED METAMATERIALS BASED ON CASCADED METASURFACES

We have verified the functionality of the proposed twisted metamaterial by realizing and characterizing several devices, going from one-layer to a four-layer stack. Figure 8.4a shows the relevant fabrication steps of our design, as described in more detail in the Methods section. Our final fabricated sample consists of four planar arrays of gold nanorods, based on the design of Figure 8.2. Figure 8.8(b) shows the scanning electron microscope (SEM) images of the realized device, obtained using focused-ion beam (FIB) milling to reveal the details of each cascaded layer. The atomic form microscope (AFM) image and characterization in Figure 8.8(c)-(e) shows the details of the planarization process that we applied to realize the cascaded structure, as described in the Methods section. We have performed full-wave numerical simulations and experimental characterization of LCP and RCP transmissivities through the several stages of this device, going from a one-layer metasurface to the four-layer twisted metamaterial slab, sequentially stacking more metasurfaces.

In our simulations, shown in Figure 8.9(a)-(d), we have included the dielectric spacers and titanium adhesion layers required for the realization of the twisted metamaterial (see fabrication details in the Methods section), which were not considered in Figure 8.2. As predicted by simulations, their presence slightly shifts the operation of the twisted metamaterial to longer wavelengths, and contributes to additional absorption

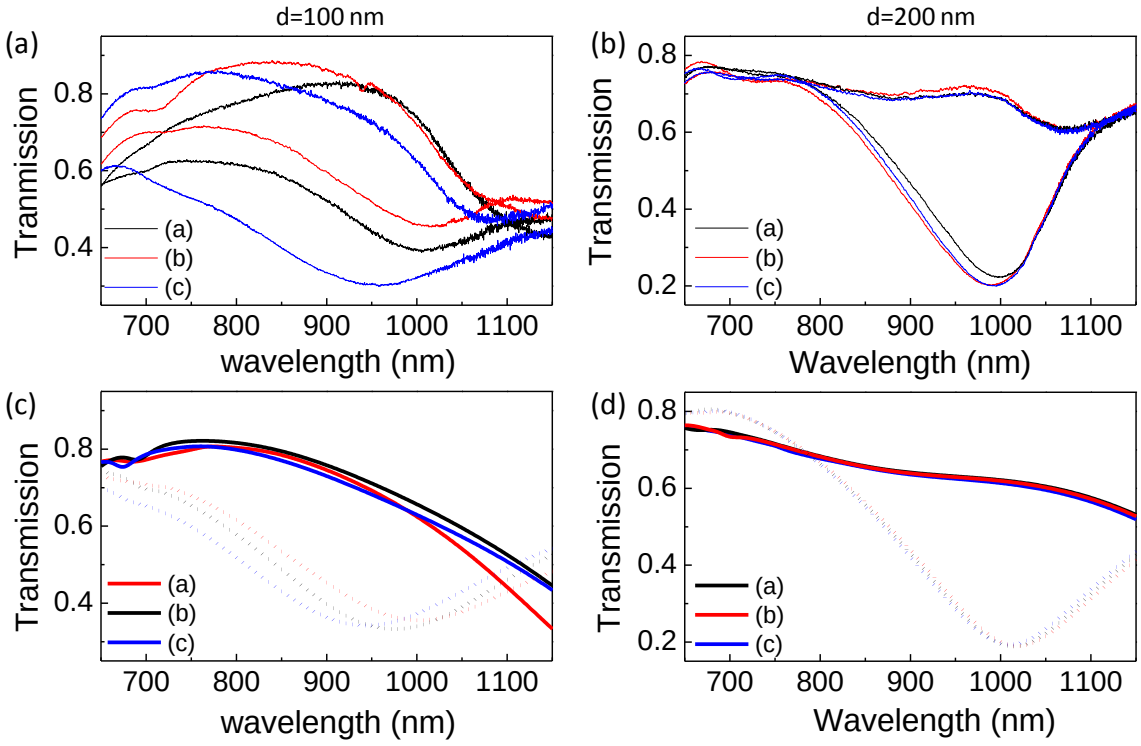

Figure 8.7: Comparison of experimental measurements and numerical simulations of transmittance for difference degree of shift corresponding to the configurations in Figure 8.6 (a), (b) and (c), which are color coded as black, red, and blue, respectively. (a) is the measurement for d=100 nm case, and (b) the measurement for d=200 nm case. (c) and (d) are their corresponding numerical simulations to confirm the line-shape.

losses residing in the thin adhesion layers, which slightly reduces the bandwidth and FoM of the polarizer. Measured and simulated curves follow each other quite closely: the single metasurface (Figure 8.9(e)) provides the expected identical transmission of LCP and RCP waves, but as soon as a second layer is cascaded with proper twist and distance (Figure 8.9(f)), we obtain some form of polarization selectivity. As predicted by our theory, a larger number of layers (Figure 8.9(g), (h)) ensures better extinction ratios and increased bandwidths. Despite some unwanted absorption due to the nonideal fabrication conditions, the four-layer device operates as a broadband, ultrathin circular polarizer,

consistent with the operation of a 3D bianisotropic metamaterial, confirming the functionality as a twisted metamaterial.

8.3.1 Nanofabrication methods

The fabrication stages are shown in Figure 8.8(a). Alignment marks with 100 nm gold thickness were first fabricated on bare glass substrate (C1737-0107, Corning® low alkaline earth from Delta Technologies), then 100 nm silicon dioxide was deposited on the substrate using ebeam evaporator. Ebeam resist ZEP 520 was first diluted with ZEP A (Anisole), then spun onto the substrate to obtain a thickness of 100 nm. The pattern was written using a JBX-6000FS/E ebeam aligner at an accelerating voltage of 50KV. After exposure, the sample was developed in ZED-N50 (Emyl Acetate). The pattern was then transferred to the silicon dioxide thin film by reactive ion etching using a gas mixture of CF4 and Helium in TRION Oracle plasma etcher to etch off 55nm of silicon dioxide. A 5 nm Titanium adhesion layer and 50nm Gold were sequentially deposited onto the sample using CHA ebeam evaporator. Then, the sample underwent the liftoff process in N-methyl-2-pyroridone to complete the first layer. 100nm silicon dioxide layer served as a dielectric spacer, coated through ebeam evaporation. The surface was automatically planarized after metal liftoff.

A special effort was made to ensure flat surface after each metal nanorod deposition. To achieve this, the metal liftoff ebeam resist mask was first used to etch 55-nm-deep trenches in the substrate via reactive ion etching; a 55-nm-thick metal layer was then deposited. After the liftoff process, the metal nanorods are positioned in the trenches etched in the substrate. The AFM image in Figure 8.8(c)-(e) shows the planarization measurement of each layer before and after the deposition of a silicon dioxide spacer. The planarization process reduced surface height variation from 55 nm to 5 nm.

Subsequent layers were added by repeating similar steps, from silicon dioxide deposition to metal liftoff.

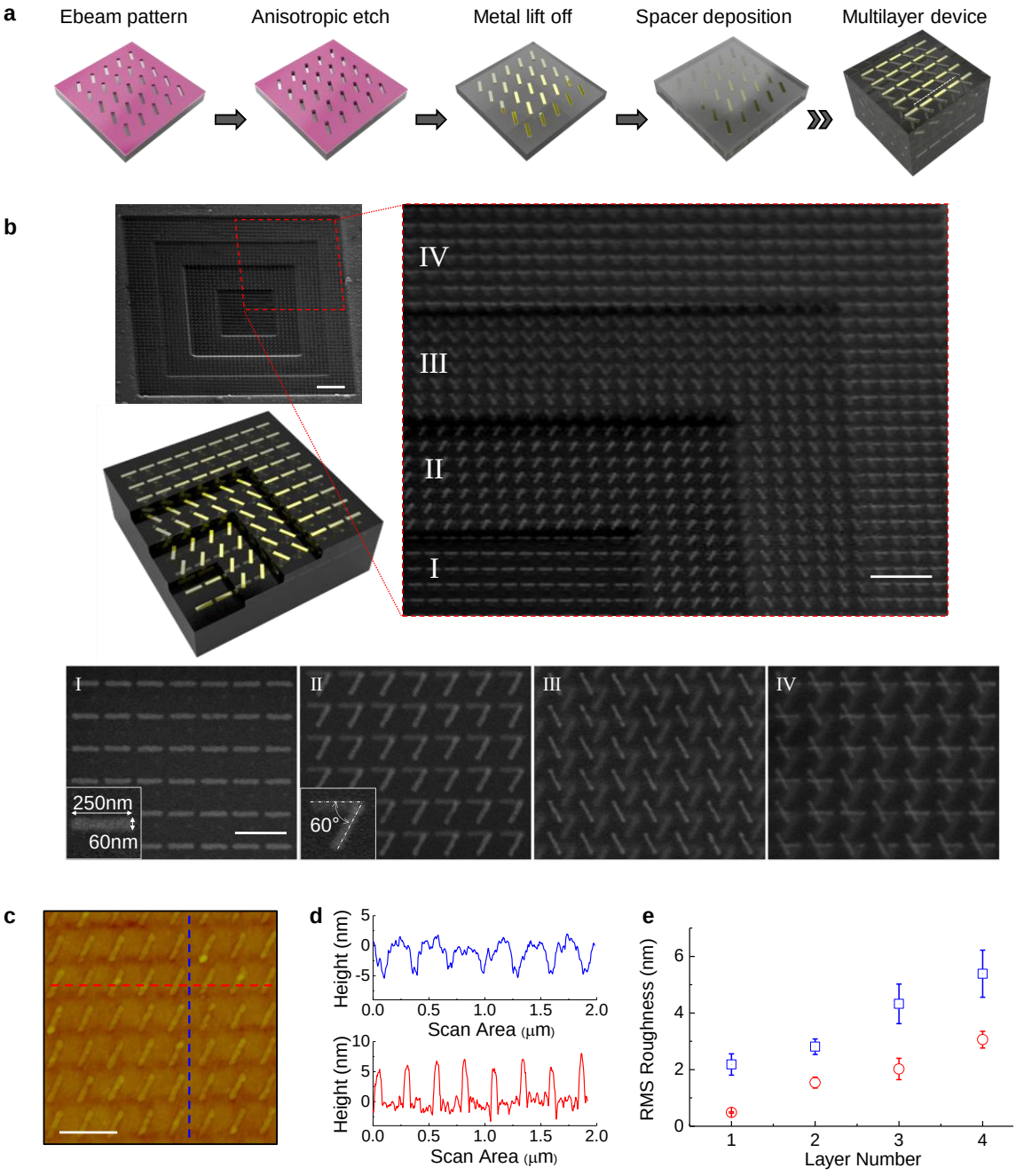

Figure 8.8: Device fabrication. (a) Fabrication scheme to realize each layer of the twisted metamaterial. A multi-layer stack can be obtained after repeating the first four steps (see Methods section). (b) Multilayer SEM view of the realized 4 layer device. The images are prepared through FIB milling to reveal each layer, where the I, II, III, IV mark the corresponding layers. The inset in layer I shows the dimensions of each nanorod; the inset in layer II shows the measured rotation angle between adjacent layers. The sample was prepared by coating 5nm of Pt/Pd before SEM imaging to reduce charging effect, due to the non-conducting nature of the silicon dioxide substrate. The scale bars in the SEM images from top to bottom are 2 μm, 1 μm, and 500 nm, respectively. (c) AFM image of a two-layer device and corresponding surface profile to measure the planarization: the first layer (horizontal rods) considers the planarization after metal-liftoff and silicon dioxide spacer deposition (blue curve in panel d), the peak to valley height is within 5 nm; the second layer (60° tilted rods) is obtained after metal liftoff, but before silicon dioxide deposition (red curve in panel d), here the peak to valley height is within 7 nm. The scale bar in panel c is 500 nm. (e) shows the root mean square (RMS) surface roughness of each layer before (blue square) and after (red circle) silicon-dioxide deposition. Surface roughness is improved after silicon dioxide deposition. (Reprinted with permission from Nature Communications 3, 870 doi:10.1038/ncomms1877. Copyright 2012 Nature Publishing Group)

8.3.2 Optical measurements

Testing was conducted after processing each layer. To test the resonance of single layer, a Halogen broad band light source was coupled into a spectrograph (Princeton instrument SpectraPro-2500i) to scan the wavelength with a resolution of 2 nm. The output light from the spectrograph was sequentially passed through a linear polarizer (Thorlabs LPVIS050), a broadband quarter-wave plate (Thorlabs AQWP05M-980), the sample, a second broadband quarter-wave plate, a second linear polarizer, and finally an InGaAs detector (Princeton instrument Model ID441-C).

8.4 CONCLUSIONS

Chiral bianisotropy, purely based on a lattice effect, has been obtained using an array of purely three-dimensionally achiral inclusions, realized with standard lithographic techniques and planarized technology. We believe that with a similar technique it may be possible to realize broadband circular polarizers at even shorter wavelengths, spanning

the entire visible range, and reduce the amount of losses by avoiding lossy metals for the adhesion layers and considering lower-loss plasmonic materials for the nanorods, e.g., silver. The proposed broadband circular polarizers may be directly integrated into nanophotonic devices, due to its ultralow and planar profile. Our proposed concept may be easily scaled up to longer wavelengths for a variety of exciting applications in mid-infrared and terahertz spectral range, for which convenient sources, such as quantum cascade lasers, are available, but advanced optical elements for polarization control such as achromatic quarter wave plates or broadband circular polarizers are currently unavailable.

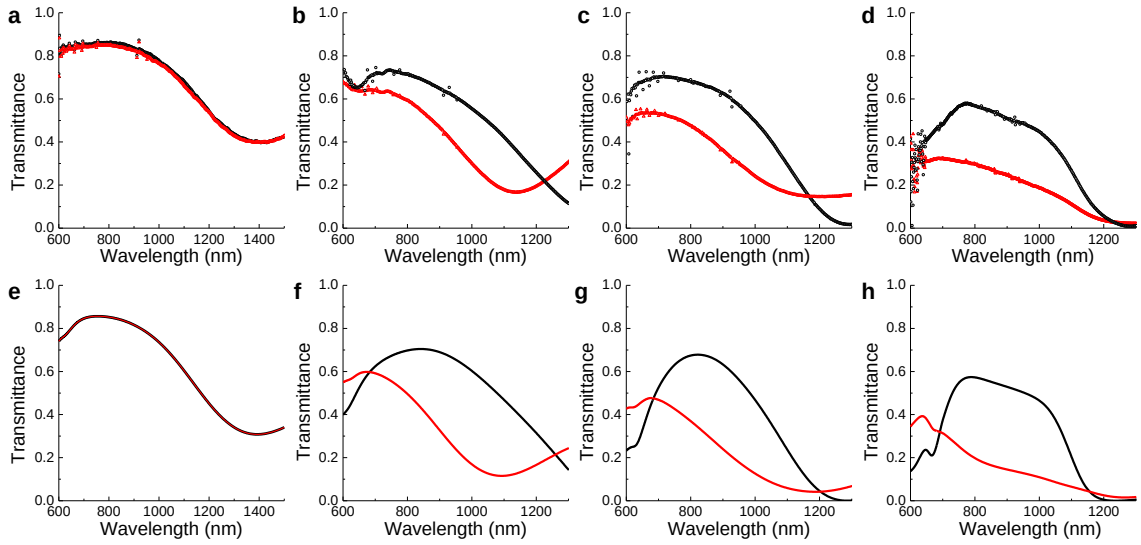

Figure 8.9: Comparison between measurements and simulations. (a)-(d) full-wave numerical simulations for twisted metamaterial slabs with 1 to 4 layers. As predicted by theory and simulations, the bandwidth and extinction ratio is increased with a larger number of layers of the twisted metamaterial. (e)-(h) corresponding experimental measurements, where black circles represent RCP and red triangles represent LCP transmission; the measurement is obtained by scanning the wavelength with a resolution of 2 nm as described in the Methods section. (Reprinted with permission from Nature Communications 3, 870 doi:10.1038/ncomms1877. Copyright 2012 Nature Publishing Group)

More broadly, we believe that the proposed concept of twisted metamaterials, obtained by breaking the periodicity of conventional metamaterials introducing a sequential twist within the lattice, may broaden the venues in which optical metamaterials may be realized and applied, by relaxing several of the requirements on the inclusion shape. This may have groundbreaking impact in a variety of novel metamaterial devices and applications, beyond polarization manipulation and control, e.g., in tailoring spatial dispersion or modal propagation. We are currently exploring some of these venues.

8.5 REFERENCES

[1] Gansel, J. K. et al. Gold helix photonic metamaterial as broadband circular polarizer. Science 325, 1513-1515 (2009).

[2] Kopp, V.I. et al. Chiral fiber gratings. Science 305, 74-75 (2004).

[3] Huang, Y. H., Zhou, Y. and Wu, S. T. Broadband circular polarizer using stacked chiral polymer films. Opt. Express 15, 6414-6419 (2007).

[4] Oseen, C. W. The theory of liquid crystals. Trans. Faraday Soc. 29, 883-899 (1933).

[5] De Vries, H. Rotatory power and other optical properties of certain liquid crystals. Acta Cryst. 4, 219-226 (1951).

[6] Broer, D. J., Lub, J. and Mol, G. N. Wide-band reflective polarizers from cholesteric polymer networks with a pitch gradient. Nature 378, 467-469 (1995).

[7] Shalaev, V. M. Optical negative-index metamaterials. Nat. Photonics 1, 41-48 (2007).

[8] Soukoulis, C. M. and Wegener, M. Past achievements and future challenges in the development of three-dimensional photonic metamaterials. Nat. Photonics 5, 523-530 (2011).

[9] Liu, N. et al. Three-dimensional photonic metamaterials at optical frequencies. Nat. Mater. 7, 31-37 (2008).

[10] Liu, N., Liu, H., Zhu, S. and Giessen, H. Stereometamaterials. Nat. Photonics 3, 157-162 (2009).

[11] Bai, B., Svirko,Y., Turunen, J. and Vallius, T. Optical activity in planar chiral metamaterials: Theoretical study. Phys. Rev. A 76, 023811 (2007).

[12] Jen, Y.-J. et al. Biologically inspired achromatic waveplates for visible light. Nat. Commun.2, 363 (2011).

[13] Kuwata-Gonokami, M. et al. Giant optical activity in quasi-two-dimensional planar nanostructures. Phys. Rev. Lett. 95, 227401 (2005).

[14] Rogacheva, A. V., Fedotov, V. A., Schwanecke, A. S. and Zheludev, N. I. Giant gyrotropy due to electromagnetic-field coupling in a bilayered chiral structure. Phys. Rev. Lett. 97, 177401 (2006).

[15] Decker, M., Klein, M. W.,Wegener, M. and Linden, S. Circular dichroism of planar chiral magnetic metamaterials. Opt. Lett. 32, 856-858 (2007).

[16] Decker, M. et al. Strong optical activity from twisted-cross photonic metamaterials. Opt. Lett. 34, 2501-2503 (2009).

[17] Plum, E., Fedotov, V. A., Schwanecke, A. S., Zheludev, N. I. and Chen, Y. Giant optical gyrotropy due to electromagnetic coupling. Appl. Phys. Lett. 90, 223113 (2007).

[18] Wei, Z., Cao, Y., Fan,Y., Yu, X. and Li, H. Broadband polarization transformation via enhanced asymmetric transmission through arrays of twisted complementary split-ring resonators. Appl. Phys. Lett. 99, 221907 (2011).

[19] Guerrero-Martinez, A. et al. Intense optical activity from three-dimensional chiral ordering of plasmonic nanoantennas. Angew. Chem. Int. Ed. 50, 5499-5503 (2011).

[20] Demetriadou, A. and Pendry, J. B. Extreme chirality in Swiss roll metamaterials. J. Phys. Condens. Matter 21, 376003 (2009).

[21] Plum, E. et al. Metamaterials: Optical Activity without Chirality. Phys. Rev. Lett. 102,113902 (2009).

[22] Deubel, M. et al. Direct laser writing of three-dimensional photonic-crystal templates for telecommunications. Nat. Mater. 3, 444-447 (2004).

[23] Maruo, S., Nakamura, O. and Kawata, S. Three-dimensional microfabrication with two-photon-absorbed photopolymerization. Opt. Lett. 22, 132-134 (1997).

[24] Van Orden, D., Fainman, Y. and Lomakin, V. Twisted chains of resonant particles: optical polarization control, waveguidance, and radiation. Opt. Lett. 35, 2579-2581 (2010).

[25] Alù, A. and Engheta, N. Optical nano-transmission lines: synthesis of planar left-handed metamaterials in the infrared and visible regimes. J. Opt. Soc. Am. B 23, 571-583 (2006).

[26] Johnson, P. B. and Christy, R. W. Optical constants of noble metals. Phys. Rev. B 6, 4370-4379 (1972).

[27] Zhao, Y., Engheta, N. and Alù, A. Homogenization of plasmonic metasurfaces modeled as transmission-line loads. Metamaterials 5, 90-96 (2011).

[28] Zhao, Y. and Alù, A. Manipulating light polarization with ultrathin plasmonic metasurfaces. Phys. Rev. B 84, 205428 (2011).

[29] Alù, A. and Engheta, N. Three-dimensional nanotransmission lines at optical frequencies: A recipe for broadband negative-refraction optical metamaterials. Phys. Rev. B 75, 024304 (2007).

[30] Lakhtakia, A. Anomalous axial propagation in helicoidal bianisotropic media. Opt. Comm. 157, 193-201 (1998).

Chapter 9: Conclusions and Future Directions

9.1 Conclusions

In this study, we have developed a novel paradigm to use single element nanoantenna, composite of nanotenna arrays in two-dimensional (metasurfaces) and three-dimensional (metamaterials) forms to control and manipulate light and its polarizations at the nanoscale, which can possibly bypass the limitations from conventional designs and realization of 3D metamaterials. The final design of the twisted metamaterial concept was borrowed from nature and biological species, whose complex structure can exhibit superior function to detect, control and manipulate the polarization state of lights for their orientation, signaling and defense. Inspired by this concept, we theoretically investigated and designed metasurfaces/metamaterials models, with the help of fully vectorial numerical simulation tools, and we have been able to outline the limitations and ultimate conditions under which the averaged optical surface impedance concept may accurately describe the complex wave interaction of planar plasmonic metasurfaces. We also experimentally explored various technological approaches compatible with these goals, such as the realization of lithographic single element nanoantenna and antenna arrays with complex circuit loads, periodic arrays of plasmonic nanoparticles or nanoapertures, and stacks of rotated plasmonic metasurfaces. At the conclusion of this effort, we have been able to theoretically analyze, design and experimentally realize and characterize the feasibility of using discrete metasurfaces to realize phenomenon and performance that are available in nature biological species.

9.2 Future directions and outlooks

The field of plasmonics and metamaterials is still facing big challenges. For example, losses have been an issue for almost all the plasmonic based devices, in

particular for applications in lasers and waveguides. Thanks to the expitaxial growth technology, low-loss single crystalline silver can be grown with almost half of the intrinsic loss at the optical frequencies [1],[2]. The advent of this superior low loss material brings new possibilities for plasmonics to study nano-lasers and biosensings. Another emerging material is called transparent conductive oxide (TCO) [3]-[6], among these, Gallium, Aluminum doped Zinc Oxide (GZO/AZO) and Indium Tin Oxide (ITO) have been actively under investigation recently. These materials exhibit much lower loss in the telecommunication frequencies, and could open new venues for long range surface plasmon polariton waveguides at the near IR regime.

New directions, such as using engineered plasmonic metasurfaces to sense single molecular are also emerging. Plasmonic metasurfaces as a planarized platform can be used to study enormous possibilities for surface chemistry, such as molecular structures and dynamic interactions. These lead to ultrasensitive single molecular sensing, which is not just based on the surface enhancement Raman scattering, or the strong field confinement/localization, or the high sensitivity of tuning its frequencies due to dielectric constant variation from environmental change, but it could be related to high sensitivity of certain mode of the metasurfaces, such as Fano resonance metasurface [7],[8].

9.3 REFERENCES

[1] Lu, Y. J. et al. Plasmonic Nanolaser Using Epitaxially Grown Silver Film. Science 337, 450-453, (2012).

[2] Li, B. H. et al. Contrast between Surface Plasmon Polariton-Mediated Extraordinary Optical Transmission Behavior in Epitaxial and Polycrystalline Ag Films in the Mid- and Far-Infrared Regimes. Nano Letters 12, 6187-6191, (2012).

[3] G.V. Naik, J. Liu, A. V. Kildishev, V. M. Shalaev, A. Boltasseva. Demonstration of Al:ZnO as a plasmonic component of near-infrared metamaterials. Proceedings of the National Academy of Sciences 109, 8834-8838 (2012).

[4] West, P. R. et al. Searching for better plasmonic materials. Laser and Photonics Reviews 4, 795-808, (2010).

[5] G. V. Naik, J. Kim, A. Boltasseva. Oxides and nitrides as alternative plasmonic materials in the optical range. Optical Materials Express 1 (6), 1090-1099 (2011).

[6] A. Boltasseva and H. Atwater. Low-loss plasmonic metamaterials. Science Perspective, Science 331, 290-291 (2011).

[7] S. H. Mousavi, I. N. Kholmanov, K. B. Alici, D. Purtseladze, N. Arju, K. Tatar, D. Y. Fozdar, J. W. Suk, Y. Hao, A. B. Khanikaev, R. S. Ruoff, and G. Shvets. Inductive Tuning of Fano-Resonant Meta-Surfaces Using Plasmonic Response of Graphene in Mid-Infrared. Nano Letters 13, 1111-1117, (2013).

[8] Wu, C. H. et al. Fano-resonant asymmetric metamaterials for ultrasensitive spectroscopy and identification of molecular monolayers. Nature Materials 11, 69-75, (2012).

Bibliography

Adato, R.; Yanik, A. A.; Altug, H. Nano Lett. 11, (12), 5219-5226, (2011).

Agio, M. and Alù, A. (eds.) Optical Antennas. Cambridge University Press 2012.

Alù, A. and Engheta, N. Achieving Transparency with Plasmonic and Metamaterial Coatings, Phys. Rev. E 72, 016623 (2005).

Alù, A. and Engheta, N. Polarizabilities and effective parameters for collections of spherical nano-particles formed by pairs of concentric double-negative (dng), single-negative (sng) and/or double-positive (dps) metamaterial layers, J. Appl. Phys. 97, 094310 (2005).

Alù, A., and Engheta, N. Optical nano-transmission lines: synthesis of planar left-handed metamaterials in the infrared and visible regimes. J. Opt. Soc. Am. B 23, 571-583 (2006).

Alù, A. and Engheta, N. Three-dimensional nanotransmission lines at optical frequencies: A recipe for broadband negative-refraction optical metamaterials. Phys. Rev. B 75, 024304 (2007).

Alù, A.; Salandrino, A. and Engheta, N. Parallel, series, and intermediate interconnections of optical nanocircuit elements. 2. Nanocircuit and physical interpretation, J. Opt. Soc. Am. B 24, 3014-3022 (2007).

Alù, A. and Engheta, N. Plasmonic and metamaterial cloaking: physical mechanisms and potentials. Journal of Optics A-Pure and Applied Optics 10, (2008).

Alù, A. and Engheta, N. Input impedance, nanocircuit loading, and radiation tuning of optical nanoantennas, Phys. Rev. Lett. 101, 043901 (2008).

Alù, A., and Engheta, N. Tuning the scattering response of optical nanoantennas with nanocircuit loads, Nature Photonics, 2, pp. 307-310 (2008).

Alù, A., and Engheta, N. Hertzian plasmonic nanodimer as an efficient optical nanoantenna, Phys. Rev. B 78, 195111 (2008).

Alù, A., Mantle cloak: Invisibility induced by a surface, Physical Review B, 80, pp. 245115 (2009).

Alù, A. and Engheta, N. On certain design criteria for nanoantennas in the visible, J. of Comput. Theor. Nanos. 6, 2009-2015 (2009).

Alù, A. and Engheta, N. Optical nanoswitch: an engineered plasmonic nanoparticle with extreme parameters and giant anisotropy, New J. Phys. 11, 013026 (2009).

Alù, A. and Engheta, N. Wireless at the nanoscale: optical interconnects using matched nanoantennas, Phys. Rev. Lett. 104, 213902 (2010).

Alù, A., Yaghjian, A. D.; Shore, R. A.; Silveirinha, M. G. Phys. Rev. B 84, 054305 (2011).

Anger, P.; Bharadwaj, P. and Novotny, L. Enhancement and quenching of single-molecule fluorescence, Phys. Rev. Lett. 96, 113002 (2006).

Anker, J. N.; Hall, W. P.; Lyandres, O.; Shah, N.C; Zhao, J. and Van Duyne, R.P. Biosensing with plasmonic nanosensors, Nat. Mater. 7, 442-453 (2008).

Atay, T.; Song, J. H.; Nurmikko, A. V. Nano Lett. 4, (9), 1627-1631 (2004).

Auguie, B.; Barnes, W. L. Phys. Rev. Lett. 101, 143902 (2008).

Bai, B.; Svirko,Y.; Turunen, J. and Vallius, T. Optical activity in planar chiral metamaterials: Theoretical study. Phys. Rev. A 76, 023811 (2007).

Baida, F. I.; Boutria, M.; Oussaid, R.; Van Labeke, D. Phys. Rev. B 84, 035107 (2011).

Bakker, R.; Boltasseva, M. A.; Liu, Z.; Pedersen, R. H.; Gresillon, S.; Kildishev, A. V.; Drachev, V. P. and Shalaev, V. M. Near-field excitation of nanoantenna resonance, Opt. Express 15, 13682-13688 (2007).

Bakker, R. M.; Yuan, H.-K.; Liu, Z.; Drachev, V. P.; Kildishev, A. V. and Shalaev, V. M. Enhanced localized fluorescence in plasmonic nanoantennae, Appl. Phys. Lett. 92, 043101 (2008).

Becker, J. W.; Reeke, G. N.; Wang, J. L.; Cunningham, B. A. and Edelman, G. M. The covalent and three dimensional structure of Concanavalin A, J. Bio. Chem. 250, 1513-1524 (1975).

Bek, A.; Jansen, R.; Ringler, M.; Mayilo, S.; Klar, T. A. and Feldmann, J. "Fluorescence enhancement in hot spots of afm-designed gold nanoparticle sandwiches," Nano Lett. 8, 485-490 (2008).

Belov, P. A.; Maslovski, S. I.; Simovski, K. R. and Tretyakov, S. A. Technical Phys. Lett. 29, 718 (2003).

Berthelot, J.; Bouhelier, A.; Huang, C. J.; Margueritat, J.; Colas-des-Francs, G.; Finot, E.; Weeber, J. C.; Dereux, A.; Kostcheev, S.; El Ahrach, H. I.; Baudrion, A. L.; Plain,

J.; Bachelot, R.; Royer, P.; Wiederrecht, G. P. Nano Lett. 9, (11), 3914-3921 (2009).

Beruete, M.; Sorolla, M.; Marques, R.; Baena, J. D. and Freire, M. Electromagnetics 26, 247 (2006).

Beruete, M.; Navarro-Cia, M.; Falcone, F.; Campillo, I. and Sorolla, M. Single negative birefringence in stacked spoof plasmon metasurfaces by prism experiment, Optics Letters, 35, pp. 643-645 (2010).

Bharadwaj, P.; Deutsch, B. and Novotny, L. Optical antennas, Adv. Opt. Photon. 1, 438-483 (2009).

Biagioni, P.; Huang, J. S.; Duo, L.; Finazzi, M. and Hecht, B. Phys. Rev. Lett. 102, 256801 (2009).

Bohren, C. F. and Huffman, D. R. Absorption and scattering of light by small particles. (John Wiley & Sons, Inc., 1983).

Boltasseva, A. and Atwater, H. Low-loss plasmonic metamaterials. Science Perspective, Science 331, 290-291 (2011).

Born, M., and Wolf, E. Principles of Optics, 7th ed., New York: Cambridge University Press, 1999.

Bose, J. C. On the rotation of plane of polarisation of electric waves by a twisted structure, Proceedings of the Royal Society 63, pp. 146-152 (1898).

Broer, D. J.; Lub, J. and Mol, G. N. Wide-band reflective polarizers from cholesteric polymer networks with a pitch gradient. Nature 378, 467-469 (1995).

Brueck, S.R.J. Optical and interferometric lithography - Nanotechnology enablers, Proceedings of the IEEE, 93, pp. 1704-1721 (2005).

Burokur, S.N.; Daniel, J.P.; Ratajczak, P. and de Lustrac, A. Tunable bilayered metasurface for frequency reconfigurable directive emissions, Applied Physics Letters, 97, pp. 064101 (2010).

Cai, W. and Shalaev, V. M. Optical Metamaterials: Fundamentals and Applications. (Springer, 2009).

Cai, W. S.; Chettiar, U. K.; Kildishev, A. V. and Shalaev, V. M. Optical cloaking with metamaterials. Nature Photonics 1, 224-227, (2007).

Chen, H. Y.; Chan, C. T. and Sheng, P. Transformation optics and metamaterials. Nature Materials 9, 387-396, (2010).

Chen, P.Y., and Alù, A. Subwavelength Imaging Using Phase-Conjugating Nonlinear Nanoantenna Arrays, Nano Letters, 11, pp. 5514-5518 (2011).

Chiou, T.H.; Kleinlogel, S.; Cronin, T.; Caldwell, R.; Loeffler, B.; Siddiqi, A.; Goldizen, A., and Marshall, J. Circular polarization vision in a stomatopod crustacean, Current Biology, 18, pp. 429-434 (2008).

Choulis, S. A.; Mathai, M. K. and Choong, V. E. Influence of metallic nanoparticles on the performance of organic electrophosphorescence devices, Appl. Phys. Lett. 88, 213503 (2006).

Collin, R. E. Field Theory of Guided Waves, second ed., Wiley-IEEE Press, New York, 1990.

Cronin, T. W.; Shashar, N.; Caldwell, R. L.; Marshall, J.; Cheroske, A. G.; Chiou, T. H. Integr. Comp. Biol. 43,, 549-558 (2003).

CST Microwave Studio 2010, CST of America, Inc., www.cst.com

Curto, A. G.; Volpe, G.; Taminiau, T. H.; Kreuzer, M. P.; Quidant, R.; van Hulst, N. F. Science 329, pp. 930-933 (2010).

Dawes, D. H.; McPhedran, R. C. and Whitbourn, L. B. Appl. Optics 28, 3498 (1989).

De Vries, H. Rotatory power and other optical properties of certain liquid crystals. Acta Cryst. 4, 219-226 (1951).

Decker, M. *et al*. Strong optical activity from twisted-cross photonic metamaterials. Opt. Lett. 34, 2501-2503 (2009).

Decker, M.; Klein, M.W.; Wegener, M. and Linden, S. Circular dichroism of planar chiral magnetic metamaterials, Optics Letters, 32, pp. 856-858 (2007).

Demetriadou, A., and Pendry, J.B. Extreme chirality in Swiss roll metamaterials, Journal of Physics-Condensed Matter 21, pp. 376003 (2009).

Deubel, M.; Von Freymann, G., Wegener, M.; Pereira, S.; Busch, K., and Soukoulis, C.M. Direct laser writing of three-dimensional photonic-crystal templates for telecommunications, Nature Materials, 3, pp. 444-447 (2004).

Dolling, G.; Enkrich, C.; Wegener, M.; Soukoulis, C.M. and Linden, S. Simultaneous negative phase and group velocity of light in a metamaterial, Science, 312, pp. 892-894 (2006).

Drezet, C.; Genet and Ebbesen, T. W. Phys. Rev. Lett. 101, 043902 (2008).

Ekinci, Y.; Solak, H. H.; David, C; Sigg, H. Opt. Express 14, 2323-2334 (2006).

Ellenbogen, T.; Seo, K.; Crozier, K. B. Nano Lett. 12, 1026-1031 (2012).

Engheta, N.; Salandrino, A. and A. Alù, Circuit elements at optical frequencies: nanoinductors, nanocapacitors, and nanoresistors, Phys. Rev. Lett. 95, 095504 (2005).

Engheta, N. Circuits with light at nanoscales: optical nanocircuits inspired by metamaterials, Science 317, 1698-1702 (2007).

Falcone, T.; Lopetegi, M. A.; Laso, G.; Baena, J. D.; Bonache, J.; Beruete, M.; Marqués, R.; Martín, F. and Sorolla, M. Phys. Rev. Lett. 93, 197401 (2004).

Fang, N.; Lee, H.; Sun, C. and Zhang, X. Sub-diffraction-limited optical imaging with a silver superlens, Science, 308, pp. 534-537 (2005).

Farahani, J. N.; Pohl, D. W.; Eisler, H. J. and Hecht, B. "Single quantum dot coupled to a scanning optical antenna: A tunable superemitter," Phys. Rev. Lett. 95, 017402 (2005).

Fedotov, V. A.; Schwanecke, A. S.; Zheludev, N. I.; Khardikov, V. V.; Prosvirnin, S. L. Nano Lett. 7, 1996-1999 (2007).

Feng, L.; Liu, Z.; Lomakin, V.; Fainman, Y. Appl. Phys. Lett. 96, 041112 (2010).

Frey, H. G.; Witt, S.; Felderer, K. and Guckenberger, R. High-resolution imaging of single fluorescent molecules with the optical near-field of a metal tip, Phys. Rev. Lett. 93, 200801 (2004).

Fung, C. K.; Xi, M. N.; Shanker, B.; Lai, K. W. C. and Chen, H. Dipole and bowtie antenna for carbon nanotube (CNT) based infrared sensors, in Proceedings of IEEE Conference on Nanotechnology Materials and Devices (IEEE, 2009), pp. 87–90 (2009).

Gansel, J.K.; Thiel, M.; Rill, M.S.; Decker, M.; Bade, K.; Saile, V.; von Freymann, G.; Linden, S. and Wegener, M. Gold Helix Photonic Metamaterial as Broadband Circular Polarizer, Science 325, pp. 1513-1515 (2009).

Garcia-Parajo, M. F. Optical antennas focus in on biology, Nat. Photonics 2, 201-203 (2008).

Garcia-Vidal, F. J.; Martin-Moreno, L.; Pendry, J. B. Surfaces with holes in them: new plasmonic metamaterials, J. Opt. A: Pure Appl. Opt. 7 S97-S101 (2005).

Gordon, J.A.; Holloway, C.L. and Dienstfrey, A. A physical explanation of angle-independent reflection and transmission properties of metafilms/metasurfaces, IEEE Antennas and Wireless Propagation Letters, 8, pp. 1127-1130 (2009).

Greffet, J. J. Nanoantennas for light emission, Science 308, 1561-1563 (2005).

Greffet, J. J.; Laroche, M.; Marquier, F. Phys. Rev. Lett. 105, (11), 117701 (2010).

Gruev, V., R. Perkins, and T. York, Opt. Express 18, 19087 (2010).

Guerrero-Martinez, A. *et al*. Intense optical activity from three-dimensional chiral ordering of plasmonic nanoantennas. Angew. Chem. Int. Ed. 50, 5499-5503 (2011).

Henzie, J.; Lee, M.H. and Odom, T.W. Multiscale patterning of plasmonic metamaterials, Nature Nanotechnology, 2, pp. 549-554 (2007).

Holloway, C. L. *et al*. An Overview of the Theory and Applications of Metasurfaces: The Two-Dimensional Equivalents of Metamaterials. Ieee Antennas and Propagation Magazine 54, 10-35, (2012).

Holloway, C.L.; Deinstfrey, A.; Kuester, E.F.; O'Hara,J. F.; Azad, A. K.; Taylor, A. J. A discussion on the interpretation and characterization of metafilms-metasurfaces: the twodimensional equivalent of metamaterials, Metamaterials 3, 100–112 (2009).

Holloway, C.L. P. Kabos, M.A. Mohamed, E.F. Kuester, J.A. Gordon, M.D. Janezic, J. Baker-Jarvis, Realisation of a controllable metafilm/metasurface composed of resonant magnetodielectric particles: measurements and theory, IET Microw. Antennas Propag. 4, 1111–1122 (2010).

Holloway, C.L.; Mohamed, M.A.; Kuester, E.F. and Dienstfrey, A. Reflection and transmission properties of a metafilm: With an application to a controllable surface composed of resonant particles, IEEE Transactions on Electromagnetic Compatibility, 47, pp. 853-865 (2005).

Hsu, S.-Y.; Lee, K.-L.; Lin, E.-H.; Lee, M.-C. and Wei, P.-K. Appl. Phys. Lett. 95, 013105 (2009).

Huang, F. M.; Baumberg, J. J. Nano Lett. 2010, 10, (5), 1787-1792, (2009).

Huang, J. S.; Feichtner, T.; Biagioni, P.; Hecht, B. Nano Lett. 9, (5), 1897-1902 (2009).

Huang, W.-X.; Zhang, Y.; Tang,X.-M.; Cai, L.-S.; Zhao, J.-W.; Zhou, L.; Wang, Q.-J.; Huang,C.-P. and Zhu, Y.-Y. Opt. Lett. 36, 3359 (2011).

Huang, Y. H.; Zhou, Y. and Wu, S. T. Broadband circular polarizer using stacked chiral polymer films. Opt. Express 15, 6414-6419 (2007).

Jen, Y.-J.; Lakhtakia, A.; Yu, C.-W.; Lin, C.-F.; Lin, M.-J.; Wang, S.-H.; Lai, J.-R. Biologically inspired achromatic waveplates for visible light. Nat. Commun.2, 363 (2011).

Johnson, P.B. and Christy, R.W. Optical constants of noble metals, Physical Review B, 6, pp. 4370-4379 (1972).

Jung, L. S.; Campbell, C. T.; Chinowsky, T. M.; Mar, M. N. and Yee, S. S. Quantitative interpretation of the response of surface plasmon resonance sensors to adsorbed films , Langmuir 14, 5636-5648 (1998).

Kats, M. A.; Genevet, P.; Aoust, G.; Yu, N.; Blanchard, R.; Aieta, F.; Gaburro, Z.; Capasso, F. PNAS 2012, 109, 12364-12368.

Khoo, E. H.; Li, E. P. and Crozier, K. B. Opt. Lett. 36, 2498(2011).

Kildishev, A.; Boltasseva, A. and Shalaev, V. Planar Photonics with Metasurfaces. Science 339, 1232009, (2013).

Kinkhabwala, A.; Yu, Z. F.; Fan, S. H.; Avlasevich,Y.; Mullen, K. and Moerner, W. E. Large single-molecule fluorescence enhancements produced by a bowtie nanoantenna, Nat. Photonics 3, 654-657 (2009).

Kobayashi, N. P.; Islam, M. S.; Wu, W.; Chaturvedi, P.; Fang, N. X.; Wang, S. Y.; Williams, R. S. Nano Lett. 9, 178-182 (2009).

Koenderink, A. F. Plasmon nanoparticle array waveguides for single photon and single plasmon sources, Nano Lett. 9, 4228-4233 (2009).

Kopp, V.I. *et al*. Chiral fiber gratings. Science 305, 74-75 (2004).

Kuester, E.F.; Mohamed, M.A.; Piket-May, M. and Holloway, C.L. Averaged transition conditions for electromagnetic fields at a metafilm, IEEE Transactions on Antennas and Propagation, 51, pp. 2641-2651 (2003).

Kuwata-Gonokami, M.; Saito, N.; Ino, Y.; Kauranen, M.; Jefimovs, K.; Vallius, T.; Turunen, J. and Svirko, Y. Giant optical activity in quasi-two-dimensional planar nanostructures, Physical Review Letters, 95, pp. 227401(2005).

Lakhtakia, A. Anomalous axial propagation in helicoidal bianisotropic media. Opt. Comm. 157, 193-201 (1998).

Landy, N.I.; Sajuyigbe, S.; Mock, J.J.; Smith, D.R. and Padilla, W.J. Perfect metamaterial absorber, Physical Review Letters, 100, pp. 207402 (2008).

Large, N.; Abb, M.; Aizpurua, J.; Muskens, O. L. Nano Lett. 10, (5), 1741-1746 (2010).

Lee, K.S.; Yang, D.Y.; Park, S.H. and Kim, R.H. Recent developments in the use of two-photon polymerization in precise 2D and 3D microfabrications, Polymers for Advanced Technologies, 17, pp. 72-82 (2006).

Leonhardt, U. Optical conformal mapping, Science 312, pp. 1777-1780 (2006).

Lezec, H.J.; Dionne, J.A. and Atwater, H.A. Negative refraction at visible frequencies, Science, 316, pp. 430-432 (2007).

Li, B. H. *et al*. Contrast between Surface Plasmon Polariton-Mediated Extraordinary Optical Transmission Behavior in Epitaxial and Polycrystalline Ag Films in the Mid- and Far-Infrared Regimes. Nano Letters 12, 6187-6191, (2012).

Li, T.; Liu, H.; Wang, S.-M.; Yin, X.-G.; Wang, F.-M.; Zhu, S.-N.; Zhang, X. Appl. Phys. Lett. 93, 021110 (2008).

Linden, S.; Enkrich, C.; Wegener, M.; Zhou, J.F.; Koschny, T. and Soukoulis, C.M. Magnetic response of metamaterials at 100 terahertz, Science, 306, pp. 1351-1353 (2004).

Liu, N. *et al*. Individual Nanoantennas Loaded with Three-Dimensional Optical Nanocircuits. Nano Letters 13, 142-147, (2013).

Liu, N.; Guo, H.C.; Fu, L.W.; Kaiser, S.; Schweizer, H. and Giessen, H. Three-dimensional photonic metamaterials at optical frequencies, Nature Materials, 7, pp. 31-37 (2008).

Liu, N.; Langguth, L.; Weiss, T.; Kastel, J.; Fleischhauer, M.; Pfau, T., and Giessen, H. Plasmonic analogue of electromagnetically induced transparency at the Drude damping limit, Nature Materials, 8, pp. 758-762 (2009).

Liu, N.; Liu, H.; Zhu, S. and Giessen, H. Stereometamaterials. Nat. Photonics 3, 157-162 (2009).

Liu, X.-X. and Zhao, Y., Determination of full dynamic polarizability tensor of arbitrary sub-wavelength inclusions in meta-arrays, under review.

Liu, Z.; Boltasseva, A.; Pedersen, R. H.; Bakker, R.; Kildishev, A. V.; Drachev, V. P. and Shalaev, V. M. Plasmonic nanoantenna arrays for the visible, Metamaterials 2, 45-51 (2008).

Lu, Y. J. *et al*. Plasmonic Nanolaser Using Epitaxially Grown Silver Film. Science 337, 450-453, (2012).

Luk'yanchuk, B. *et al*. The Fano resonance in plasmonic nanostructures and metamaterials. Nature Materials 9, 707-715, (2010).

Luukkonen, A.; Simovski, C.; Granet, G.; Goussetis,G.; Lioubtchenko, D.; Raisanen, A. V. and Tretyakov, S. A. IEEE Trans. Antennas Propag. 56, 1624 (2008).

Lythgoe, J. N.; Hemmings, C. C. Nature 213, 893-894 (1967).

Maier, S. A. Plasmonics: fundamentals and applications. (Springer, 2007).

Maier, S. A.; Atwater, H. A. Plasmonics: Localization and guiding of electromagnetic energy in metal/dielectric structures, Journal of Applied Physics, 98, pp. 011101 (2005).

Maier, S. A.; Brongersma, M. L.; Kik, P. G.; Meltzer, S.; Requicha, A. A. G.; Atwater, H. A. Plasmonics-A route to nanoscale optical devices, Advanced Materials, 13, pp. 1501-1505 (2001).

Maradudin, A. A. Structured Surfaces as Optical Metamaterials, eds. Alù, A., and Engheta, N., Chapter 3 "Optical Wave Interaction with Two-Dimensional Arrays of Plasmonic Nanoparticles" (Cambridge University Press, New York) pp. 58-93 (2011).

Marques, R.; Mesa, F.; Martel, J. and Medina, F. IEEE Trans. on Antennas and Propagation 51, 2572 (2003).

Maruo, S.; Nakamura, O. and Kawata, S. Three-dimensional microfabrication with two-photon-absorbed photopolymerization. Opt. Lett. 22, 132-134 (1997).

Mertens, H. J.; Biteen, S.; Atwater, H. A. and Polman, A. Polarization-selective plasmon-enhanced silicon quantum-dot luminescence, Nano Lett. 6, 2622-2625 (2006).

Mosallaei, H.; Sarabandi, K. A one-layer ultra-thin meta-surface absorber, Antennas and Propag. Soc. Int. Symp., IEEE1B pp.615-618 (2005).

Mousavi, S. H.; Kholmanov, I. N.; Alici, K. B.; Purtseladze, D.; Arju, N.; Tatar, K.; Fozdar, D. Y.; Suk, J. W.; Hao, Y.; Khanikaev, A. B.; Ruoff, R. S. and Shvets. G. Inductive Tuning of Fano-Resonant Meta-Surfaces Using Plasmonic Response of Graphene in Mid-Infrared. Nano Letters 13, 1111-1117, (2013).

Muhlschlegel, P. H.; Eisler, J.; Martin, O. J. F.; Hecht, B. and Pohl, D. W. Resonant optical antennas, Science 308, 1607-1609 (2005).

Munk, B. A., Frequency Selective Surfaces: Theory and Design, first ed., Wiley, New York, 2000.

Naik, G. V.; Kim, J.; Boltasseva. A. Oxides and nitrides as alternative plasmonic materials in the optical range. Optical Materials Express 1 (6), 1090-1099 (2011).

Naik, G.V.; Liu, J.; Kildishev, A. V.; Shalaev, V. M.; Boltassev, A. Demonstration of Al:ZnO as a plasmonic component of near-infrared metamaterials. Proceedings of the National Academy of Sciences 109, 8834-8838 (2012).

Neubrech, F.; Pucci, A.; Cornelius, T. W.; Karim, S.; Garcia-Etxarri, A. and Aizpurua, J. Resonant plasmonic and vibrational coupling in a tailored nanoantenna for infrared detection, Phys. Rev. Lett. 101, 157403 (2008).

Novotny, L. Effective wavelength scaling for optical antennas, Phys. Rev. Lett. 98, 266802 (2007).

Novotny, L. and van Hulst, N. Antennas for light. Nature Photonics 5, 83-90, (2011).

Luukkonen, O.; Simovski, C.; Granet, G.; Goussetis, G.; Lioubtchenko, D.; Raisanen, A. V. and Tretyakov, S. A. Simple and Accurate Analytical Model of Planar Grids and High-Impedance Surfaces Comprising Metal Strips or Patches, IEEE Trans. Antennas Propag. 58, 2162-2162 (2010).

Ogut, E.; Sendur, K. Appl. Phys. Lett. 96, 141104 (2010).

Okamoto, K.; Niki, I.; Shvartser, A.; Narukawa, Y.; Mukai, T. and Scherer, A. Surface-plasmon-enhanced light emitters based on InGaN quantum wells, Nat. Mater. 3, 601-605 (2004).

Oseen, C. W. The theory of liquid crystals. Trans. Faraday Soc. 29, 883-899 (1933).

Ozbay, E. Plasmonics: Merging photonics and electronics at nanoscale dimensions, Science, 311, pp. 189-193 (2006).

Papakostas, A.; Potts, A.; Bagnall, D. M.; Prosvirnin, S. L.; Coles, H. J.; Zheludev, N. I. Phys. Rev. Lett. 90, 107404 (2003).

Papasimakis, N.; Fedotov, V.A.; Zheludev, N.I. and Prosvirnin, S.L. Metamaterial Analog of Electromagnetically Induced Transparency, Physical Review Letters, 101, pp. 253903 (2008).

Pendry, J. B.; Schurig, D.; Smith, D. R. Controlling Electromagnetic Fields, Science 312, 1780-1782 (2006).

Pendry, J. B. Negative refraction makes a perfect lens, Phys. Rev. Lett. 85, 3966-3969 (2000).

Pendry, J. B. Negative refraction. Contemporary Physics 45, 191-202, (2004).

Plum, E.; Fedotov, V. A.; Schwanecke, A. S.; Zheludev, N. I. and Chen, Y. Giant optical gyrotropy due to electromagnetic coupling. Appl. Phys. Lett. 90, 223113 (2007).

Plum, E.; Liu, X.X.; Fedotov, V.A.; Chen, Y.; Tsai, D.P. and Zheludev, N.I. Metamaterials: Optical Activity without Chirality, Physical Review Letters, 102, pp. 113902 (2009).

Plum, E.; Zhou, J.; Dong, J.; Fedotov, V.A.; Koschny, T.; Soukoulis, C.M. and Zheludev, N.I. Metamaterial with negative index due to chirality, Physical Review B, 79, pp. 035407 (2009).

Pors, A.; Nielsen, M. G.; Della Valle, G.; Willatzen, M.; Albrektsen, O. and Bozhevolnyi, S. I. Opt. Lett. 36, 1626 (2011).

Pozar, D. M. Microwave Engineering. (John Wiley & Sons, 2012).

Raether, H. Surface plasmons on smooth and rough surfaces and on gratings (Springer, Berlin, 1988).

Roberts, N.W.; Chiou, T.H.; Marshall, N.J. and Cronin, T.W. A biological quarter-wave retarder with excellent achromaticity in the visible wavelength region, Nature Photonics, 3, pp. 641-644 (2009).

Rockstuhl, C.; Lederer, F.; Etrich, C.; Pertsch, T. and Scharf, T. Design of an artificial three-dimensional composite metamaterial with magnetic resonances in the visible range of the electromagnetic spectrum, Physical Review Letters, 99, pp. 017401 (2007).

Rockstuhl, C.; Zentgraf, T.; Meyrath, T. P.; Giessen, H. and Lederer, F. Opt. Express 16, 2080 (2008).

Rogacheva, A. V.; Fedotov, V. A.; Schwanecke, A. S. and Zheludev, N. I. Giant gyrotropy due to electromagnetic-field coupling in a bilayered chiral structure. Phys. Rev. Lett. 97, 177401 (2006).

Sarid, D. and Challener, W. Modern instroduction to surface plasmons. (Cambridge University Press, 2010).

Sarkar, T.K., and Sengupta, D.L. An appreciation of J. C. Bose's pioneering work in millimeter waves, IEEE Antennas and Propagation Magazine, 39, pp. 55-63 (1997).

Schnell, M.; Garcia-Etxarri, A.; Huber, A. J.; Crozier, K.; Aizpurua, J.; Hillenbrand, R. Nat. Photonics 3, (5), 287-291 (2009).

Schuck, P. J.; Fromm, D. P.; Sundaramurthy, A.; Kino, G. S. and Moerner, W. E. Improving the mismatch between light and nanoscale objects with gold bowtie nanoantennas, Phys. Rev. Lett. 94, 017402 (2005).

Schurig, D.; Mock, J.J.; Justice, B.J.; Cummer, S.A.; Pendry, J.B.; Starr, A.F. and Smith, D.R. Metamaterial electromagnetic cloak at microwave frequencies, Science, 314, pp. 977-980 (2006).

Schwind, R. Polarization vision in water insects and insects living on a moist substrate, Journal of Comparative Physiology a-Sensory Neural and Behavioral Physiology, 169, pp. 531-540 (1991).

Seet, K.K.; Mizeikis, V.; Matsuo, S.; Juodkazis, S. and Misawa, H. Three-dimensional spiral-architecture photonic crystals obtained by direct laser writing, Advanced Materials, 17, pp. 541-545 (2005).

Serdyukov, A.N.; Semchenko, I.V.; Tretyakov, S.A. and Sihvola, A. Electromagnetics of Bi-anisotropic Materials: Theory and Applications (Gordon and Breach, Amsterdam) (2001)

Sersic, I.; Tuambilangana, C.; Kampfrath, T. and Koenderink, A.F. Magnetoelectric point scattering theory for metamaterial scatterers, Physical Review B, 83, pp. 245102 (2011).

Shalaev, V. M. *et al*. Negative index of refraction in optical metamaterials. Optics Letters 30, 3356-3358, (2005).

Shalaev, V. M. Optical negative-index metamaterials. Nat. Photonics 1, 41-48 (2007).

Shashar, N.; Rutledge, P.S. and Cronin, T.W. Polarization vision in cuttlefish - A concealed communication channel, Journal of Experimental Biology, 199, pp. 2077-2084 (1996).

Shelby, R. A.; Smith, D. R.; Schultz, S. Experimental verification of a negative index of refraction, Science 292 77-79 (2001).

Silveirinha, M. G. Phys. Rev. E 73, 046612 (2006).

Simovski, C. R. Analytical modelling of double-negative composites, Metamaterials 2, 169-185 (2008).

Smith, D. R. Analytic expressions for the constitutive parameters of magnetoelectric metamaterials, Phys. Rev. E 81, 036605 (2010).

Smith, D.R.; Pendry, J.B. and Wiltshire, M.C.K. Metamaterials and negative refractive index, Science, 305, pp. 788-792 (2004).

Soukoulis, C. M. and Wegener, M. Past achievements and future challenges in the development of three-dimensional photonic metamaterials. Nature Photonics 5, 523-530, (2011).

Soukoulis, C. M.; Kafesaki, M. and Economou, E. N. Negative-index materials: New frontiers in optics. Advanced Materials 18, 1941-1952, (2006).

Soukoulis, C.M.; Linden, S. and Wegener, M. Negative refractive index at optical wavelengths, Science, 315, pp. 47-49 (2007).

Sparks, W. B.; Hough, J.; Germer, T. A.; Chen, F.; DasSarma, S.; DasSarma, P.; Robb, F. T.; Manset, N.; Kolokolova, L.; Reid, N.; Macchetto, F. D.; Martin, W. PNAS 106, 7816-7821 (2009).

Sun, H.; Chen, A. and Dalton, L.R. Enhanced evanescent confinement in multiple-slot waveguides and its application in biochemical sensing, IEEE Photonics. J. 1, 48-57 (2009).

Sun, Y.; Edwards, B.; Alù, A. and Engheta, N. Experimental realization of optical lumped nanocircuits at infrared wavelengths, Nature Materials, 11, pp. 208-212 (2012).

Sundaramurthy, A.; Schuck, P. J.; Conley, N. R.; Fromm, D. P.; Kino, G. S. and Moerner, W. E. Toward nanometer-scale optical photolithography: Utilizing the near-field of bowtie optical nanoantennas, Nano Lett. 6, 355-360 (2006).

Taminiau, T. H.; Moerland, R. J.; Segerink, F. B.; Kuipers, L. and van Hulst, N. F. lambda/4 Resonance of an optical monopole antenna probed by single molecule fluorescence, Nano Lett. 7, 28-33 (2007).

Taminiau, T. H.; Stefani, F. D.; Segerink, F. B.; Van Hulst, N. F. Nat. Photonics 2, (4), 234-237 (2008).

Tsakmakidis, K.L.; Boardman, A.D. and Hess, O. Trapped rainbow' storage of light in metamaterials, Nature, 450, pp. 397-401 (2007).

Valentine, J.; Zhang, S.; Zentgraf, T.; Ulin-Avila, E.; Genov, D.A.; Bartal, G. and Zhang, X. Three-dimensional optical metamaterial with a negative refractive index, Nature, 455, pp. 376-379 (2008).

Van Orden, D.; Fainman, Y. and Lomakin, V. Twisted chains of resonant particles: optical polarization control, waveguidance, and radiation. Opt. Lett. 35, 2579-2581 (2010).

Viitanen, A. J.; Hanninen, I.; Tretyakov, S. A. Analytical model for regular dense arrays of planar dipole scatterers, Prog. in Electromagn. Res. 38, 97-110 (2002).

Wei, Z.; Cao, Y.; Fan, Y.; Yu, X., and Li, H. Broadband polarization transformation via enhanced asymmetric transmission through arrays of twisted complementary split-ring resonators, Applied Physics Letters, 99, pp. 221907 (2011).

West, P. R. *et al*. Searching for better plasmonic materials. Laser & Photonics Reviews 4, 795-808, (2010).

Wu, C. H. *et al.* Fano-resonant asymmetric metamaterials for ultrasensitive spectroscopy and identification of molecular monolayers. Nature Materials 11, 69-75, (2012).

Yaroslavsky, A. N.; Neel, V.; Anderson, R. R. J. Invest. Dermatol. 121, 259-266 (2003).

Yu, N.; Genevet, P.; Kats, M. A.; Aieta, F.; Tetienne, J. P.; Capasso, F.; Gaburro, Z. Science, in press (2011).

Yu, N.; Aieta, F.; Genevet, P.; Kats, M. A.; Gaburro, Z.; Capasso, F. Nano Lett., ASAP (2012).

Zentgraf, T.; Meyrath, T. P.; Seidel, A.; Kaiser, S.; Giessen, H.; Rockstuhl, C. and Lederer, F. Phys. Rev. B 76, 033407 (2007).

Zhang, S. *et al.* Experimental demonstration of near-infrared negative-index metamaterials. Physical Review Letters 95, (2005).

Zhang, S.; Fan, W.J.; Panoiu, N.C.; Malloy, K.J.; Osgood, R.M. and Brueck, S.R.J. Experimental demonstration of near-infrared negative-index metamaterials, Physical Review Letters, 95, pp. 137404 (2005).

Zhang, S.; Zhou, J.; Park, Y.-S.; Rho, J.; Singh, R.; Nam, S.; Azad, A.K.; Chen, H.-T.; Yin, X.; Taylor, A.J. and Zhang, X. Photoinduced handedness switching in terahertz chiral metamolecules, Nature Communications, 3, pp. 942 (2012).

Zhang, S.; Genov, D. A.; Wang, Y.; Liu, M.; Zhang, X. Phys. Rev. Lett. 101, 047401 (2008).

Zhao, Y. and Alù, A. Tailoring the Dispersion of Plasmonic Nanorods To Realize Broadband Optical Meta-Waveplates. Nano Letters 13, 1086, (2013).

Zhao, Y. and Alù, A. Manipulating light polarization with ultrathin plasmonic metasurfaces. Phys. Rev. B 84, 205428 (2011).

Zhao, Y., Alù, A. An Ultrathin Quarter-Wave Nano-Plate Based on Detuned Plasmonic Nanoantennas. In IEEE Antennas and Propagation Society International Symposium (2012).

Zhao, Y.; Belkin, M.A., and Alù, A. Twisted optical metamaterials for planarized ultrathin broadband circular polarizers, Nature Communications, 3, pp. 870 (2012).

Zhao, Y.; Engheta, N. and Alù, A. Effects of shape and loading of optical nanoantennas on their sensitivity and radiation properties. Journal of the Optical Society of America B-Optical Physics 28, 1266-1274, (2011).

Zhao, Y.; Engheta, N. and Alù, A. Homogenization of plasmonic metasurfaces modeled as transmission-line loads. Metamaterials 5, 90-96 (2011).

Zharov, A. A.; Shadrivov, I.V. and Kivshar, Y.S. Nonlinear properties of left-handed metamaterials, Physical Review Letters, 91, pp. 037401 (2003).

Zhou, J.; Dong, J.; Wang, B.; Koschny, T.; Kafesaki, M.; Soukoulis, C. M. Phys. Rev. B 79, 121104 (2009).